NONDESTRUCTIVE EVALUATION/STRUCTURAL HEALTH MONITORING OF IMMERSED PLATES BY MEANS OF GUIDED ULTRASONIC WAVES

by

Elisabetta Pistone

Master of Science in Architectural Engineering, Politecnico di Torino, 2008

Master of Engineering in Architectural Engineering, Pennsylvania State University, 2010

Submitted to the Graduate Faculty of

Swanson School of Engineering in partial fulfillment

of the requirements for the degree of

Doctor of Philosophy in Civil Engineering

University of Pittsburgh

2013

UNIVERSITY OF PITTSBURGH

SWANSON SCHOOL OF ENGINEERING

This dissertation was presented

by

Elisabetta Pistone

It was defended on

November 08, 2013

and approved by

Jorge D. Abad, Ph.D., Assistant Professor,

Department of Civil and Environmental Engineering

John C. Brigham, Ph.D., Assistant Professor,

Department of Civil and Environmental Engineering

Luis F. Chaparro, Ph.D., Associate Professor,

Department of Electrical and Computer Engineering

Irving J. Oppenheim, Ph.D.,

Department of Civil and Environmental Engineering, CMU

Dissertation Director: Piervincenzo Rizzo, PhD, Associate Professor, Department of Civil and Environmental Engineering

NONDESTRUCTIVE EVALUATION/STRUCTURAL HEALTH MONITORING OF IMMERSED PLATES BY MEANS OF GUIDED ULTRASONIC WAVES

Elisabetta Pistone, Ph.D.

University of Pittsburgh, 2013

Studies conducted in the last two decades have demonstrated the effectiveness of guided ultrasonic waves (GUWs) for the nondestructive evaluation (NDE), as well as for structural health monitoring (SHM) of waveguides, such as pipes, plates, and rails. Owing to the ability of travelling relatively large distances in dry structures with little attenuation, GUWs allows for the inspection of long waveguides, locating cracks and notches from few monitoring points, while providing full coverage of the cross section. Laser pulses are one of the most effective methods to generate ultrasonic bulk and guided waves in dry structures. In this dissertation we propose a non-contact NDE method based on the generation of broadband ultrasonic signals by means of laser pulses to inspect underwater structures. The waves are then detected by means of an array of immersion transducers and analyzed by means of statistical analysis to search for damages on the wet structure of interest.

In this study we first investigated the effect of water's depth, temperature, and pressure, and the laser energy and wavelength on the amplitude of the laser-induced ultrasonic waves. The results showed that the 0.532 μm wavelength is the most suitable for our applications. A good range of nominal laser energy is comprised between 160 mJ and 190 mJ. Furthermore, the variations of temperature and pressure have minimal effects on the ultrasonic signals. The following phase showed the ability of the technique to detect various types of defects in an

immersed plate, which we achieved by building *in house* A B-scan system, controlled by National Instrument PXI running under LabVIEW. We designed two series of tests in which the number of transducers, their spatial arrangement, as well as the types of features extracted from the time, the frequency and time-frequency domain varied. By developing two unsupervised algorithms based on outlier analysis, we revealed that the method is capable of successfully detecting a crack and a hole-through. Next, the variation of the energy peak in the time-frequency space was shown to decrease with a dependence on the plate thickness. A range of peak energy was experimentally tabulated and the experimental group velocities of the first fundamental symmetric mode were calculated for six plates of different thickness, varying between 1 mm and 10 mm. Finally, the ability of a focused transducer to interrogate the damage state of the original aluminum plate was shown. As predicted, our multivariate algorithm successfully detected all the five defects devised on the plate. This work concluded with a comparison between the two methods. The results showed that both the hybrid laser-immersion transducer technique and the focusing technique can be successfully used for the noncontact monitoring of immersed plates.

TABLE OF CONTENTS

LIST OF TABLES

LIST OF FIGURES

ACKNOWLEDGEMENTS

To a cyclic concept of history.

"Κτῆμα…ἐς ἀεὶ…" (Thucydides)

I would like to express my deep gratitude to my advisor *Prof. Piervincenzo Rizzo* for his guidance and supervision during my Ph.D. studies. He gave me the opportunity to study some of the most recent advancements in the NDT/SHM field.

I owe my sincere thanks to the members of my defense committee, *Prof. Jorge D. Abad*, *Prof. John C. Brigham*, *Prof. Luis F. Chaparro*, and *Prof. Irving J. Oppenheim*, for reading the manuscript, and for all the suggestions and insightful discussions.

I am thankful to *Mr. Charles C. Hager* for his availability and help in building various equipments for my experimental setups.

I sincerely appreciated the time spent with the colleagues of the *NDE and SHM Laboratory* and all the formative discussions we had throughout these years.

I acknowledge the financial support of the NSF, grant number *CMMI 1029457*, and of the Teaching Assistantships provided by the *Civil and Environmental Department* of the *Swanson School of Engineering* to support my Ph.D. studies.

I warmly embrace all my *friends*, close and far away. The nature of friendship, πολύτροπος, has been a full moonlight during all these years.

My *whole family* has always been in my thoughts. I became a traveler with them, first experiencing νοσταλγία. I learnt that we have to continuously challenge our safe beliefs with different points of view, but also that nothing tastes as strawberries in our countryside home.

Finally, I wish to dedicate this work to my beloved fiancé *Paolo*. I would be as fragile as grass after days without rain or as tasteless as food without salt if not for him. I learnt from Paolo that we are real even when we dream, "*Σκιᾶς ὄναρ ἄνθρωπος*" (Pindar). In fact, "*Sólo muere un amor que ha dejado de soñarse hecho materia y que se busca en tierra*" (P. Salinas).

1.0 INTRODUCTION

Existing structures are aging and constantly novel materials and technology of constructions are employed for new engineering systems. Even though innovation is what potentially improves our daily life, methods to properly assess the damage-state and, therefore, the level of safety of the systems we are developing are needed. Nondestructive testing (NDT), also called nondestructive evaluation (NDE), are becoming more and more attractive due to their enormous potential. The American Society for Nondestructive Testing defines the NDT methods as those methods employed to inspect a material, an object or system without impairing its future usefulness [1]. Therefore, NDT methods can potentially investigate the damage state of a structure without further damaging. In literature, as well as in the industrial development side, various methods have been studied and implemented and their use and effectiveness is based upon the application. Nonetheless, their potential resides in the aim of detecting damage and, as a consequence, preventing failure at a very early stage. Thus, safety is increased and costs associated to unexpected failures are decreased. In fact, ideally, a constant or well-appointed monitoring allows the detection of flaws at an early stage, thus leading to expenses related more to maintenance and service rather than extensive repair. The structural health monitoring (SHM) approach is based on the process of implementing a damage detection strategy (with the aim of real time monitoring) for engineering structures. SHM techniques very often make use of NDT methods. In general, effective NDT and SHM techniques should reach a level where they are

capable of detecting and quantifying damage at the very beginning, thus increasing the level of safety of our engineering system.

This study attempts to develop a NDT method based on the generation of guided ultrasonic waves (GUWs) by means of a laser. These waves are then detected by conventional immersion transducers. This hybrid laser/immersion transducer technique aims at detecting damages in immersed plates. The novelty of the research presented here is the use of laser pulses to generate broadband omnidirectional signals in an immersed waveguide and the overall signal processing applied to wet waveguides for damage detection purposes. The proposed NDE/SHM scheme may overcome some of the challenges related to monitoring of immersed structures. For instance the scan of large structures is possible without the need to install and maintain a large number of transducers *in situ*.

1.1 MOTIVATION AND OBJECTIVE

The objective of the research presented in this work is to investigate the hypothesis that a hybrid laser/immersion transducers system enables the inspection of underwater structures. The research addresses the need for the prevention of failures of important structural systems such as water mains and focuses on fundamental research that shall lead to the design of new technologies. The long-term aim is extending the lifetime of those critical infrastructures that contain or are surrounded by water. It is expected that the success of this research may pave the road to a new frontier of NDT and SHM of wet large structures.

The need of this research is driven by the fact that the rupture of water mains for example, although might be spectacular (Figure 1.1.), is too often accompanied by distress in

local communities and avoidable costs for municipalities. Water mains breaks are also the subject of local news primetime as their impact to residential areas and businesses can be very significant. The economic and social costs associated with pipeline breaks in modern water supply systems (WSS) are rapidly rising to unacceptably high levels. The Environmental Protection Agency reported that there are 240,000 water main breaks per year in the U.S. water distribution systems causing, according to the U.S. Geological Survey, water losses in the amount of 1.7 trillion gallons at a cost of $2.6 billion per year [2].

Figure 1.1. (a) Picturesque photo of a water main break [2]. (b) Street collapse due to a water main break [3].

To date, two types of failure management strategies are applied: prevention and reaction. The first one is achieved by proactive asset condition assessment which, however, cannot be extensively applied to WSS due to high cost, slow speed of inspection, and often requirement for service interruption. Therefore, a protocol to minimize the reaction time and losses associated with a failure is implemented. As the infrastructure ages and the price of commodities increase,

there is growing pressure on public authorities to shift the management strategy from reactive to proactive. Undertaking more extensive and detailed inspections of underground pipes is therefore much needed. The primary difficulty with water pipe inspection is accessibility. The exterior is buried underground while the interior is inaccessible to conventional tools because it is a pressurized system.

What we propose is to: use GUWs that, in the future, can also be generated and detected from the inside of the pipe using pulsed laser and immersion transducers, respectively, to detect and quantify damage present on the surface or under the interior walls; apply advanced digital signal processing (DSP) to GUWs data for data mining, feature extraction, and damage classification; propose the design of a prototype that may be implemented in an underwater vehicle (UwV) to inspect pipes from the inside without service disruption, or to inspect underwater structures.

The uniqueness of the proposed research with respect to existing technologies relies upon the following high-risk approaches and novelties:

- exploit the ablation at the liquid/solid interface induced by immersed pulsed laser beams for the non-contact generation of high signal-to-noise ratio (SNR) stress waves propagating along the structures and leaking into the liquid;
- use of leaky Lamb waves for surface damage detection in plate immersed in water;

The long-term goal is to design a conceptual UwV able to distinguish among three damage states: pristine, damaged but not critical, and critical. The latter shall lead to target repair/replacement. The main broad impact of the project is the “natural” expansion of the proposed solutions to large underwater systems such as pipes, submarines, ships, or offshore platforms.

1.2 NDT/SHM OF IMMERSED STRUCTURES

In this section we report a brief review of the NDT or SHM methods used to inspect or monitor water mains or underwater structures. The content of this section is largely excerpted from Rizzo [4][5].

Structures containing or surrounded by water are ubiquitous in the modern world. They can be arbitrarily clustered into the following groups: oil or natural gas offshore structures, communication cables, pipelines, naval vessels, waterfront facilities, water mains and pipes. With the advent of renewable energy technology, a new type of offshore structure is represented by sea wind farms [4]. The economic and strategic impact of these structures is enormous but, owing to the operational conditions, they are vulnerable to internal and external corrosion, manufacturing flaws, ship anchors, and seismic movements of the sea bed. Moreover, some of these structures are already operating beyond their designed lifetime. As such, the periodic inspection or the permanent monitoring of structures surrounded or containing water is necessary to avoid risks for personnel and the environment, and to minimize economic losses.

In general, the inspection of underwater structures is challenging due to tidal conditions, weather, marine growth, visibility, and accessibility. Irrespective of the engineering system being assessed, the inspection is carried out applying NDE techniques that closely resemble topside NDE tools, i.e., tools that are direct applications or modifications of techniques employed in dry conditions [6]. The modifications usually consist of waterproofing and adaptation of the instruments to the sub-sea environment [7][8]. Several underwater structures are made of thin-walled metallic parts.

Due to the different topology and hydraulic characteristics, several failure detection and location techniques have been proposed for water and wastewater systems. These techniques can

be divided according to the physical phenomenon they exploit: X-ray, magnetic, visual, ultrasound, or acoustics. Drawbacks associated with one or more of these approaches are: slow inspection speed, not trenchless, and the requirement for service interruption [9].

X-ray radiography uses high energy electromagnetic waves that penetrate into the object and "sees through". The technique has the advantage that the pictorial image from the investigation is, to some extent, intuitive. However, safety concerns arise because of the radiation and the high voltage necessary to generate the X-rays [10].

Magnetic Flux Leakage (MFL) requires magnets or electro-magnets to generate magnetic flux flowing in the pipe. Defects are detected by measuring changes in the pipe's magnetic permeability. The main disadvantage of the MFL inspections is the bulkiness of the probes, the energy required for magnetization, the cost, and the need to have the pipe empty [10].

Magnetic Particle Inspection (MPI), used to detect defects at or near the surface of a ferromagnetic material, consists of magnetizing the sample and coating it with ferromagnetic particles. Any defect in the material will affect its magnetic field and thus the position of the particles. MPI is low cost and simple to operate. However, it is impracticable for large structures as it requires thorough cleaning and drying of the surface. It also requires magnetization of the entire pipe specimen [10].

Eddy currents can be used to measure wall thickness by inducing the magnetic fields in the material. Internal inspection speed however is low and effectiveness is limited whenever the lift-off distance between the probing devices and the structure is large [10].

One of the most growing sectors in the construction and civil engineering field is the trenchless technology, i.e., a family of subsurface construction used to install or repair

underground infrastructure with minimal disruption of the regular activities nearby. However, none of the above methods is feasible for trenchless inspection of freshwater mains.

Visual methods are mainly related to the use of closed-circuit television (CCTV). This is the standard technology for the NDE of air sections of sewers (Water Env. Research Found.). A typical CCTV system includes a color CCTV and lighting system mounted on a wheeled carriage. The use of CCTV is limited to the pipe surface located above the flow surface and it is mainly qualitative in nature. Image processing software is available (e.g. AQUA-selekt, AQUA-WertMin [11]). Systems like the Panoramo 3-D, mount optical scanners that provide the same information as digital CCTV, with the added benefit of unwrapping the pipe size [12]. For wastewater mains, for instance, a typical inspection device is the three-stage cable-guided swimming system called SEK developed in Germany and shown in Figure 1.2 [13]. In the first stage, SEK inspects and measures the entire sewer line and conducts camera inspections, recording major abnormalities such as erosion, deposits, obstacles and leaks in the gas space. Then, a wheel-driven cleaning device eliminates deposits detected by the SEK and cleans the sewer wall before a damage-survey device monitors the sewer, measuring joint widths, pipe offsets and cracks with greater accuracy than the first stage. A major problem with video imaging is the effect that lighting and perspective can have on the appearance of a defect. The quality and angle of lighting provided during the inspection directly impacts the operator's ability to accurately diagnose pipe defects. For instance, shadows created by lighting can create the mirage of multiple fractures or holes.

Figure 1.2. SEK prototype [13].

Active sound methods like sonar are used in both dry and wet portions of sewer systems to provide pictorial evidence of sewers beneath the flow line. Sonar can generate a 360-degree outline of the interior of a filled pipe. Sonar requires more specialized service than CCTV, and it only allows the surface profile to be seen [14].

Passive sound detectors are used for leakage detection by sensing sound or vibration generated by water as it escapes from pipes under pressure. Traditional techniques have relied on the detection of leakage from above ground using accelerometers or hydrophones attached at strategic locations [15]. Sahara (Figure 1.3) is a pigging technology devoted to leak detection [16].

Figure 1.3. The Sahara system [12].

A sensor mounted on an umbilical cable is introduced into the pipe. The sensor travels along with the flow; as it passes it generates a sound for any leak it detects, thus giving an indication to the operator. The umbilical cable allows its position along the pipe to be controlled precisely [12]. BHRSolution's developed the HearLeak pig that is similar to the Sahara system. This device fits tightly to the pipe and may disturb sediment [17]. This system is also tethered, which limits its use and flexibility.

Conventional ultrasonic testing (UT) such as local thickness gauging, uses bulk waves and only tests the region of pipe below the transducer. The requirement for scanning makes this inspection time consuming.

The passive detection of ultrasonic waves generated by material cracks or dislocation is described as an Acoustic Emission (AE) technique. In pipes, the waves may be generated by friction, crack growth, turbulence, leaks, or corrosion. Sensors can be made by piezoelectric transducers, hydrophones, or accelerometers. AE monitoring requires the presence of an "active" defect such as a moving dislocation or a growing crack to be detected [18-22]. Therefore, the technique is suitable to detect damage onset and/or propagation but cannot detect existing or "silent" damage.

Finally, large diameter Prestressed Concrete Cylinder Pipes (PCCP), if internal inspection is viable, can be sounded using either primitive tools or more sophisticated impact-echo equipment. If human entry is not feasible, then acoustic emission monitoring for wire breaks could be considered. However, the method is time-consuming and applicable only to PCCP.

In recent years, the use of GUWs was proven efficient for the NDT / SHM of waveguides. Owing to the ability to travel relatively large distances in dry structures with little attenuation, GUWs allows for the inspection of long lengths of waveguides, locating cracks and

notches from few monitoring points, while providing full coverage of the cross section [23-27]. Therefore, they represent a very promising method to be employed. Finally, they can travel long distances with little attenuation. Few studies presented the use of GUWs for underwater structures [28].

Na and Kundu [29] devised an innovative transducer holder to activate flexural cylindrical waves for damage detection in underwater pipes. Mijarez *et al.* [30] developed a waterproof transmitter and a seawater-activated battery package to monitor the tubular cross-beam members used in offshore steel structures. Bingham *et al.* [31] studied the use of Lamb waves to detect limpet mines on ship hulls. The whole idea is to prevent the approach of a swimmer to a ship, in order to ensure the security of the vessel during navigation. They developed robots carrying ultrasonic sensors that are attached to the ship hull above the water line. These robots have the capability of sending high power signals that are guided along the hull surface and that are received by a sensor placed on another robot. They used a signal processing technique called the Dynamic Wavelet Fingerprint Technique in order to synthesize the guided wave information in a two-dimensional binary image. Since the interpretation of the signals may become extremely complex, they also developed a parallel 3D elastic wave simulation using the finite integration technique. From a theoretical point of view, if a mass is present on a ship hull, there is an increase in thickness of the ship hull, and so this actually changes the velocity of the guided wave mode taken into consideration (speed up or slow down, depending on the mode selected). Since the arrival time of the wave can be calculated, if there is a delay in time, a mass can be present in the field. Wavelet are particularly appropriate for this application because they take into account (and display) both time and frequency. They run four

tests on a mock-up of a ship placed in dry conditions. They simulated the mine with a weight and four magnets for a total of 3kg that was placed on the underside of the ship.

1.3 STRUCTURE OF THE DISSERTATION

This dissertation is organized as follows. The theoretical background about GUWs and laser ultrasound is presented in Chapter 2.0 . The fundamental research, which includes the study of the effects of water absorption, laser energy, temperature and pressure on the amplitude of the laser-generated waves is presented in Chapter 3.0 . The development of a remotely and automatically controlled hybrid laser-immersion transducer system used to inspect immersed plates is described in Chapter 4.0 . In particular, four immersion transducers were used as receivers and four artificial defects were devised on an immersed plate. A SHM algorithm was developed to discriminate the presence of such defects. In the same chapter, an analysis which includes an expanded version of the SHM algorithm, a new transducer setup as well as an additional type of defect is presented. Chapter 5.0 presents a study conducted on the frequency content of laser-generated waves in plates of different thicknesses. Chapter 6.0 describes a study conducted on guided waves generated by a focused immersion transducers and detected by five immersion transducers in an immersed plate where five different types of defects were devised. Finally, Chapter 7.0 discusses some directions for future studies.

2.0 BACKGROUND AND METHODOLOGY

When an ultrasonic wave propagates into a bounded media, a GUW is generated. The wave is termed “guided” because it travels along the medium guided by the medium geometric boundaries. The shape of the waveguide defines the types of GUWs that can propagate.

Laser ultrasonics is one of the most effective methods to generate ultrasonic bulk and guided waves. In general, laser ultrasonic techniques (LUTs) involve the generation of ultrasounds by irradiating the surface of the test object with laser pulses. The ‘‘heat shock’’ provided by the thermal expansion or the ablation accompanied with the irradiation produces the formation of stress waves [32][33]. In semi-infinite solids, longitudinal waves, shear waves, surface (Rayleigh) waves, and head waves can be generated. When the test object has a plate-like, pipe-like, or bar-like shape, the longitudinal and shear waves combine to form a guided wave. The advantages of LUT for NDE applications include noncontact generation and detection, remote placement of equipment (>1 m), easy scanning, absolute displacement calibration, both broadband and narrow band signal generation, wide frequency band measurement, and applicability to curved surfaces [34].

2.1 GUIDED ULTRASONIC WAVES

The study on the propagation of guided waves in waveguides is widely diffuse in literature due to the enormous impact in real applications, such as material characterization, or plates, pipes and railroad inspection [26][35-39].

In hollow cylinders, GUWs can propagate along the circumference (circumferential guided ultrasonic waves - CGUWs) and along the axial direction (longitudinal guided ultrasonic waves - LGUWs). Three different modes can propagate; longitudinal, flexural, and torsional modes. The modes are usually labeled L(0,n), T(0,n), and F(m,n) and they, respectively, refer to longitudinal, torsional, and flexural modes. The first index m gives the harmonic number of circumferential variation, and the second index *n* is a counter variable. The simultaneous presence of many modes and their dispersive behavior, i.e., the propagation velocity and the attenuation depend on the wave frequency, are represented by the dispersion curves that describe the relation between the wave velocity and the frequency. The phase velocity C_p of a GUW is the speed at which an individual crest of a wave moves. The group velocity C_g dispersion curve describes at which speed the energy propagates and it gives information about how quickly the energy of the wave packet propagates.

Numerical methods, such as the DISPERSE package developed in the U.K. [40] or Semi-analytical Finite Element (SAFE) Method have been developed for extracting modal solutions from a variety of waveguides, including empty and filled pipes. The SAFE method is an efficient tool for extracting the dispersion curves for waveguides with constant material properties and geometry along the wave propagation direction and it has been developed as an alternative to exact approaches including the matrix-based methods. Compared to the more classic Finite Element method (FEM), where the entire structure has to be modeled (3D), the SAFE method

models waveguides only in two dimensions, thus reducing the computational time. In other words, according to the SAFE method, only the cross-section of the waveguide is modeled and the displacement along the third dimension (length) are described by harmonic functions of the type exp(-iωt) [41]. The dispersion curves are plotted through the obtained solution from an eigenvalue problem [42]. This method has been recently applied to rods [43], rails [44][45], empty pipes [46][47] and plates [40]. When the thickness is much smaller than the other dimensions, the target is considered as a plate. Figure 2.1 shows the phase velocity and group velocity dispersion curves for an aluminum plate in dry conditions.

Another important aspect to consider in the GUWs employment is that part of the energy of the waves leaks into the surrounding environment (medium). This particularly happens at solid-liquid interface. This has to be considered because energy leakage causes signal attenuation, i.e., the signal diminishes in amplitude as it travels. Some guided wave modes are more prompt to exhibit energy attenuation, so attention must be paid to select a mode that properly meets the requirement of a specific application.

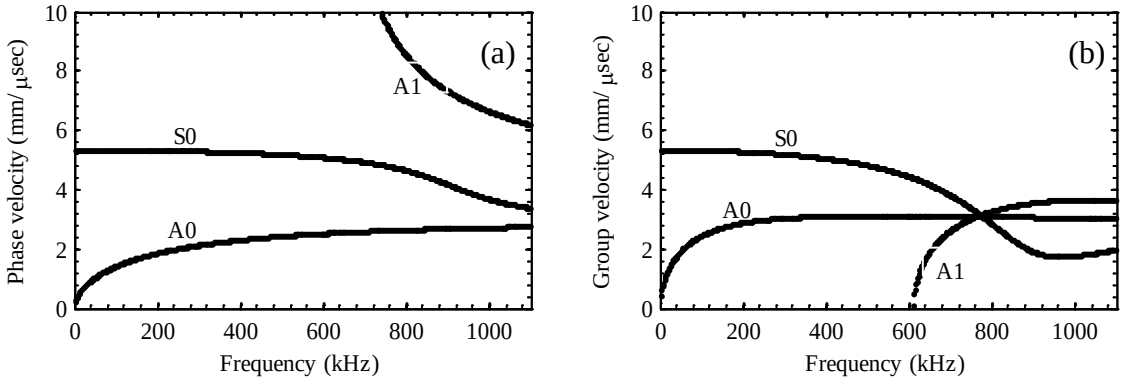

Figure 2.1. (a) Phase velocity dispersion curve of the 2.54 mm thick aluminum plate in dry condition. (b) Group velocity dispersion curve of the 2.54 mm thick aluminum plate in dry condition. Courtesy of Mr. Abdollah Bagheri.

From a theoretical point of view, extensive work has been conducted on cylindrical guided waves. Gazis [48] was the first to develop the dispersion curves for GUWs in hollows isotropic cylinders while Fitch [49] first matched experimentally Gazis' prediction. Then, researchers focused on cylinders filled with liquid. Safaai-Jazi *et al.* [50], Simmons *et al.* [51] and Viens *et al.* [52] provided the entire range of dispersion curves for this case.

Rose and its group of research at The Pennsylvania State University extensively investigated the propagation of guided waves in pipes [53],in hollow cylinders with outside fluid load [54], and their applications to SHM [55-57]. They demonstrated the feasibility of their solution as well as the challenges that GUWs present.

Liu *et al.* [58] investigated the propagation of guided waves in pipes under changing environmental conditions since these factors can dramatically influence the acquired signals.

Finally, the research group lead by Prof. Cawley at the Imperial College of London [59-65] investigated the capability of GUWs at detecting different types of defects in pipes. They also studied the propagation of GUWs in fluid-filled pipes [66] and in large structures [67], just to cite a few of their works reported in the literature. They also created an enterprise that developed equipment and technology to interrogate the state of pipelines. In fact, Guided Ultrasonic LTD system developed a system based on low frequency guided waves to inspect underwater pipes and marine risers [68].

When the inner diameter of the pipe is much larger than the wall thickness, the pipe can be considered unwrapped to ease the mathematical and numerical formulation, thus becoming a plate. If this is the case, Lamb waves are generated. Lamb waves are elastic disturbance in thin plates or shells, so they are guided waves that propagate in plates. They belong to the family of guided waves because they propagate in a structure that has the shape of a waveguide and they

are dispersive, as their velocities are dependent on frequency and thickness. Up to today, they have been largely used for NDE of plate-like structures, because of their strong penetration, fast and omnidirectional propagation, low attenuation even in underwater structures, low energy consumption, ominidirectional propagation and high sensitivity to damage.

Figure 2.2 shows the generation of Lamb waves by a longitudinal transducer [26].

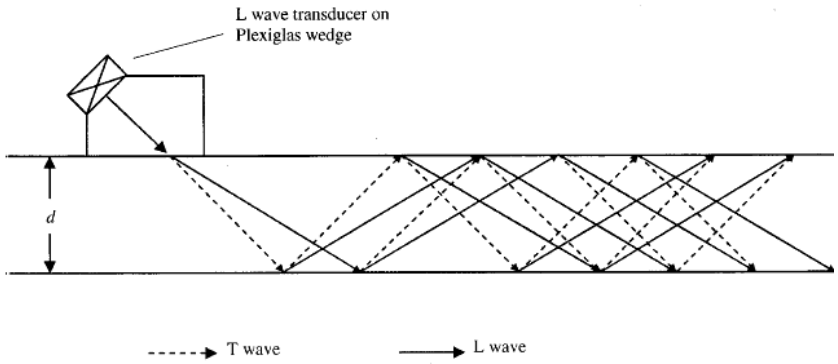

Figure 2.2. Generation of Lamb waves in a dry plate [26].

In plates, Lamb waves can propagate with a symmetrical mode (S_i), where the particles of the neutral fiber perform pure longitudinal displacements, or with an anti-symmetrical mode (A_i), where the particles of the neutral fiber perform pure shear oscillations. Here, the subscript is the order of mode. Figure 2.3 shows the symmetric and anti-symmetric particle displacement about the center of a plate [10].The S_0 and A_0 mode are the fundamental modes that co-exist at any frequency. As the frequency increases, higher-order modes appear.

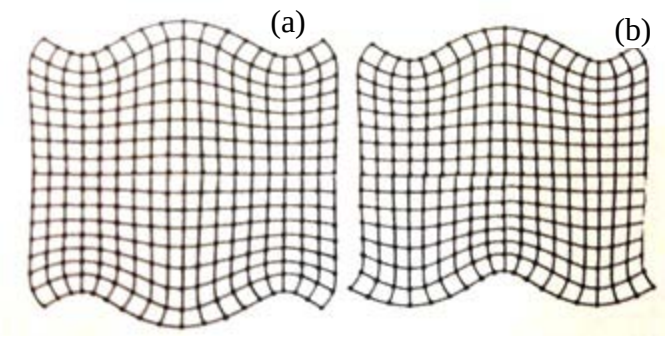

Figure 2.3. (a) Symmetric and (b) anti-symmetric particle displacement about the center of a plate[10].

However, the existence of multiple Lamb modes at higher *frequency x thickness* product makes the applications extremely complex. To overcome this difficulty, generally working at low frequency-thickness product and/or mode selectivity achieved with specific transducers is recommended. In fact, dependent upon material and geometry, generally, the low frequency-thickness regime is preferred since it presents lower number of modes. Therefore, selective excitation could be achieved. On the contrast, higher frequency-thickness regimes present more complex pattern of propagating modes, thus making much more difficult the selective excitation of modes. A great deal of research has also been conducted with the scope of developing particular transducers capable of exciting particular modes. For instance, remarkable work has been conducted on the Lamb wave generation with piezoelectric sensors in the SHM field. Mode selectivity has also been proved both theoretically and experimentally to establish the relationships between transducers dimension and excitation frequency [69-71].

Symmetric and anti-symmetric wave propagations in a plate in vacuum have also been solved analytically and numerically and are widely reported in the literature [24][26][27][72-78]. Similar studies were also conducted for plate immersed in water [79-85].

The research group led by Prof. Cawley at the Imperial College of London carried also out extensive research on Lamb waves. Their studies include, but is not limited to, the generation

and propagation of Lamb waves in plates [86-87], the interaction of Lamb waves with defects [88], and they optimize Lamb waves inspection techniques [89] .

Other interesting works include the excitation of specific GUWs for application-based use. For instance, Greve conducted a study in thick plates where he proved that, besides classic guided waves, nearly-longitudinal waves could also be extremely useful in flaw detection due to their shorter wavelength [90]. Greve *et al.* [71] [91]investigated the use of Lamb waves in plates and the development of wireless sensors to be used in SHM applications.

When geometries have a dimension much smaller than others, such as in strips, the pattern of propagating modes becomes even more complicated. This is mainly due to the reflection coming from the width direction. However, even in this case, it is sometimes possible to achieve selective mode generation and, among all the possible excited modes, some of them display very interesting characteristics and their behavior can be inferred by the energy concentration in the target. Cegla in 2008 proved that it is possible to excite two modes in large aspect ratio rectangular strips that resemble the first symmetric and first antisymemtric modes that would propagate in a plate [92]. Besides the FEM simulation, he also conducted a series of tests where he proved that desired modes can be excited even in strips. It is important to note that, for these modes, the energy concentrates in the center of the strip and will decay towards the edge. Practical applications include the fact that strips of this type can be attached to other structures for various purposes without interfering with wave propagation.

If water is present, Leaky Lamb waves are generated. Pavlakovic studied the use and the benefits of Leaky guided ultrasonic waves in NDT [79].

In the case of a plate immersed in a liquid, the coupling between different media (for example aluminum and water) produces additional phenomena that have to be taken into

account. In fact, the surrounding medium allows the Lamb waves to leak outwards from the solid, thus potentially attenuating the propagation of the Lamb waves in the solid. This process depends on the propagating mode and, being dispersive, it varies for each mode shape [93]. In fact, since the S_i mode is mainly characterized by in-plane displacement, this means that the energy of the Lamb waves for this mode will mainly be retained in the solid (ex. in the plate). On the other hand, since the A_i mode is mainly characterized by out-of-plane displacement, the energy associated with this mode will mainly leak into the surrounding medium (liquid, for example water).

For damage detection, the fundamental modes are the most widely employed, being the fastest. Several differences distinguish the S_0 from the A_0, thus making one mode more appealing than the other, depending on the application. Generally, the S_0 is less prone to attenuation compared to the A_0 mode due to the fact that most of its energy is retained in the solid since it has mostly in-plane displacement. Then, its phase velocity is higher. On the hand, the A_0 mode is easier to be generated since commercial transducers can easily excite out-of plane displacements. Even though it attenuates quickly, the signal amplitude is larger, thus improving the SNR ratio. Moreover, since the A_0 mode has a shorter wavelength at a given excitation frequency, its sensitivity to smaller defects is higher. Therefore, both modes can be used for damage identification. The S_0 mode is more sensitive to damages in cross-section of the target and to delaminations, while the A_0 mode performs better at detecting cracks or corrosion [93].

Finally, other researchers concentrated on the propagation of the quasi-Scholte waves as appropriate to detect defects in immersed structures. In fact, the dispersion equations predict another wave called the quasi-Scholte wave, which is a wave that propagates at the interface between solid and liquid and it is not leaky. At high frequencies, the wave energy will decay

exponentially away from the surfaces at a faster rate (the wavelength decreases with higher frequency). However, at low frequencies, it has a dispersive behavior. Cegla *et al.* also showed that the quasi-Scholte mode changes in energy partition between fluid and solid with frequency [94]. In fact, below 500 kHz-mm, the energy flows predominantly in the plate, while at frequencies higher than 1 MHz-mm, most of the energy travels in the fluid. Figure 1.4. shows the mode shape of the quasi-Scholte mode at varying frequencies.

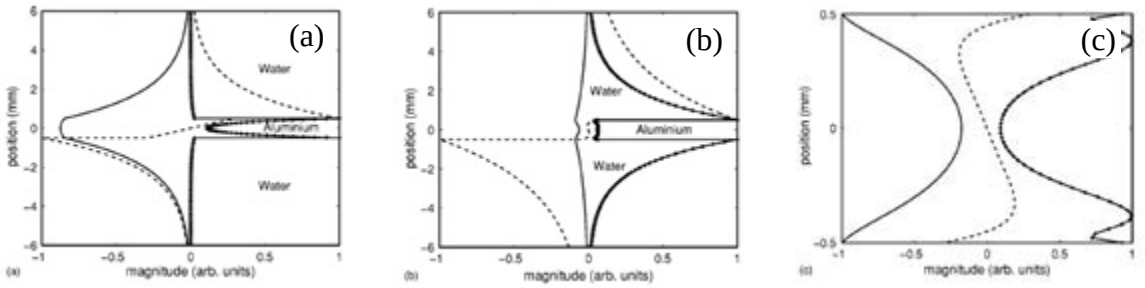

Figure 2.4. Mode shape of the quasi-Scholte mode (water-aluminum) at varying frequencies [94]. (a) 0.1 MHz-mm; (b) 1 MHz-mm; (b) 2 MHz-mm, in plate only[— — out-of-plane displacement; --- in-plane displacement; +++ strain energy density].

In particular, Figure 2.4.a shows that the out-of-plane displacement component at 100 kHz-mm is almost constant across the section of the plate, and most of the energy is propagating in the plate. Figure 2.4.b shows that, at higher frequencies, most of the energy is traveling in the fluid. Figure 2.4.c shows the mode shape in the plate alone at 2 MHz-mm. Displacements decay away from the surfaces and are a minimum at the center of the plate.

2.2 LASER ULTRASONICS

Laser-ultrasonics is one of the most effective methods to generate and detect ultrasonic bulk and guided waves. In general, LUTs involve the generation of ultrasounds by laser pulses and the detection of ultrasonic signals by continuum laser. Laser pulses generate mechanical waves by irradiating the surface of the test object. The “heat shock” provided by the thermal expansion or the ablation accompanied with the irradiation produces the formation of ultrasounds up to few MHz frequency [32][33][95][96]. Figure 2.4a shows the laser-generated ultrasound in the thermoelastic and in the ablative regime and Figure 2.4b shows the directivity patterns for the shear and longitudinal waves [10]. The most important advantages associated with the LUT method is the non-contact generation, remote placement of equipment, and wide frequency band excitation [97][98]. In semi-infinite solids longitudinal, shear, surface (Rayleigh) waves, and head waves can be generated. When the test object has a plate-like, pipe-like, or bar-like shape, the longitudinal and shear waves combine to form a guided wave. The advantages of LUT to quantitative NDE include non-contact generation and detection, remote placement of equipment (> 1 meter), easy scanning, absolute displacement calibration, both broad band and narrow band signal generation, wide frequency band measurement, and applicability to curved surfaces [99].

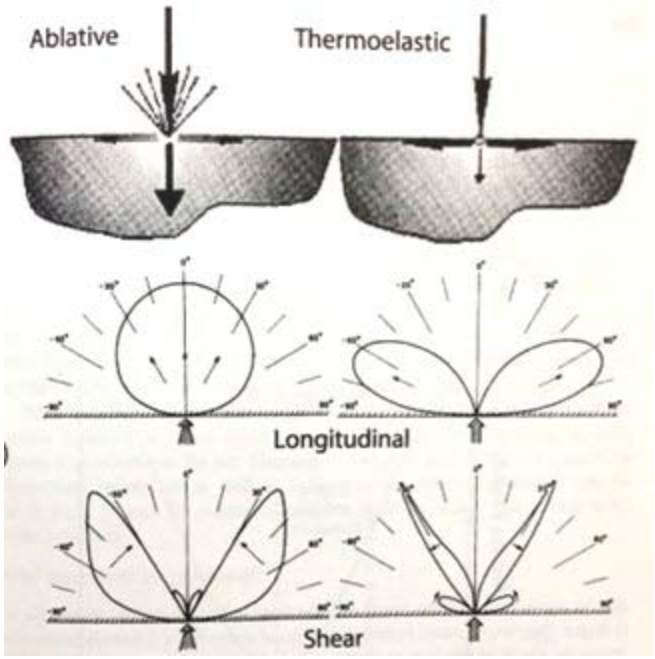

Figure 2.5. Laser-generated ultrasound in the thermoelastic and ablative regime. (a) Magnitude of force perpendicular and parallel to the specimen surface (b) directivity patterns for the shear and longitudinal waves [10].

The generation of ultrasonic waves by means of pulsed laser for NDE applications has widespread applications, spanning from aerospace to civil structures. In NDE one major application is related to flaw detection and materials characterization. The interested reader is referred to Davies' review article for a broad review of laser-based ultrasonic applications [100]. In all these applications, the structure under investigation is dry. Sometimes, in order to raise the SNR, a thin layer of gel or water is deposited on the surface irradiated by the laser.

2.2.1 Laser ultrasonics in dry structures

The ability of using laser pulses to generate guided waves for NDE/SHM in dry structures is well-established [101-105]. Lasers emit electromagnetic radiation whose wavelength may range from the infrared to the ultraviolet portion of the spectrum. When a laser beam is incident on a

solid material, the radiation will be partially absorbed and partially reflected. The fraction of energy being absorbed depends upon the material properties and the laser wavelength and it is converted into heat. The solids are usually too thick to allow for transmission [33]. The absorbed electromagnetic radiation will attenuate following the Beer-Lambert law:

$$I(z) = I_0 e^{-\alpha z} \tag{2.1}$$

where α is the absorption coefficient, I_0 and I are the intensities of the light beam before and after passing through a distance z of the target. The total intensity *I*, i.e., the power per unit area of the incident radiation that interacts with the surface, will be:

$$I = I' + I'' \tag{2.2}$$

where *I'* is the absorbed intensity and *I"* is the reflected intensity and this latter parameter is higher for conductive materials. A metric to establish the amount of energy absorbed by a solid is given by the coefficient of reflectivity *R*, defined as:

$$R = \frac{I''}{I} \tag{2.3}$$

For polished aluminum R = 0.94 and R = 0.80 when the laser wavelength is equal to 1.064 μm and 0.250 μm, respectively [33]. Usually, reflectivity decreases as the wavelength decreases. In general, the smaller the R, the more effective is the laser-based generation of ultrasounds because more energy will be absorbed by the test object and converted into

mechanical stress. As Equation (2.3) does not take into account any scattering, Equation (2.3) is valid for polished surfaces that do not present irregularities, damages, or roughness [33].

In dry structures, the transfer of energy from a nanosecond optical pulse to a mechanical wave can occur by thermoelastic transduction or by ablation, depending on the intensity of the pulse and the surface properties of the illuminated target. A thermoelastic stress is created when the laser energy density is low, such that there is no material ablation or plasma formation on the surface of the object. In this regime, shear mechanical stresses are generated by the thermal expansion associated with the sharp increase of the surface's temperature. The physical phenomena can be modeled either as a 1-D problem or as a 3-D problem. In 1-D models the center of expansion is located on the surface of the test object and a plane state of stress occuring along the surface is assumed. In 3-D models, the center of expansion is localized either on the surface or underneath the surface of a test object. In the latter case a triaxial state of stress is assumed. If the center of expansion is located on the surface, a biaxial tensile state of stress is modeled [33].

Laser ablation is generated when the laser's power density is high, or when the surface of the illuminated medium is covered with a film of water or gel. In this case the rapid vaporization (ablation) of the film, or the melting of a small portion of the medium's surface, induces high reaction pressures that can be considered similar to normal stress loading [106]. In the ablative regime, additional phenomena occur [107-111]. The formation of plasma increases the pressure that acts against the target surface raising the normal boiling point of the material. The plasma can also act as a screen on the surface of the target preserving the surface from further damages associated with subsequent pulses. During ablation the plasma continues to absorb light from the

laser pulse, thus becoming extremely hot. The plasma will eventually expand and it will produce an additional impulse reaction acting against the surface [33].

For dry metals, ablation can be achieved with power densities higher than 10^7 W cm^{-2} [33]. As Q-switched laser generally can reach powers of the order of 10^9-10^{10} W cm^{-2}, they are suitable to attain ablation [112][113].

For dry surfaces, the ablation produces a net stress in reaction against the sample [33], which can be calculated from the rate of change of momentum, i.e.:

$$\sigma = \frac{I^2}{\rho\ [L + C(T_v - T_0)]^2} \tag{2.4}$$

In Equation (2.4), I is the incident power density, ρ is the material density, L is the latent heat of vaporization, C is the thermal capacity, T_v is the vaporization temperature, and T_0 is initial temperature. If water is deposited on the object, the amount of mechanical stress transferred from the laser to the test object can be calculated by assuming that the energy transfer occurs only through the ablation of the fluid deposited on the object. In this case, the parameters ρ, L C and T_v of Equation (2.4) are referred to water. Table 2.1 summarizes the water parameters used to compute the net stress against a target in the ablative regime.

Table 2.1. Water parameters used to compute the net stress against a target in the ablative regime.

Parameter	Value	Unit
ρ_w	1000	Kg / m^3
L	2260 x 10^3	J / kg
C	4200	J / kg K
T_v	373	K

The deposit of a thin layer of water or gel on the irradiated surface increases the SNR of the laser-generated ultrasound [97][98]. In fact, the ablative regime ensures rapid vaporization of the film, thus increasing the reaction forces acting against the target surface leading to increased amplitude of the signals involved. This phenomenon can be modeled considering the laser source circular with radius equal to the laser beam's radius. The distribution of the surface stress is elliptical since the film boundary will evaporate sooner, thus producing smaller reaction forces compared to the central location of the source [97]. In this case, the source is buried into the irradiated surface and normal stresses are still the main consequence of the whole ablative process. Plasma will result from ablation and it will be trapped between water and the target. The plasma absorbs part of the laser light causing the reduction of irradiation on the target [114].

2.2.2 Laser ultrasonics in immersed structures

In order to fully understand the mechanism that generates ultrasonic waves in underwater structures by means of laser pulses, the physical phenomena that occur in water when a laser pulse travels should be examined. Irrespective of the presence of a test object, when a high energy laser pulse penetrates water, optical breakdown may occur yielding to the formation of plasma at the water interface, cavitation, and to the formation of shock waves that propagate in water and or in the test object [115-117]. Laser induced breakdown (LIB) occurs when the water's threshold damage is exceeded. The threshold depends on certain characteristics, such as, ionization energy and impurity level and can be exceeded by selecting the proper pulse duration and wavelength. For example, Kennedy *et al*. demonstrated that for a 10 nsec laser pulses the irradiance threshold is $1x10^9$ W/cm^2 [118]. Kennedy *et al.* also showed that impurities do not affect the irradiance threshold at the 0.532 μm wavelength while this does not hold true for the

1.064 μm [118]. LIB creates plasma that expands for the whole duration of the pulse and compresses the liquid, causing the formation of a shock wave front as well as a vapor bubble [118]. The speed of the shock wave decreases to near acoustic wave velocity within one millimeter [118]. The bubble will eventually collapse when its pressure will be much lower than the surrounding hydrostatic pressure. The formation of shock wave and cavitation bubble has been observed for picoseconds, nanosecond, and femtosecond lasers [119-122].

As the laser beam travels through water, it is subjected to absorption and Equation (2.1) applies. Several authors have proposed different values of the absorption coefficient α with some disagreement [123-127]. While the values of α related to the near infrared region agree within 10%, in the visible region discrepancies can be of a factor of two. One reason for these differences is the presence of suspended particles that induce light scattering, a phenomenon particularly significant in the visible region [128].

Water-laser interaction gives also rise to the optoacoustic effect, which is the generation of sound in a medium by the absorption of a modulated (chopped) light [128]. The optoacoustic effect consists of the conversion of the absorbed energy into heat through nonradiative relaxation process. The following equation represents the basis of the optoacoustic phenomenon in water:

$$\frac{a}{E} = \frac{\beta}{2\pi r \rho C_p} \alpha \tag{2.5}$$

where a is the sound amplitude, E is the output laser energy, β is the thermal expansion coefficient, r is the radius of the cylindrical volume considered, ρ is the density, C_p is the specific heat at constant pressure, and α is the optical absorption coefficient [128].

The optoacoustic phenomenon was studied by several authors [129-135]. Patel and Tam exploited it to calculate the absorption spectra of several liquids, including light and heavy water, and benzene [128]. For the case of light and heavy water, their experiments were conducted at 21.5 °C but their results can be considered valid in the 10-30°C temperature range. Please note that here the word heavy refers to the presence of suspended particle in the liquid, while light indicates their scarce presence. In accordance with the Equation (3.5), Patel and Tam observed that the amplitude of the optoacoustic signal depends on the thermal expansion coefficient β which is temperature-dependent. In particular, for the case of light water, β changes sign at 4°C as it starts to increase and this change of sign also inverts the phase of the signal. Therefore, above 4°C, the optoacoustic signal starts to increase in amplitude, as well as the coefficient β [128].

3.0 FUNDAMENTAL RESEARCH ON LASER ULTRASONICS

In this chapter we will present the research conducted to investigate the most important parameters that influence the propagation of laser-ultrasonics in water. In particular, we evaluated the effect of absorption, water depth, laser energy, temperature, and pressure on the fundamental characteristics (amplitude and frequency) of ultrasonic bulk waves. Three series of experiments were conducted. The first series of tests examined the effect of wavelength, water-depth and laser energy on bulk waves. The second series investigated the effect of water temperature on the bulk waves while the third series studied the effect of pressure on the laser-generated waves.

3.1 LASER GENERATED STRESS WAVES ON AN IMMERSED TARGET

The absorption of laser light by a liquid, and in particular water, has been study by several authors with the scope of tabulating absorption spectra at different optical wavelengths [136-145]. Generally, scattering is measured and then it is converted into absorption. Morel [138] studied in detail the scattering in water and he defined the absorption b and scattering s as it follows:

$$a = b + s \tag{3.1}$$

$$s = \iint_{4\pi} \beta(\theta) d\Omega = 2\pi \int_0^{\pi} \beta(\theta) \sin\theta \, d\theta \quad (3.2)$$

Where a is the attenuation coefficient, b is the absorption coefficient and s the scattering coefficient. The scattering coefficient can be expressed as a function of the volume scattering function β(θ). Therefore, if attenuation and scattering are measured, absorption can be calculated. The three quantities a, b and c are all wavelength dependent.

Most of the absorption coefficients have been obtained through conventional transmission techniques [139]. According to this method, a light beam travels through a long path, for instance in a tube, of pure distilled water [145]. At the end of the path, attenuation is measured as well as scattering (or the latter can be considered from tabulated values in literature), thus absorption can be derived according to Equation (3.1). There are several problems associated with this method, such as the fact that the length of the path must be long to properly measure the absorption of water, thus both practical and alignment issues have to be considered. Furthermore, water is contained into tubes or into sealed windows that can increase the scattering coefficients, making this method complex despite the fact that is the most intuitive. This technique is widespread in literature and, generally, the absorption coefficients so calculated agree fairly well as far as the infrared (IR) region is concerned (between ±10%) [128]. This can also be explained with the fact that the absorption coefficients are much larger at longer wavelength. Figure 3.1 shows the absorption coefficients for pure water.

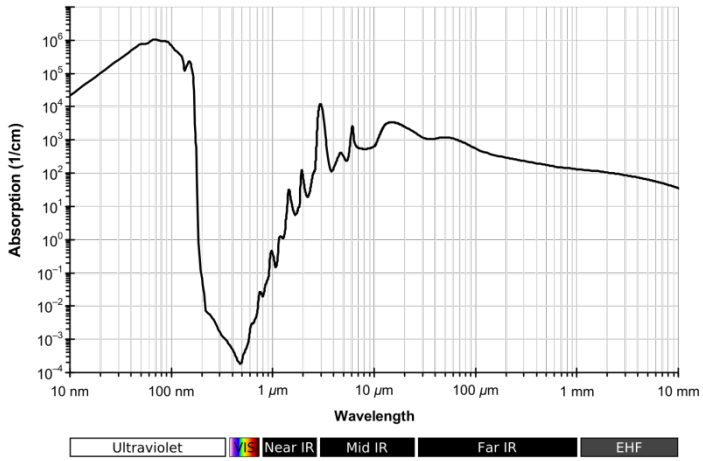

Figure 3.1. Water absorption spectrum [146].

It must be considered that natural water has suspended particles or organic molecules that have their own absorption and scattering properties. Therefore, distilled water is usually used in the experiments found in literature to create a baseline [147].

Even though in this dissertation we aim at discovering the advantages of using specific wavelengths, we consider appropriate to include a brief background on the absorption coefficients of water as these were fundamental parameters to be considered in our analysis. Other methods to measure absorption coefficients include, but are not limited to, the following. Hass and al. developed an adiabatic laser calorimetry to measure absorption spectra in the range 0.488-0.514μm [148][149]. Stone used photothermal techniques exploiting the temperature dependence of the index of refraction [150]. Querry used a split-pulse laser to measure the extinction coefficients in the visible region [141]. Sogandares and Fry used, for the same purpose, photothermal deflection spectroscopy [126]. In 1979, Patel and Tam had the brilliant idea to use optoacoustic spectroscopy to measure the optical absorptions of light and heavy water [128]. In fact, the optoacoustic effect was first introduced by Bell in 1880. He defined it as the generation of sound in a medium by the absorption of a modulated chopped light. Patel and Tam

tabulated the coefficients of absorption in the visible region by sending a pulsed laser beam into a cell filled with water and then analyzing the acoustic waves so generated. They also discovered that, in water, the optoacoustic signal changes its phase at 4°C. In fact, at temperature higher than 4°C, the signal increases in amplitude as the temperature increases. However, below 4°C, it starts to increase in amplitude (with reversed phase) as the temperature is lowered. This phenomenon follows the same trend as the coefficient of thermal expansion β of Equation (2.5) [128]. All these studies were conducted on the effect of water absorption phenomenon *per se* from a physical point of view. Few studies were conducted on the interaction of a laser beam-light with a target, with a metallic target [121] or on the effects of a water confinement regime on the laser-generated waves [114][116][151]. Furthermore, in literature, there is a lack of experiments and theory conducted with the scope of improving practical application of laser-generated waves in the NDT field of immersed structures. Therefore, this chapter addresses the need of investigating fundamental parameters such as absorption, depth, laser energy, temperature and pressure on the effectiveness of LUTs applied to immersed targets.

3.2 EXPERIMENTAL SETUP

In all the three experiments illustrated in this chapters, a 8 ns Q-switched Nd:YAG (CFR 200 – Quantel USA) pulsed-laser operating either at 1.064 μm or at 0.532 μm was used. The laser was remotely controlled using a National Instrument PXI unit (NI PXIe-1062Q) running under Labview only during the last series of tests, otherwise waveforms were recorded and digitized by an Oscilloscope LeCroy (waveRunner 44Xi, 400 MHz Oscilloscope, 5Gs/s). In the former case, we created an interface capable of controlling the generation of laser pulses, their detection as

well as their recording. The number of pulses, the frequency and the energy level could also be chosen. The routine was concerned in such a way to always allow the automatic saving of the signals so generated in a chosen folder.

3.3 EFFECT OF WATER ABSORPTION AND LASER ENERGY. RESULTS AND DISCUSSION

To evaluate the effect of water absorption on the SNR of the laser-induced stress waves, a 1 mm diameter laser beam was delivered to the surface of a test object by means of a mirror and a plano-convex lens (PCX) with focal length of 350 mm (Newport, SPX030AR.33).

Figure 3.2 shows the experimental setup. A plastic pipe 50.8 mm in diameter was glued on the surface of a 255 x 150 x 50 mm aluminum block. The pipe was filled with water at ambient temperature and the water level was progressively raised from 12.7 mm to 203.2 mm at 12.7 mm increments, thus resulting into sixteen levels.

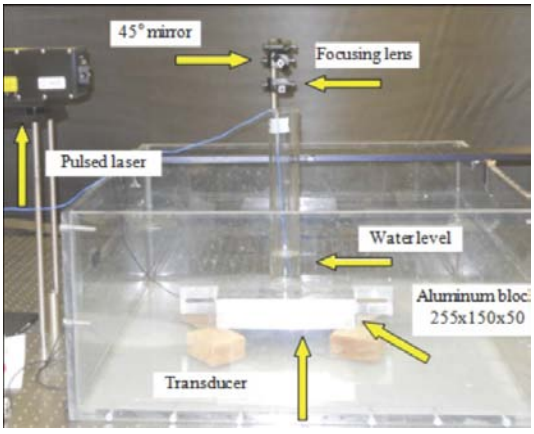

Figure 3.2. Experimental set-up used in the water-level test. Photo of the laser, PCX lens, aluminum block and pipe filled with water.

A 1 MHz commercial ultrasonic transducer (Olympus NDT, V103-RM, Part ID: U8403008), 0.5” in diameter was attached on the opposite face of the block to detect the bulk longitudinal waves generated by the laser pulses. For each water level, five measurements were taken to increase the statistical population data. Both 1.064 μm and 0.532 μm pulse wavelengths were investigated. The nominal laser output energy was equal to 180 mJ for both wavelengths. Assuming the losses through the focal lens and the water negligible, the power densities was approximately equal to 2.87×10^9 W/cm^2.

Figure 3.3 shows the peak-to-peak amplitude of the laser-generated waves as a function of the water level at 1.064 μm (Figure. 3.3a) and 0.532 μm (Figure 3.3b).

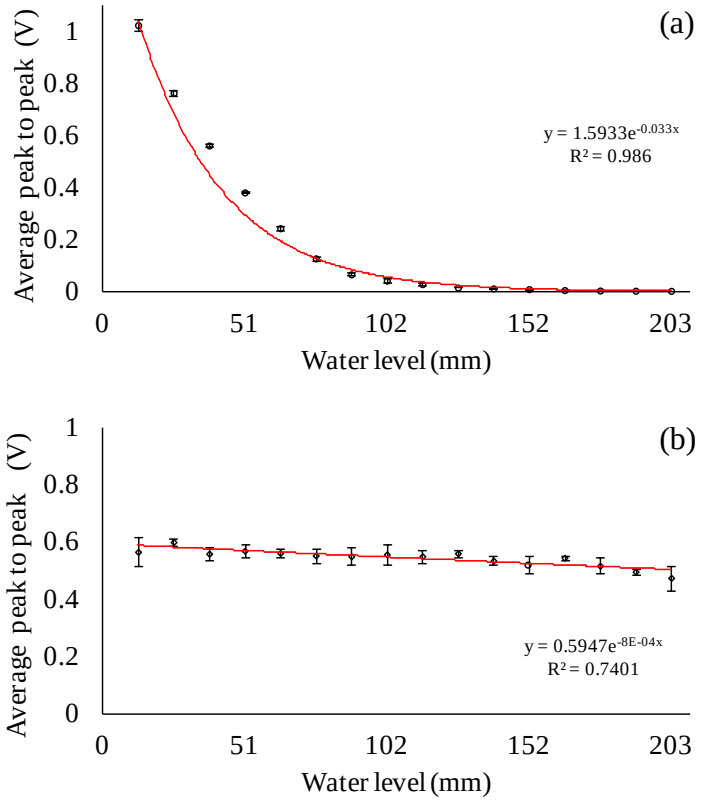

Figure 3.3. Average of the peak-to-peak amplitude as a function of the water level. Effect of the water level on the SNR of the laser-induced bulk waves. (a) 1.064 μm and (b) 0.532 μm.

The dots represent the averaged value of the five measurements and the vertical bars are equal to twice the standard deviation. The continuous red curve overlapped to the dots represents an approximate exponential trendline. As can be seen, the standard deviation is very small, thus confirming the small dispersion of the signals at each water level.

As expected, both curves follow and exponential decay, according to Equation (2.1). However, since the absorption coefficients in the IR region are much higher than in the visible region, in the latter case the exponential behavior is less evident. In fact, also referring to Figure 3.1, the absorption coefficients at 1 μm are in the order of ≈ 0.5 cm^{-1} while at 0.550 μm are in the order of $\approx 10^{-4}$ cm^{-1}. Furthermore, in the visible region scattering is much more predominant than in the IR region [128]. Thus, the signals are less repeatable, fitting less precisely an exponential decay, as proved by the lower R-squared value in Figure 3.3b.

In the 1.064 μm case, the average amplitude of the bulk waves drops almost to zero after 90 mm. Therefore, the IR wavelength is not suitable in real application since the laser beam, due to physics, is absorbed after a small distance. In the 0.532 μm case, the average amplitude of the bulk waves remains constant around a value (0.6 V) which corresponds to the 1.064 μm case after only two water-level steps. Thus, even if the initial surveyed average amplitude is higher in the IR region, the green light permits a good applicability in real cases since it displays an overall higher and more flat behavior.

Then, we compared the experimental data to the theoretical prediction given by Equation (2.1) for both wavelengths. As for the absorption coefficients, having great discrepancy among researchers, we first referred to the extinction coefficients $k(\lambda)$ tabulated by Hale and al. being the most widely cited in literature [123]. The values of $k(\lambda)$ are tabulated only for discrete values. Therefore, we considered the two closest values to both 0.532 μm and 1.064 μm and we linearly

interpolated between them to obtain the *k(λ)* values corresponding to our wavelengths. Finally, we computed the absorption coefficients α(λ) by using the Lambert absorption coefficient equation to plot the theoretical curves based on Equation (2.1):

$$\alpha(\lambda) = \frac{4\pi k(\lambda)}{\lambda} \tag{3.3}$$

where k(λ) represents the extinction coefficients and λ is the wavelength considered. For the 1.064 μm we obtained α(λ) equal to 0.6056 while for the 0.532 μm we obtained α(λ) equal to 0.0003539 [123]. Even though the absorption curve is not linear, as can be seen in Figure 3.1, we adopted a linear interpolation of the *k(λ)* values because the increments step tabulated by Hale and al. are close enough to justify such a choice for our application. The theoretical curves so obtained where then overlapped to the experimental ones presented in Figure 3.3. Figures 3.4a and 3.4b are presented for 1.064 μm and 0.532 μm, respectively. In each figure the experimental values are normalized with respect to the maximum. For both cases there is a good agreement between the theoretical prediction and the experimental results. It should be remarked that, while the theoretical curves represent the absorption in water, our experimental results are more truly the attenuation as defined by Equation 3.1, since scattering is also included [128]. Therefore, small discrepancies between theoretical values as predicted by Equation (2.1) and experimental values are expected.

As can be seen in Figure 3.4a, the normalized amplitude decay agrees almost perfectly with the theoretical one, while in Figure 4.3b there is a difference between the two curves that reaches a maximum of 20% at 203 mm water level. This higher discrepancy in the visible spectrum is consistent with what it is found in literature and can be explained with the fact that

the absorption coefficients in the green region are much smaller compared to the IR region. Furthermore, in contrast with what is found in literature, we did not used purified water since our aim was clearly not to calculate the pure absorption coefficients in water but to verify the impact of water depth and laser wavelength in real NDT application of immersed targets.

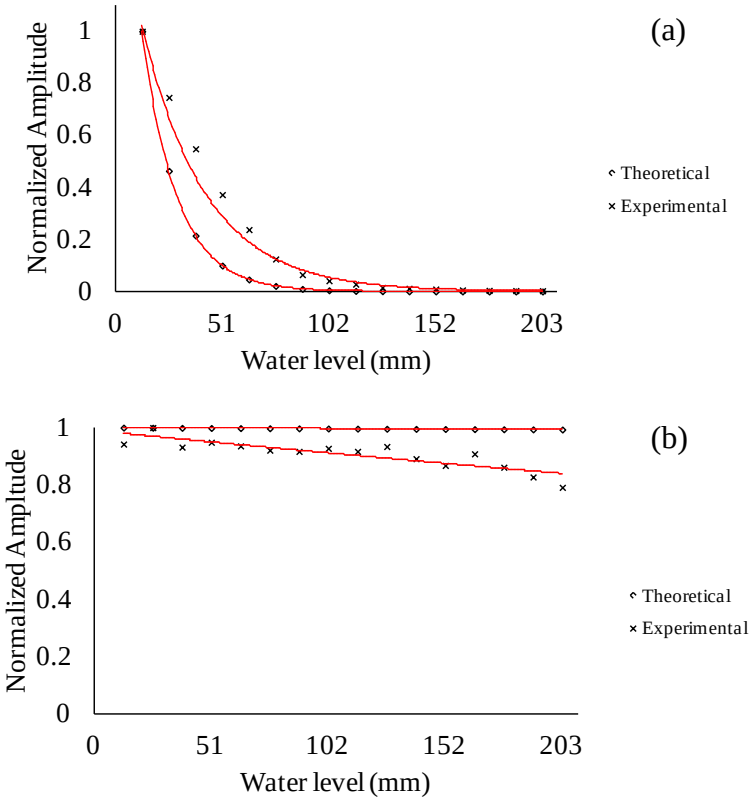

Figure 3.4. Normalized theoretical and experimental averaged peak-to-peak amplitude as a function of the water level. (a) 1.064 μm and (b) 0.532 μm.

By extrapolating the absorption coefficient from our experimental data, we obtain α=0.033 for the 1.064 μm case and α=0.0008 for the 0.532 μm case. In literature these value are compared to α=0.6056 for 1.064 μm and to α = 0.0003539 for the 0.532 μm case [123]. Clearly a direct comparison between our and the literature data cannot be attempted, as our data have to take into account other variables, including the net stress induced on the surface to generate the ultrasound, the attenuation of the bulk wave as it travel across the object thickness and the fact

that we did not used purified water. Nonetheless, our results respect the theoretical prediction of water absorption. Thus, the green light is the most effective at laser generation in underwater applications.

To further investigate the effect of laser wavelength on the characteristics of the laser-generated ultrasonic waves, we then studied higher levels of laser energy, since this could lead to an increase in amplitude [33]. Even though this is not optimal because higher energy could lead to an increased surface damage, we performed a new set of tests where we employed four levels of laser energy for both wavelengths in order to investigate the advantages of varying laser-energy levels in real applications of immersed targets.

The same set-up adopted for the previous experiment was used to investigate the effect of laser energy on the peak-to-peak amplitude at a fixed water level. In particular, the level of the water column in the pipe was kept constant at 50.8 mm and the water was at ambient temperature (22°C). We chose four values of nominal laser energy for the 1.064 μm wavelength and we adopted the correspondent energy level for the 0.532 μm wavelength so that the results are comparable. In particular, we chose 160 mJ, 170 mJ, 180 mJ,190 mJ for both wavelengths. Figure 3.5 shows the energy level versus the peak-to-peak amplitude of the laser-generated bulk waves for the case of 1.064 μm wavelength (Figure 3.5a) and for the case of 0.532 μm wavelength (Figure 3.5b). In both cases, a good repeatability of the tests was proven. As expected, in the visible region the repeatability is less efficient, due to scattering [33], and the amplitude increase is much more evident, since light absorption is lower. Nonetheless, as can be seen, for both cases, an increase in laser energy does not result into a significant increase in amplitude. Furthermore, even though at the same energy level the signal amplitude is lower in the visible region, after 40 mJ step the amplitude of the signals generated with the 0.532 μm is

almost 40% more than the signals generated with the 1.064 μm laser pulse. Thus, it is possible to partially compensate higher water depths and consequent lower signal amplitudes with an increase in laser energy. However, this has also to be carefully balanced with the risk of surface deterioration.

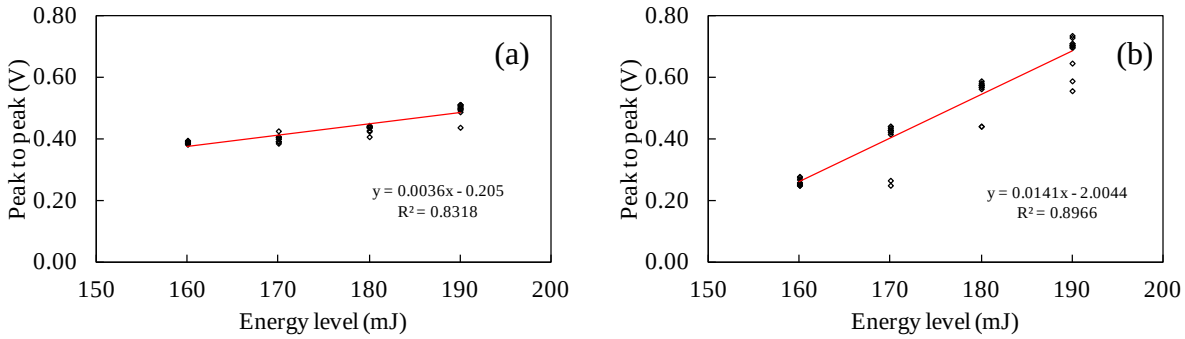

Figure 3.5. Effect of laser energy for 1.064μm wavelength (a) and for 0.532μm wavelength (b).

As a conclusion on these series of tests we can say that the 0.532 μm is the most effective wavelength to employ for the NDT investigation of underwater structures by means of laser ultrasound due to low water absorption. As far as the laser energy is concerned (for the 0.532 μm), levels between 160-190 mJ are a good tradeoff between higher signal amplitude and low surface deterioration.

3.4 EFFECT OF WATER TEMPERATURE. RESULTS AND DISCUSSION

In order to evaluate the effect of the water temperature on the characteristics of the laser-generated bulk waves, we used the same setup described in the previous section. Pulses at 0.532 μm travelled through a column of 100 mm of water cooling from 62 °C to 25 °C. The

temperature of the water column was monitored by means of a thermocouple and ten measurements were taken at each degree Celsius.

Figures 3.6a and 3.6b shows one time waveform recorded at 62 °C and at 25 °C, respectively. The arrival of the longitudinal wave is clearly visible. The peak-to-peak amplitude as a function of the water temperature is displayed in Figure 3.6c. The dots are the averaged value of the ten measurements and the vertical bars are equal to twice the standard deviation. As the temperature increases, the peak-to-peak amplitude of the ultrasound decreases. Equation (2.4) predicts that net stress σ generated against the sample increases as the temperature of the material increases. In the context of this experiment, the parameters in Equation (2.4) are related to the water. As such, T_v = 100 °C and T_0 is the temperature of the water column. However, our results disagree with the theoretical prediction as the amplitude of the bulk wave increases with the temperature decrease. It should be concluded that the intensity of the irradiated pulse increases with the temperature decrease. This can be attributed to the optoacoustic effect. Patel and Tam proved that the coefficient of thermal expansion β is temperature-dependent and this affects the optoacoustic phenomenon [128]. Specifically, above 4°C the thermal expansion coefficient is proportional to the temperature increase. As proved by Equation (2.5), the amplitude of the optoacoustic signal, and consequently the intensity of the laser light converted into the signal, is directly proportional to the coefficient of thermal expansion. Therefore, we speculate that the intensity of the laser light irradiating the surface decreases towards higher water's temperature. Moreover, as metals are excellent conductors, we speculate that a nanosecond laser pulse can diffuse through a portion of the subsurface material that is directly proportional to the surface's temperature. The thermal equilibrium between the solid's

subsurface and the water increases the deformability of the aluminum, which in turn hinders the laser ablation.

In order to assess the effect of temperature on the overall shape and frequency spectrum of the bulk waves, Figures 3.6d-3.6f are presented.

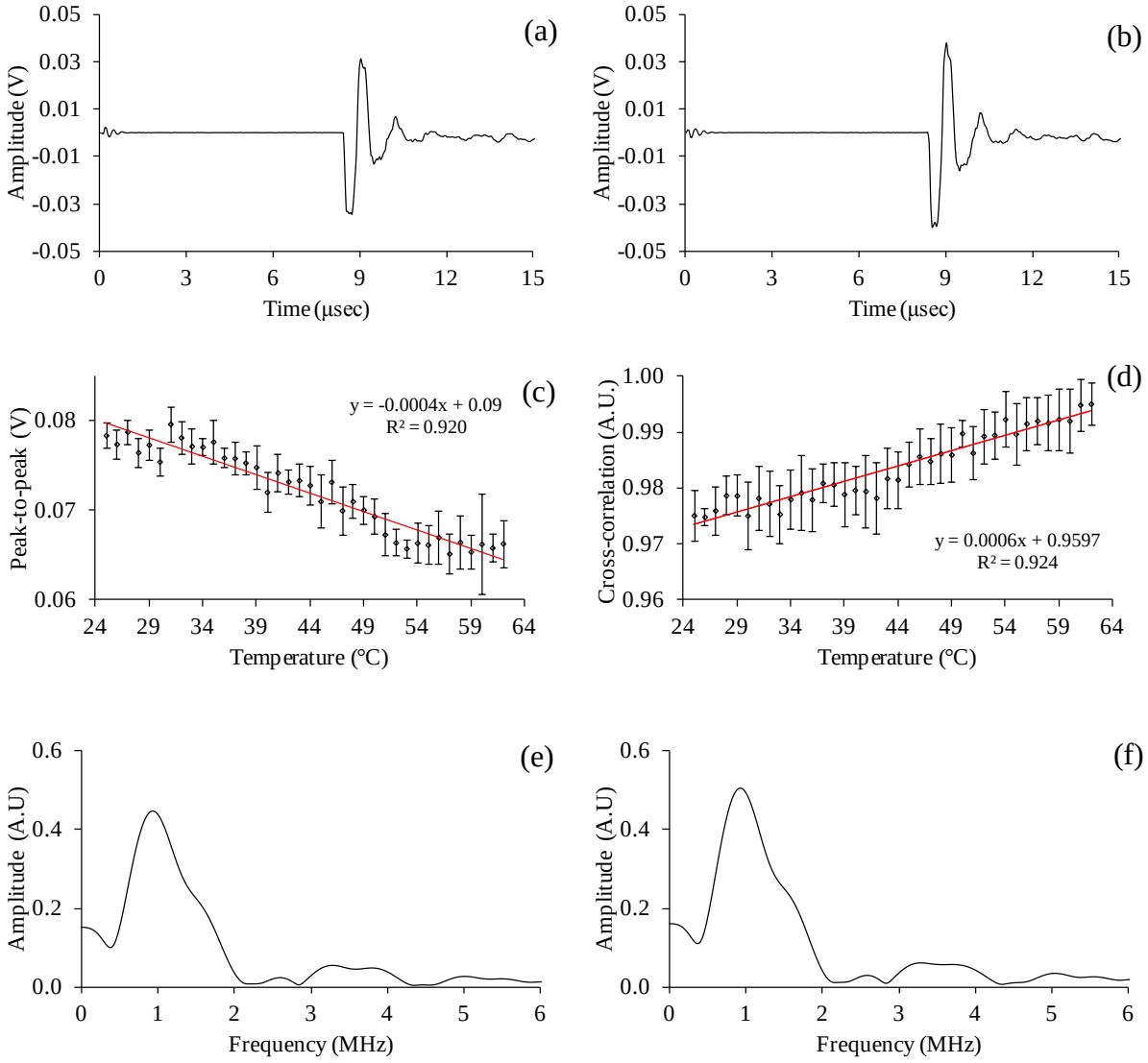

Figure 3.6. Laser-generated time waveforms recorded at (a) 62 °C and (b) 25 °C. (c) Average of the peak-to-peak amplitude as a function of the water temperature. (d) Average of cross-correlation as a function of the water temperature. (e), (f) FFTs of the time waveforms displayed in Figure 3.6a and 3.6b, respectively.

Specifically, Figure 3.6d shows the cross-correlation of the detected bulk wave. The analysis was conducted by considering the average time waveform computed at the highest temperature, i.e., 62 °C, as the reference signal. The vertical bars are equal to twice the standard deviation. As the cross-correlation across the temperature range is closed to one, we can conclude that the temperature has no significant effect on the shape of the time waveforms. The same conclusion can be drawn by examining the spectrum of the recorded signals. Figures 3.6e and 3.6f show the frequency spectrum of the signals shown in Figures 3.6a and 3.6b, respectively.

The signal is dominant at 1 MHz, which represents the resonant frequency of the commercial transducer. Not shown here, the frequency content of the signal remains regular and is not affected by the variation of temperature in the water. In agreement with the peak-to-peak analysis, the amplitude at the frequency peak increases as the temperature.

3.5 EFFECT OF WATER PRESSURE. RESULTS AND DISCUSSION

To evaluate the effect of the water pressure on the amplitude of the laser-generated bulk waves, we devised the setup shown in Figure 3.7. A pressure generator (Figure 3.7a) was connected to the pressure chamber shown in Figure 3.7b (front view) and Figure 3.7c (side view) by means of a hose. The pressure chamber consisted of two thick steel plates bolted together to hold a third steel hollow block able to accommodate the liquid under pressure. In order to allow the irradiation by the laser pulses, a high-pressure borosilicate glass, shown in Figure 3.7b, was used. On the opposite face of the block, a 1 MHz ultrasonic transducer, 0.5” in diameter was bonded

(Olympus NDT, V103-RM, Part ID: U8403008). The liquid pressure was measured using a pressure gauge, as shown in Figure 3.7a.

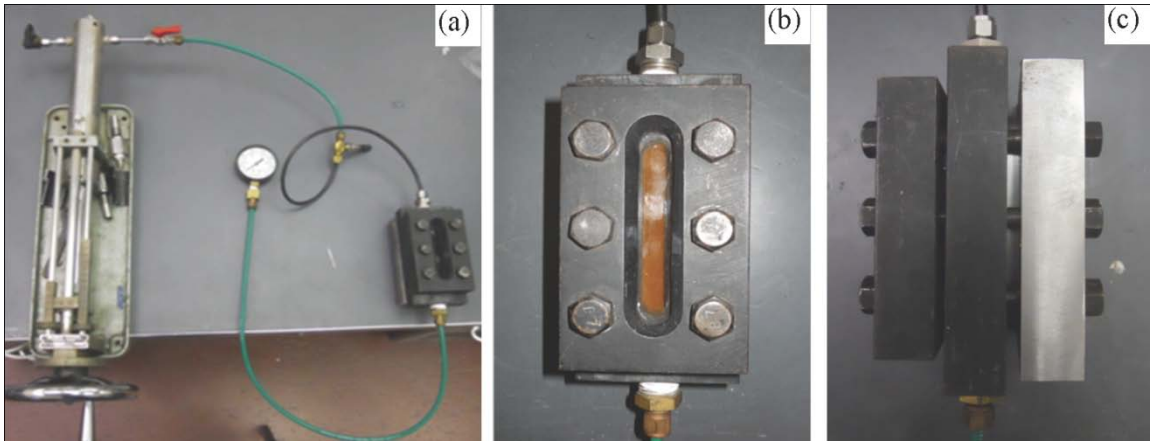

Figure 3.7. Effect of pressure. Experimental setup. Photo of (a) the pressure generator and the pressure chamber (b) front view, (c) side view.

A 0.532 μm, 7 mm diameter laser pulse was used. The beam was kept purposely unfocused to prevent any damage of the glass. The laser intensity was approximately 5.5×10^7 W/cm^2. Ten measurements were taken by turning the handle of Figure 3.7a and varying the pressure at 12 pressure levels ranging from 0 atm to 7.6 atm (7.7 bar) at 0.69 atm (0.7 bar) steps, as indicated by the pressure gauge. We performed this experiments three times. We first measured the effect of pressure on the laser-generated waves irradiating a single spot of the steel block face but increasing the level of pressure, starting at 0 atm up to 7.6 atm. We then chose another spot on the steel block but we decreased the pressure, from at 7.6 atm to 0 atm. Finally, we performed a third experiment at zero pressure, to investigate any effect associated with surface deterioration of plasma trapping. We repeated the experiment three times because we wanted to discriminate the effect of pressure order (ascendant or descent) from pure consequential laser impinging on the amplitude of the laser-generated waves.

Figure 3.8 shows the normalized amplitude of the stress waves as a function of pressure. Figure 3.8a refers to the first experiment when the pressure was raised. Figure 3.8b shows the results obtained when the pressure was decreased from 7.6 atm to 0 atm and Figure 3.8c shows the normalized amplitude of the stress waves as a function of the number of pulses at zero pressure.

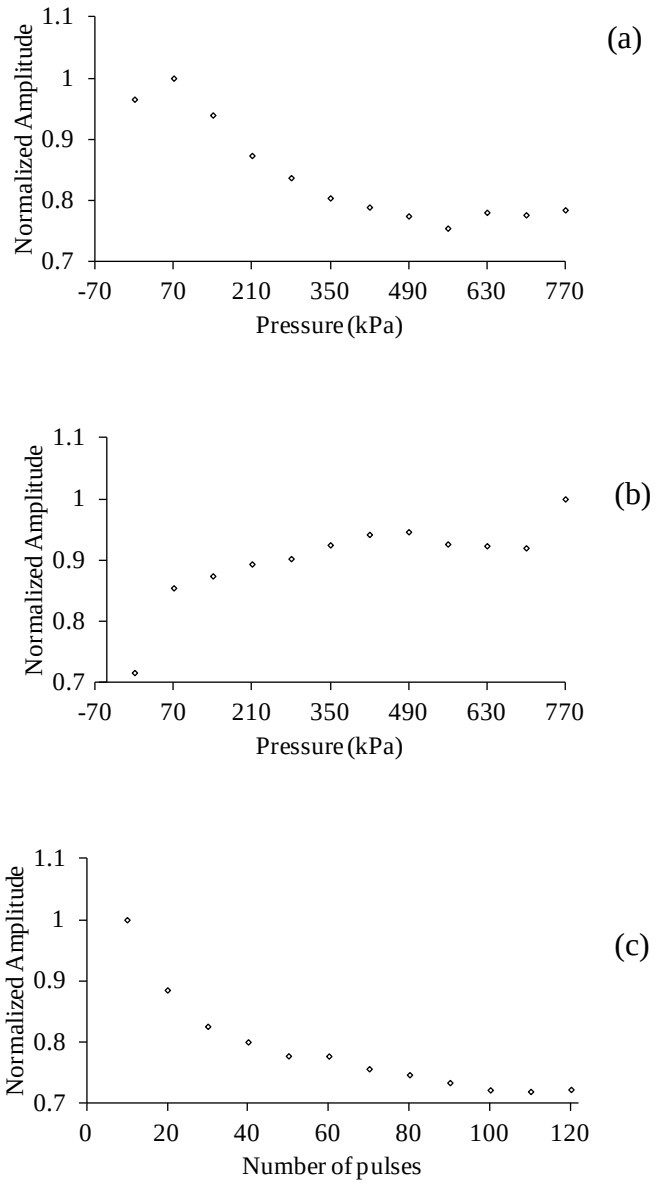

Figure 3.8. Peak-to-peak average as a function of the water pressure. (a) Low to high pressure, (b) high to low pressure,(c) peak-to-peak average as a function of the number of pulses.

Overall, there is a decay of the wave' peak-to-peak amplitude as the pressure increases. If we consider Figure 3.8c as representative of the effect of pure ablation, i.e., at zero pressure, we see that the signal's amplitude decreased as the number of pulses increased. If we define the ablation rate as the thickness of the ablated layer during the pulse, it has been shown by Stafe *et al.* that the ablation rate decreases almost exponentially with the pulse number [152]. This phenomenon can be mainly explained with the fact that plasma is trapped inside the craters that are formed during the ablation process and since plasma is not transparent, its absorption coefficient is increased during this process, thus also transforming the plasma in a shielding layer over the specimen. In turn, this produces a decrease in the laser efficiency and so in the waves' amplitude as a consequence of laser absorption. In Figure 3.8c, we observe a loss in the peak-to-peak amplitude close to 30%. A similar trend is observed in Figure 3.8a. However, in this case, the decay of the waves' amplitude is about 25%.

We can conclude that pressure has some influence on the amplitude of the laser-generated waves and this can be attributed to the fact that the pressure increases the water's vaporization temperature. This implies that, at higher pressures, larger amount of laser energy is necessary to ablate the same amount of water molecules.

3.6 CONCLUSIONS

In the study reported in this chapter we investigated the effect of certain water parameters on the amplitude and frequency of ultrasonic waves generated in pseudo-immersed structures by means of laser pulses. The aim is to understand to which extent these parameters affect the ability to inspect immersed plates by means of LUTs. First, the effect of the distance traveled by

laser light at 1.064 μm and 0.532 μm was studied and compared with the theoretical prediction associated with the coefficient of absorption. The experiment demonstrated that high energy laser pulses can be remotely used to induce stress waves across solid materials immersed in water. In particular, we found that the amplitude of the signal excited by means of the 0.532 μm pulse remains unaffected as the distance traveled by the laser through water increases from few millimeters to 200 mm. As such, the 0.532 μm can be successfully used to generate laser pulses on immersed structures while 1.064 μm can't, being totally absorbed after few millimeters. We then demonstrated that a good laser-energy range in practical applications is 160-190 mJ. In fact, this range is a good balance between high-amplitude laser generation and low surface deterioration.

Then, we found that the amplitude of the laser-generated bulk waves increases as the water temperature decreases. This can be attributed to the optoacoustic signal that increases with temperature owing to the thermal expansion coefficient of water associated with the passage of light. Finally, we found that the increase of pressure determines a decrease in the ultrasonic signal amplitude. The outcome of this experiment, however, cannot be conclusive as we believe that the formation of plasma and slight degradation of the material surface may have hindered the laser ablation, and therefore the net stress transmitted to the test object. However, the change in amplitude of the ultrasonic signals due to both temperature and pressure, for the ranges inspected, is moderate. Thus, neither an increase of temperature/ pressure in the range investigated will deviate the results from normal conditions, i.e., the amplitude and the SNR of the laser-generated waves will not deteriorate. Further studies may be suggested in case of severe changes of temperature or pressure to ensure the same ability of inspecting immersed plates by LUTs.

4.0 NONCONTACT MONITORING OF IMMERSED PLATES BY MEANS OF LASER-GENERATED ULTRASOUND

This chapter presents a study where the ability of a noncontact system to inspect an immersed aluminum plate using leaky Lamb waves was investigated. In particular, we present the results of two experimental studies where guided ultrasonic waves were used for the structural health monitoring / nondestructive evaluation of an immersed aluminium plate. Leaky Lamb waves were generated by means of a pulsed laser and detected by an array of immersion transducers. The signals were then processed using continuous wavelet (CWT) transform to extract few damage-sensitive features that were fed to an unsupervised learning algorithm based on outlier analysis. In order to assess the capability of the monitoring system to detect damage, two setups were devised. In the first, four defects were devised on the plate prior to the immersion in water and four immersion transducers arranged in a cross array were used to detect the leaky Lamb waves. In the second, five defects were devised on the plate prior to the immersion in water and five immersion transducers arranged in a half-moon array were used to detect the leaky Lamb waves. For each test, a different unsupervised algorithm was developed based on varying damage-sensitive features. For sake of completeness, we also include in this chapter a numerical study conducted by Mr. K. Li, a graduate student in our laboratory, which simulated the setup using commercial finite element software to predict the time of arrival of the propagating modes. We found that the non-contact probing system and the signal processing enable the detection of

cracks and holes. The content up to Chapters 4.4 is largely excerpted from a paper of Pistone et al. [161].

4.1 METHODOLOGY

The waves were generated by means of short duration (~8 nsec) laser pulses and detected by an array of ultrasonic immersion transducers. We exploited the optical transparency of water to induce broadband stress waves directly onto the plate. To enhance the detection and location of a few damages artificially devised, we adopted a signal processing strategy based on CWT and outlier analysis. The wavelet transform was used to extract certain damage-sensitive features from the time, the frequency, and the joint time-frequency domains of the ultrasonic signals. These features were then coupled to an unsupervised learning class algorithm able to determine the severity and the location of the defects. To portray the physical phenomenon expected in the experiments, we created a model using the commercial finite element software ANSYS. Moreover, the ANSYS simulation allows visualizing the interaction that occurs between the leaky waves and the bulk and quasi-Scholte waves that propagate in the bulk fluid and along the solid-liquid interface, respectively.

4.2 NUMERICAL SYMULATION

To portray the propagation of waves generated on a plate surrounded by water, a time-transient analysis was run using the commercial finite element software ANSYS v13.0. The effectiveness

of finite elements to simulate the propagation of elastic guided waves in structural waveguides was demonstrated by many researchers [78][102][153-156]. In our analysis the time step resolution ΔT and the finite element length L_e satisfied the conditions [157]:

$$\Delta t \leq \frac{1}{20 f_{\max}} \tag{4.1}$$

$$L_e = \frac{\lambda_{\min}}{20} \tag{4.2}$$

where $f_{\max}$ and $\lambda_{\min}$ were the highest frequency and the shortest wavelength of interest, respectively.

We modeled this system as a plane strain problem. The plate was discretized using the two-dimensional 4-node "PLANE42" element having two degrees of freedom per node. The properties of the aluminum were: density ρ=2700 kg/m^3, Young's modulus E=69 GPa, and Poisson's ratio ν=0.33. The water was meshed using two-dimensional 4-node "FLUID29" element having pressure as the only degree of freedom per node. The boundary conditions at the fluid-solid interface were guaranteed by using the appropriate ANSYS flags. Thus, at the solid-liquid interface the two fields are coupled. Free boundaries were applied to the other water edges while the right plate edge was constrained in the x direction. In the liquid domain, the FLUID29 elements had only the pressure degree of freedom while, at the solid-liquid interface, displacements perpendicular and parallel to the plate were allowed for the same elements [158]. An unconditionally stable implicit Newmark procedure with a decay factor of 0.005 and integration parameters α=0.252 and δ=0.505 was used to perform the time integration. The integration time step was 0.1 μsec [159].

4.2.1 Continuous Wavelet Analysis

CWT is used to divide continuous function into wavelets. A wavelet is a function with zero average:

$$\int_{-\infty}^{\infty} \psi(t)dt = 0 \tag{4.3}$$

That can be scaled by s and translated by u:

$$\psi_{u,s}(t) = \frac{1}{\sqrt{s}}\psi\left(\frac{t-u}{s}\right) \tag{4.4}$$

It is possible to calculate the wavelet transform of a signal, 'f(t)', at a specific scale s and position u by correlating the signal with a wavelet atom:

$$Wf(u,s) = \int_{-\infty}^{+\infty} f(t)\frac{1}{\sqrt{s}}\psi^*\left(\frac{t-u}{s}\right)dt \tag{4.5}$$

In 1946 Gabor defined basic time-frequency atoms as waveforms that have a minimum spread in a time frequency plane. Therefore, to have a measure of the time-frequency content, signals can be decomposed over basic atomic waveforms [160] and so, the wavelet transform decomposes signals over dilated and translated wavelets.

An analytical wavelet can be built with a modulation in frequency of a real and symmetric window g. The Fourier transform of:

$$\psi(t) = e^{i\eta t}g(t) \tag{4.6}$$

is $\hat{\psi}(\omega) = \hat{g}(\omega - \eta)$.

A Gabor wavelet can be defined as:

$$\psi(t) = g(t)e^{i\eta t} \tag{4.7}$$

where g(t) is a Gaussian window of the form:

$$g(t) = \frac{1}{\sqrt[4]{(\sigma^2 \pi)}} e^{-\frac{t^2}{2\sigma^2}} \quad . \tag{4.8}$$

Gaussian windows are used because they provide the best balance between time and frequency concentration, as proved by the Heinsenberg uncertainty Theorem [160].

4.2.2 Simulation of the A_0 Lamb wave propagation in the dry aluminum plate

To calibrate our model, we first simulated a dry plate subjected to anti-symmetric loading. The plate was 600 mm long, 2.54 mm thick (Figure 4.1a). One edge was subjected to the triangular displacement load function shown in Figure 4.1b. Nine elements were modeled through the plate thickness giving a through-thickness element length of 0.282 mm. To enhance the generation of the anti-symmetric modes, the spatial distribution of the load was anti-symmetric with respect to the neutral axis (Figure 4.1c).

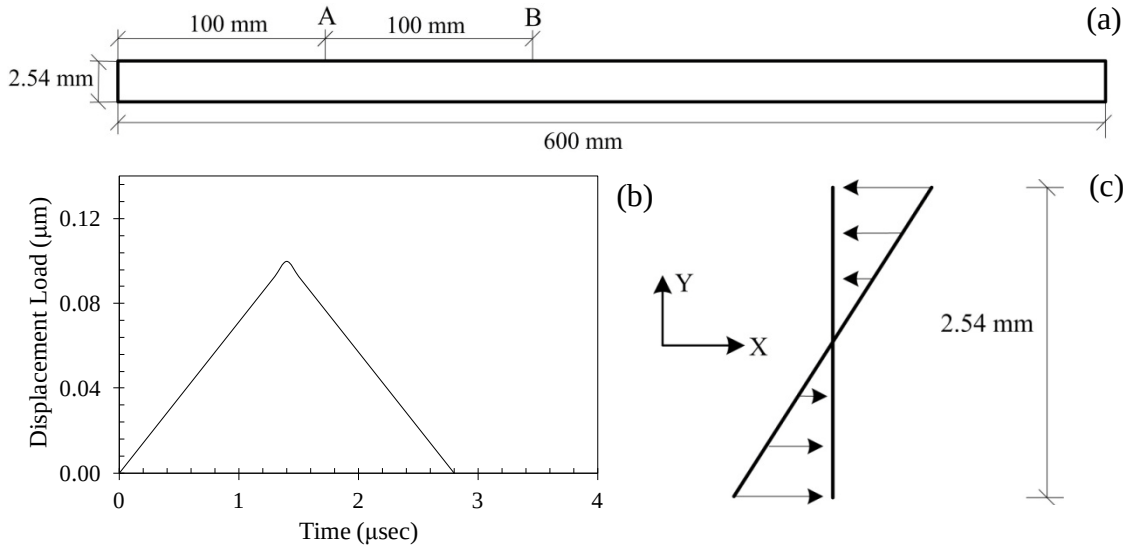

Figure 4.1. ANSYS simulations of Lamb waves in a dry plate excited by an impulse. (a) Sketch of the plate; (b) forcing function in the time domain; (c) spatial distribution of the forcing function across the plate's thickness.[161].

Figures 4.2a and 4.2b show the nodal displacement measured on the plate's surface of the plate 100 and 200 mm from the input, respectively, whereas Figures 4.2c and 4.2d present the corresponding Gabor wavelet transform (GWT). As mentioned, the wavelet transform decomposes the original time-domain signal by computing its correlation with a short-duration wave called the mother wavelet that is flexible in time and in frequency. The transform determines the time of arrival and the frequency content of the propagating modes. We used the Gabor mother wavelet as it provides the best balance between time and frequency resolution, i.e., the smallest Heisenberg uncertainty box [160]. Owing to the time of arrival and the dispersive behavior observed in the scalograms, the A_0 mode was identified.

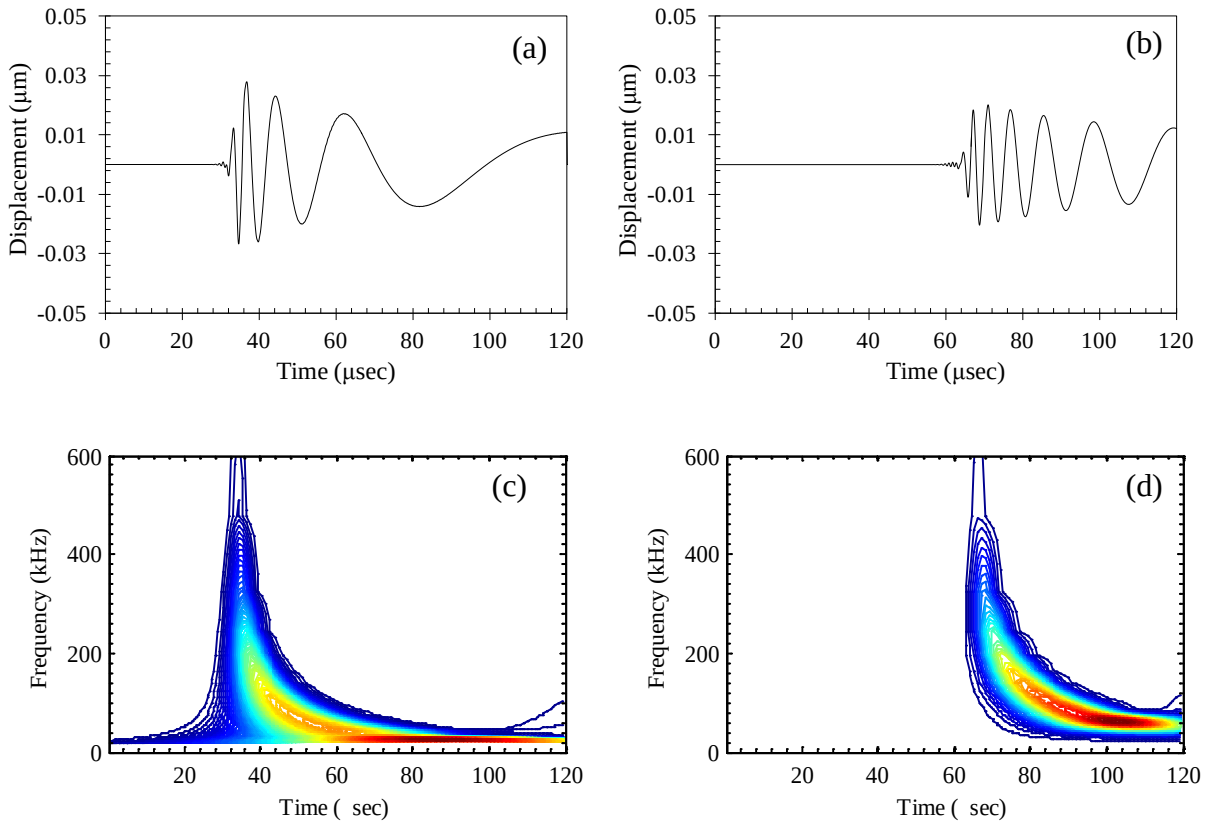

Figure 4.2. ANSYS simulations of Lamb waves in a dry plate excited by an impulse. Nodal displacement at (a) node A and (b) node B. Gabor wavelet scalograms associated with (c) node A displacement and (d) node B displacement [161].

By using a methodology outlined elsewhere [96][157], the numerical dispersion curves associated with the propagating modes were extracted. Figure 4.3 compares this curve with the group velocity dispersion curve obtained using the SAFE approach [157]. By looking at the plot, the A_0 curve obtained with our FE model agrees very well with the A_0 curve obtained with the SAFE method.

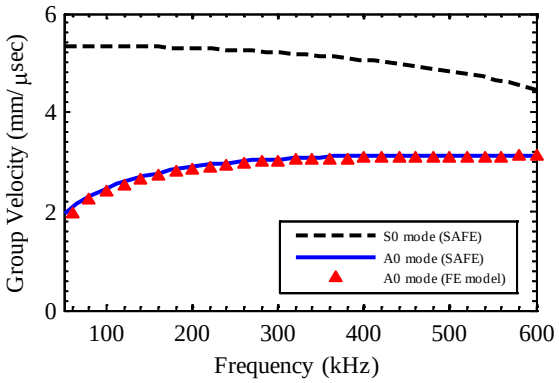

Figure 4.3. SAFE dispersion curves for an h=2.54 mm thick Aluminum 6010 plate (density ρ=2700 kg/m3, Young's modulus E=69.00 GPa, shear modulus G=25.94 GPa, Poisson's ratio ν=0.33). Courtesy of Mr. Abdollah Bagheri.

4.2.3 Simulation of the anti-symmetric Lamb wave propagation in the immersed aluminum plate

We then simulated the same plate surrounded by 30 mm of water above and below to predict the pressure field in the fluid generated by the laser induced ultrasounds and to overall portray the propagation of the guided waves along the plate, their leakage into water, and the propagation of the quasi-Scholte mode and the bulk waves. Most of the finite element simulations carried out using commercial software, as it is reported in the literature, considers only the propagation of the wave along the solid even if the solid is surrounded by fluid. With our simulations we

determined the pressure field in the liquid surrounding the solid. This is the field measured using the immersion transducers, and it is eventually the result of the interaction among different kind of waves. Moreover, the detection of leaky Lamb waves either if the surrounding medium is solid or liquid, is dependent on their amplitude which, in turn, is affected by the wave structure of the modes [40][78][79][94][162][163].

Figure 4.4 shows the dispersion curves for an aluminum plate immersed in water that was used as reference to understand the various types of waves that were depicted by our numerical model. In particular, Figure 4.4a shows the phase velocity and Figure 4.4b shows the group velocity of a 2.54 mm aluminum plate in dry conditions.

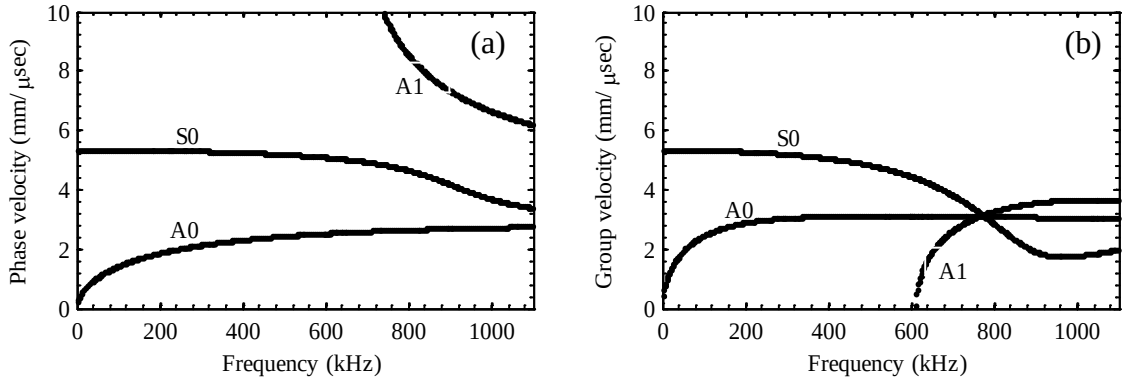

Figure 4.4. (a) Phase velocity dispersion curve of the 2.54 mm thick aluminum plate in dry condition. (b) Group velocity dispersion curve of the 2.54 mm thick aluminum plate in dry condition. Courtesy of Mr. A. Bagheri.

In this simulation, the same loading conditions illustrated in Figure 4.1b were applied. Figure 4.5a shows the contour map of the pressure in the water at 50 μsec where the waves are visible. The fastest wave with center frequency at 900 kHz has group velocity of 3.0 mm/μsec and phase velocity of 6.0 mm/μsec, and it is the A_1 mode leaky Lamb wave according to the phase and group velocity dispersion curve for the same plate in dry condition shown in Figures 4.4a and 4.4b, respectively. The wave packet following the A_1 mode is the quasi-Scholte wave [94]. The

third wave packet with the speed at 1.46 mm/μsec is the bulk wave traveling in water. The A_0 mode is not observed as most of its energy is converted into the quasi-Scholte wave [94]. The Scholte wave is a particular case of the Stoneley wave which propagates at the solid-liquid interface, considering the solid as a semi-infinite media. The quasi-Scholte wave behaves very similarly to the Scholte wave at high frequencies, i.e., the wave energy will decay exponentially away from the surfaces at a faster rate since the wavelength decreases with higher frequency. However, at low frequencies, it has a dispersive behavior. This is caused by the interaction of the top and bottom boundaries of the plate due to the fact that the wave energy will decay at a slower rate with longer wavelength. Figures 4.5b and 4.5c show the nodal displacement at the solid-fluid interface's points A and B, located at 100 mm and 200 mm, respectively, away from the loading source. The waveforms show the quasi-Scholte wave mode while the energy associated with the A_1 mode is too weak to be observed. The discontinuities visible at 70 μsec, 110 μsec and 150 μsec represent the bulk wave and its reflection from the water-vacuum interface. The corresponding GWT scalograms are presented in Figures 4.5d and 4.5e.

To enhance the generation and propagation of the symmetric mode in the wet plate a second simulation was run. In this case, the same time function illustrated in Figure 1b was applied uniformly across the thickness of the plate edge. Figure 4.6a shows the resultant pressure contour map at 50 μsec. The snapshot reveals the dominance of the leaky S_0 mode. Figures 4.6b and 4.6c show the nodal displacement at the solid-fluid interface's points A and B. The wave packets at 55 μsec and 95 μsec are reflections of the Leaky S_0 mode from the water edge. The corresponding GWT scalograms are presented in Figures 4.6d and 4.6e and show the slight dispersive behavior typical of the first symmetric mode, below 600 kHz.

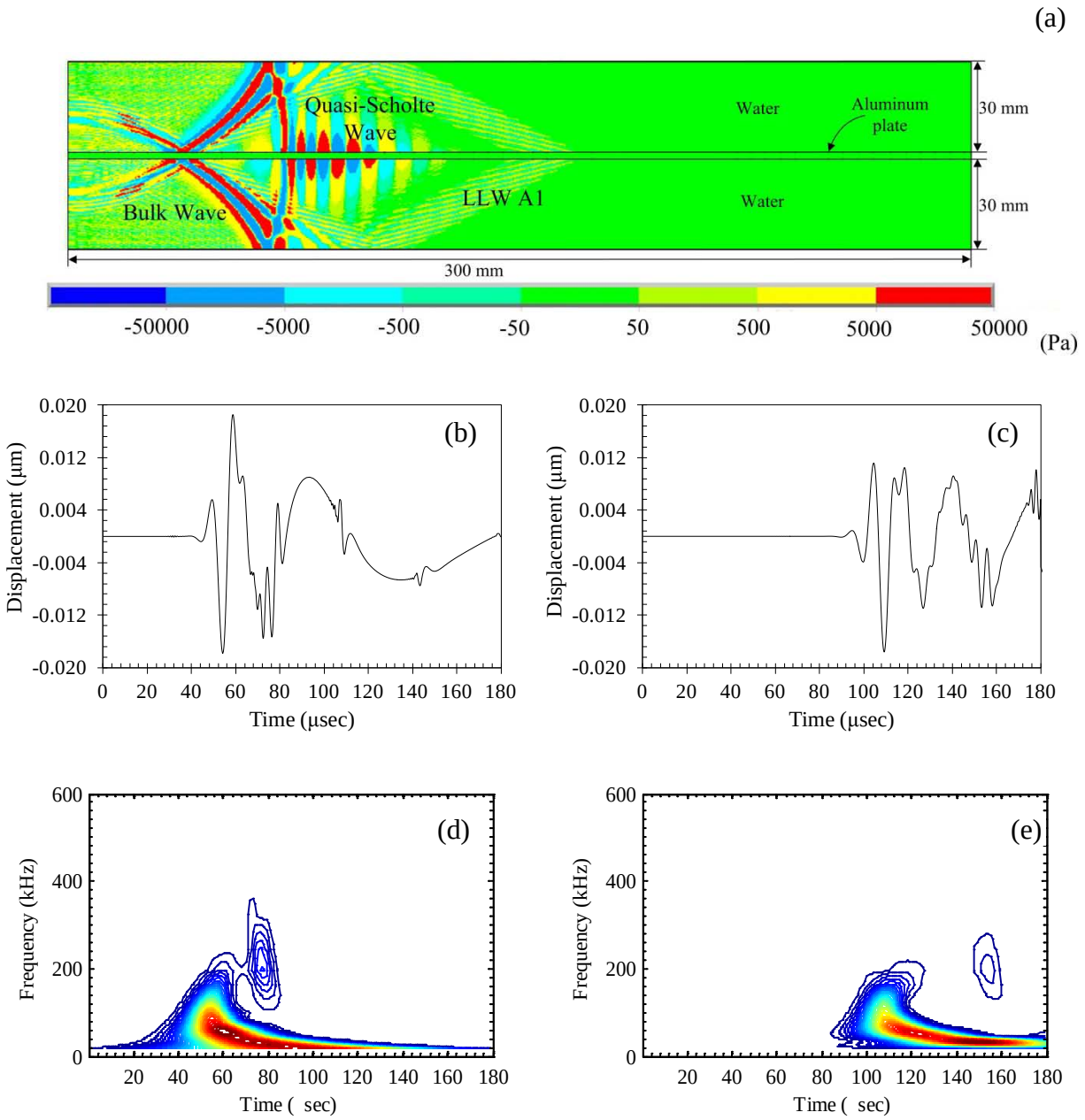

Figure 4.5. ANSYS simulations of waves propagating in a plate subject to an anti-symmetric impulse and surrounded by 30 mm of water. (a) Contour map of the pressure of water at 50 μsec. Nodal displacement at (b) node A and (c) node B. Gabor wavelet scalograms associated with (d) node A displacement and (e) node B displacement [161].

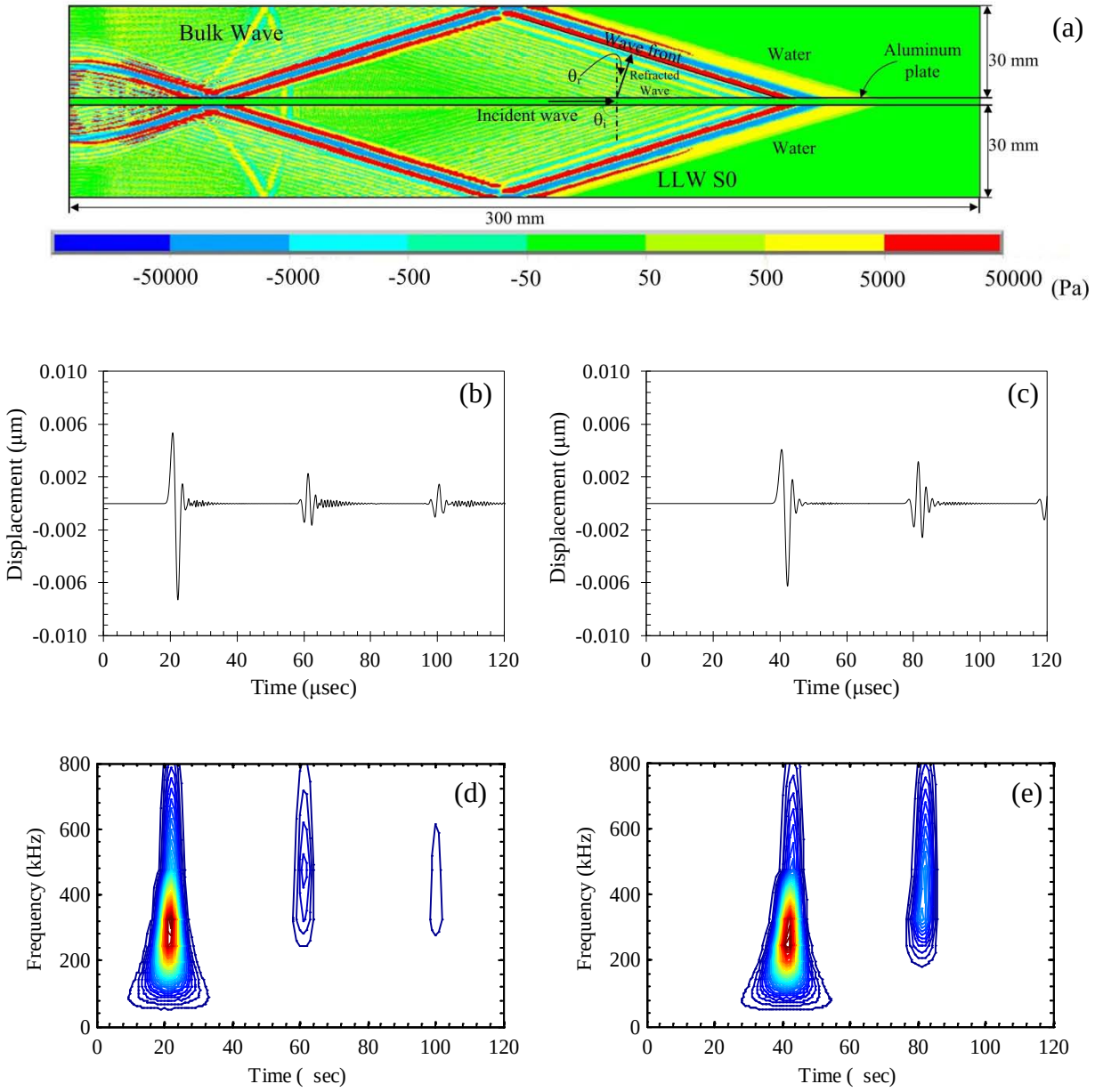

Figure 4.6. ANSYS simulations of waves propagating in a plate subject to a symmetric impulse and surrounded by 30 mm of water. (a) Contour map of the pressure of water at 50 μsec. Nodal displacement at (b) node A and (c) node B. Gabor wavelet scalograms associated with (d) node A displacement and (e) node B displacement [161].

4.3 TEST I – EXPERIMENTAL SETUP

In this experiment a 8 ns Q-switched Nd:YAG pulsed-laser (CFR 200, Quantel USA) operating at 0.532 μm was used to probe an aluminum plate (750 x1605 x 2.54 mm) immersed in a tank filled with water. The nominal level of output energy was equal to 180 mJ. Figure 4.7 shows the experimental setup. A 1 mm diameter laser beam was delivered to the surface of the plate by means of a mirror and a PCX lens with focal length of 100 mm (Newport, KPX094AR.14). Four immersion transducers resonant at 1 MHz were used to receive the laser-generated ultrasound (Olympus NDT, V303-SU, Part ID: U8423005). According to the Snell's law, we inclined them at 15° to maximize the sensitivity to the leaky S_0 mode. We used four preamplifiers (Olympus NDT, Model 5660C) to boost the signals. The location of the transducers and their lift-off distance with respect to the plate are detailed in Figures 4.7b and 4.7c. A foam panel was suspended between the laser and the immersion transducers to attenuate the longitudinal bulk wave traveling directly in water. The plate was positioned on four supports and the level of water above was 65 mm. Figure 4.7d details the location of the supports while Figure 4.7e schematizes the plan view of the setup, showing the position of the four transducers and their relative distance with respect to the laser-illuminated point. A B-scan system was built *in house* to inspect the immersed plate. The system consisted of the laser head and the transducers secured to a movable metallic bench plate. The motion of the bench plate was guaranteed by pulleys and belts connected to a stepper motor (NI MID7602, 4/2 Axis Stepper Motor Drive) and driven by a National Instrument PXI unit (NI PXIe-1062Q). A front user interface, running under LabVIEW, was coded to control the motion of the scan and to select the proper parameters for the generation, detection, and the storage of the ultrasonic waves.

Four defects, displayed in Figure 4.8a, were machined at the locations shown in Figure 4.8b. Defect 1 was a surface notch 1 mm deep, defects 2 and 3 were a through-thickness and a surface hole, respectively, and defect 4 was a surface abrasion that simulated corrosion. In the study presented in this paper, the B-scan was conducted by irradiating 55 points of the plate spaced 20 mm apart and aligned 425 mm from the right edge of the plate.

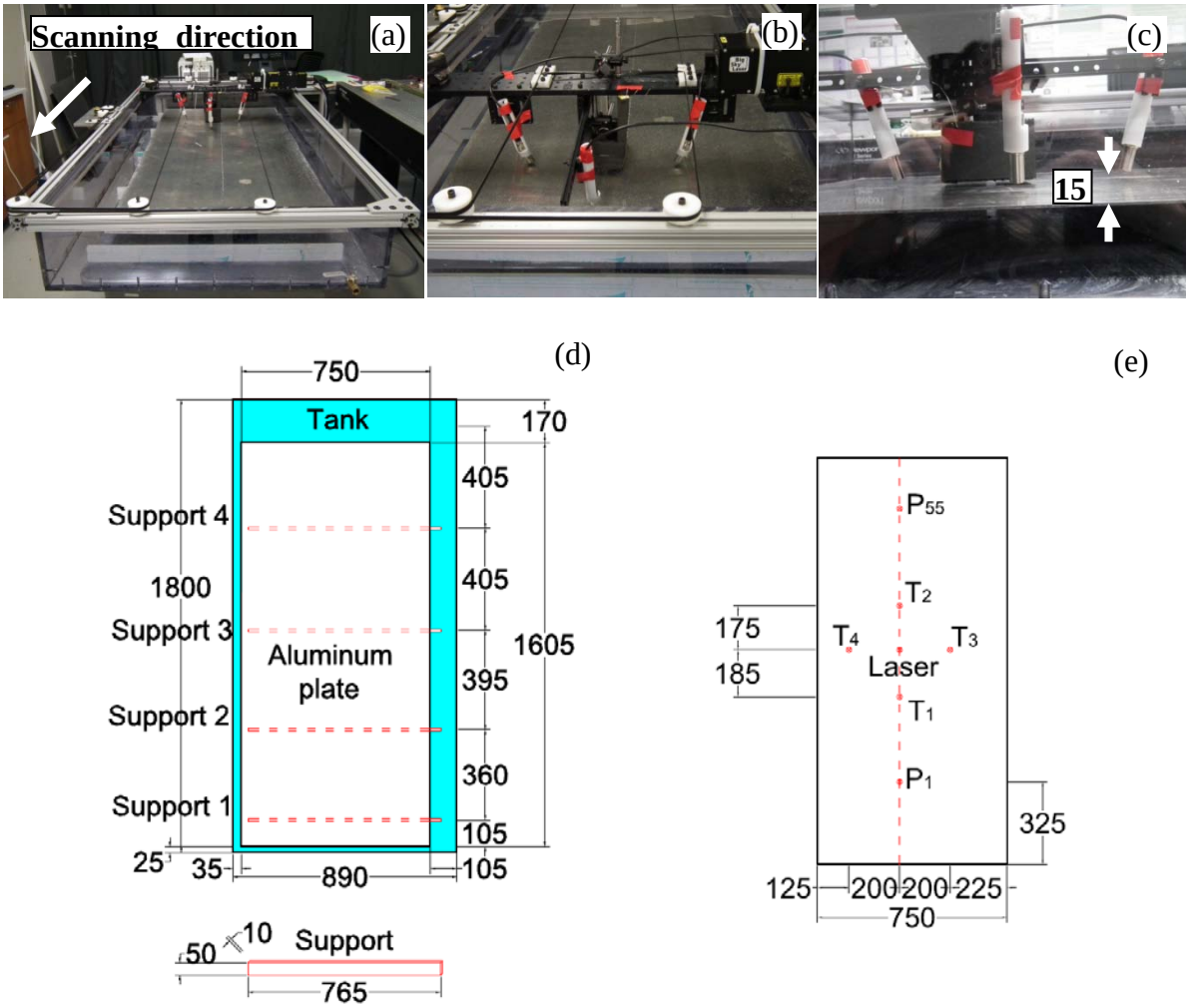

Figure 4.7. Experimental setup. (a,b,c) Photos of the scanning system and close up-view of the ultrasonic transducers, laser and optical system. (d,e) Schematics of the setup. (d) plan view. (e) details of the position of the transducers (T1, T2, T3, T4) and of the irradiated points. The drawings are on scale and all the quotes are in millimeters [161].

To verify the repeatability of the laser-induced ultrasound in water, ten laser pulses were generated at each point. The plate was inspected five times to prove the repeatability of the methodology. Figure 4.8b shows the location of the first and last scanned point, as well as few other key points located close to the artificial defects.

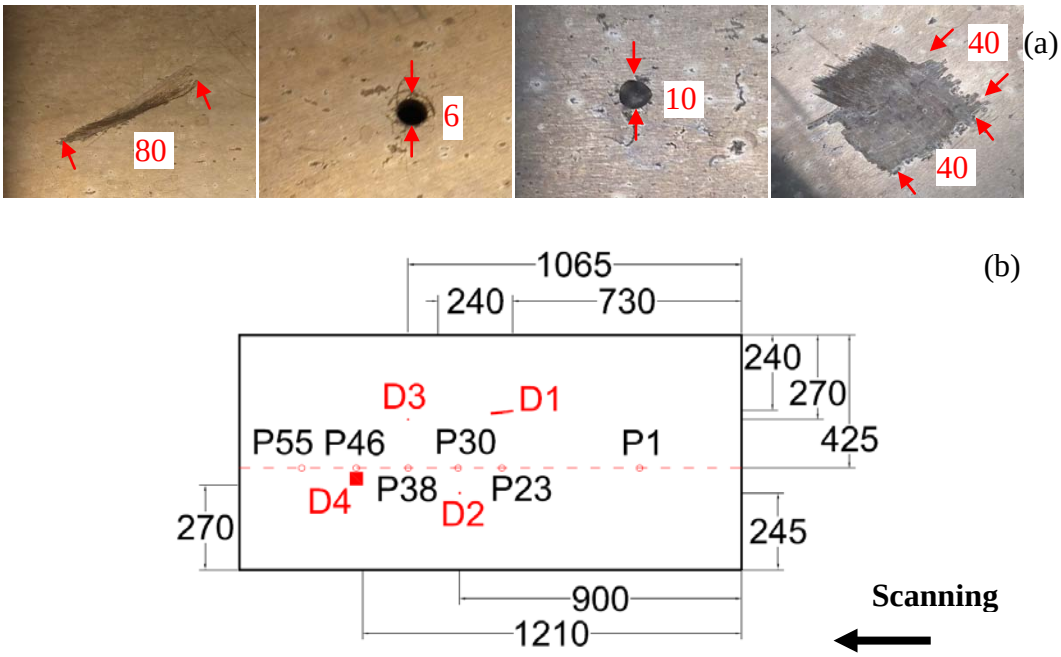

Figure 4.8. (a) Photos of the artificial defects (D1, D2, D3, D4) devised on the plate. (b) Location of the defects and of few laser-illuminated points. The drawing is on scale and all the quotes are in millimeters.[161].

4.3.1 Setup assessment

Figure 4.9 shows the typical time waveforms measured by the four transducers during the experiment. In particular, the four panels refer to the first measurement taken at the scanning point 10 and relative to the first scan. Three wave packets are visible: the first packet at about 40 μsec is the leaky S_0 mode, the second packet comprised between 50 μsec and 65 μsec is likely generated by the interaction of the leaky S_0 mode with the foam and the subsequent solid-liquid and liquid-air interfaces, while the third wave packet beyond 80 μsec is the superposition of the

quasi-Scholte mode and the bulk wave. In this study, we analyzed the leaky symmetric mode being the most repeatable and stable. As such, any signal processing discussed hereafter was conducted on the time window 0-50 μsec.

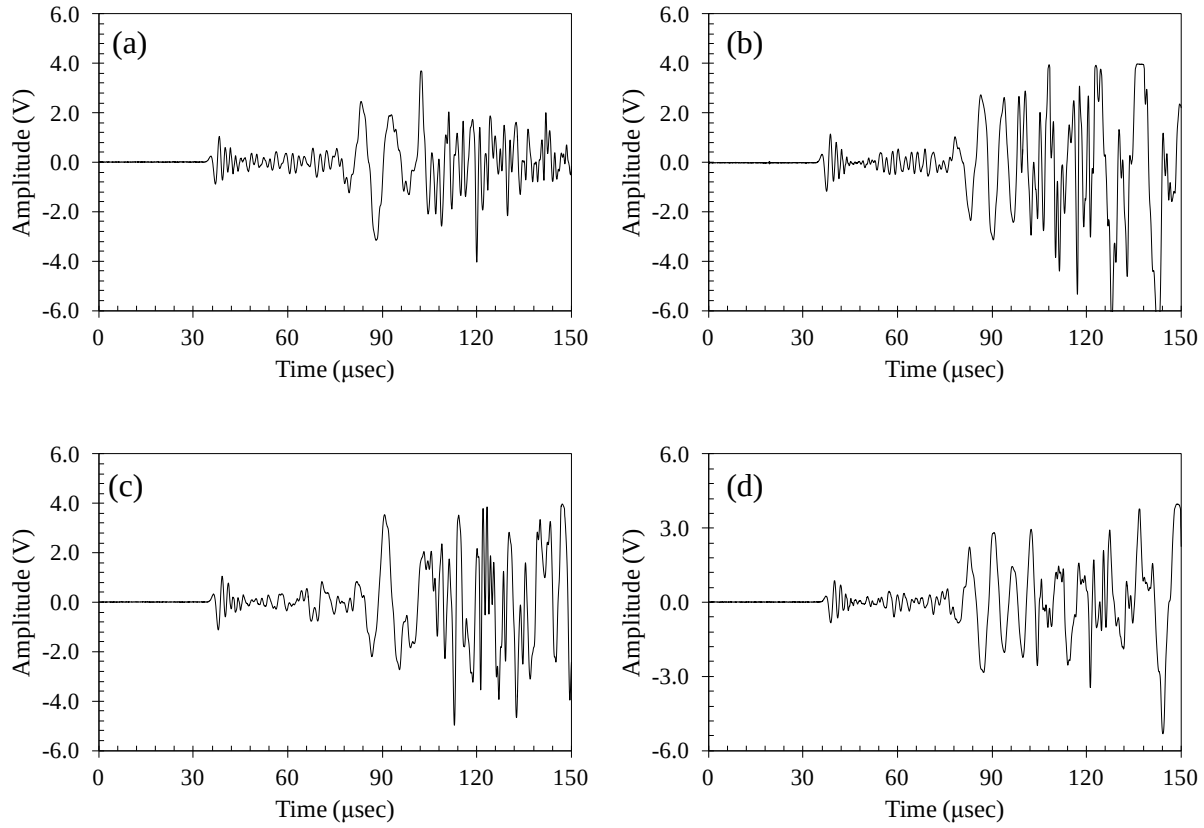

Figure 4.9. Experimental time waveforms by (a) T1, (b) T2, (c) T3, and (d) T4. [161]

Figure 4.10 shows the scalogram of the time waveforms presented in Fig. 4.9 at the time interval 0 – 50 μsec. The scalograms show that the energy of the leaky S_0 mode is dominant in the 200-800 kHz range, with peak located between 400 and 500 kHz.

First, we evaluated the repeatability of the laser-generated signals by adopting the following procedure. We considered the signals from the first scan. For each point and for each transducer, we considered the time waveform associated with the first measurement as a

reference signal, and then we correlated the remaining nine signals to the reference. Figure 4.11 shows the cross-correlation as a function of the irradiated points for the four transducers. The dots represent the averaged value of the cross-correlations and the vertical bars represent the 95.5% (2σ) confidence interval. The panels demonstrate the elevated repeatability of the laser-generated ultrasounds. Isolated scatters are visible, for example at point 33. Although we cannot provide a conclusive justification, we believe that these scattered data might have been caused by air bubbles, made of ionized gas trapped in the water, suspended in the liquid or adherent to the surface of the plate.

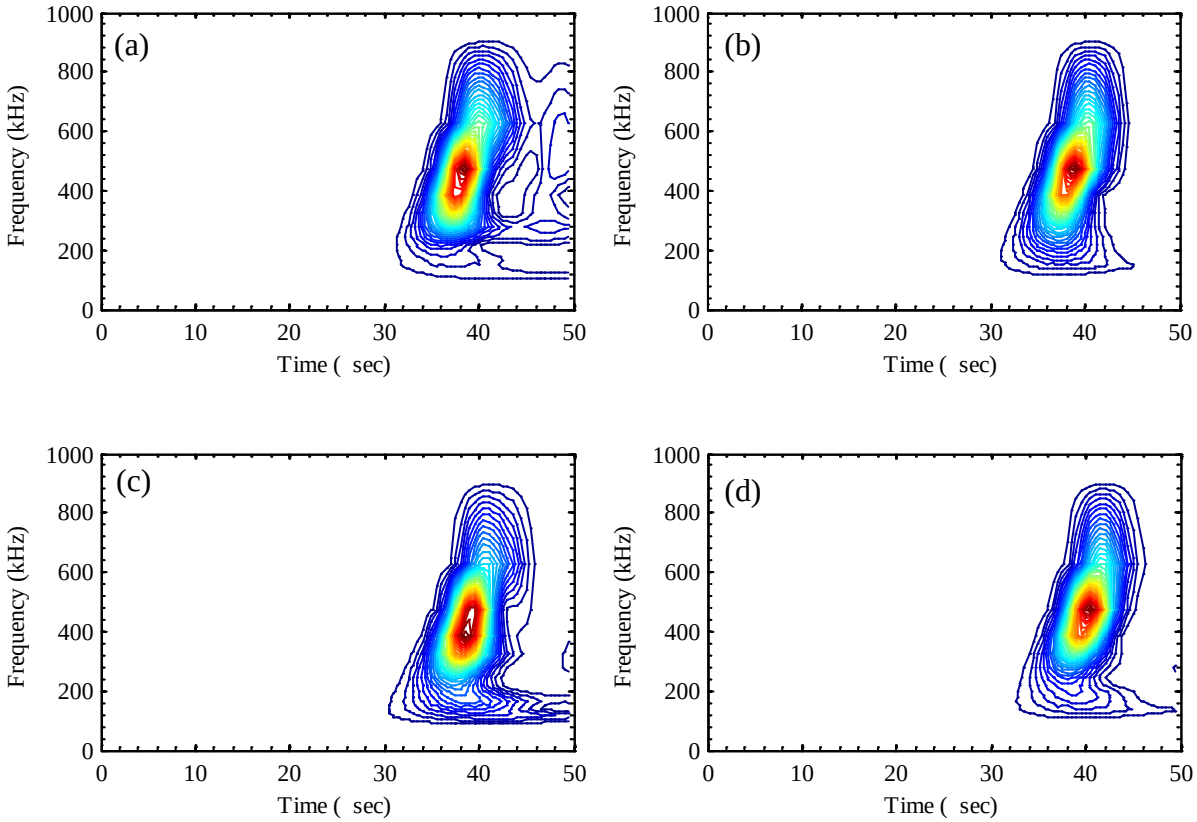

Figure 4.10. Gabor wavelet scalograms associated with the time-waveforms presented in Figure 4.9. [161].

To evaluate the repeatability of the methodology we inspected the plate five times, and we built a reference signal for each scanning point by averaging the ten time-series recorded

during the first inspection. We then calculated the cross-correlation of the time waveforms associated with the remaining four scans with respect to the corresponding reference signal. Figure 4.12 shows the cross-correlation as a function of the scan points for all the scans and relative to all transducers. To ease the readability of the graphs, the average value of the ten correlations is presented only.

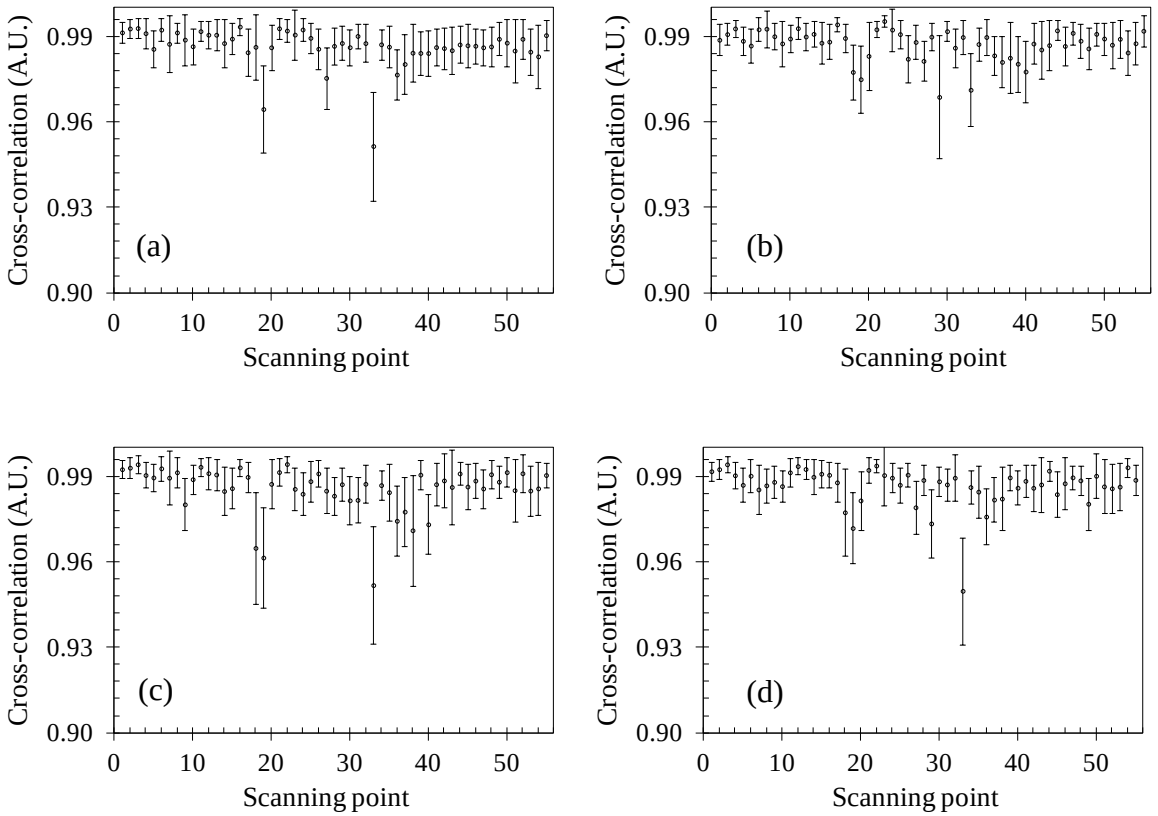

Figure 4.11. Experimental results relative to scan 1. Cross-correlation as a function of the illuminated point (a) Transducer T1, (b) Transducer T2, (c) Transducer T3, and (d) Transducer T4 [161].

As can be seen, the cross-correlation is high, thus confirming the repeatability of the probing system. The scatters visible in Figure 4.12c at point 22 are due to the presence of the notch. By looking at Figure 4.12d, it seems that scan 5 was deteriorated since the values for the cross-correlation were lower compared to the other scans. This decrease in amplitude is most likely due to the presence of air bubbles of ionized gas coalescing around the transducers.

Nonetheless, the values of the cross-correlation are still high. It must also be noted that in real applications, this would be normal as the ionized gases in water are common.

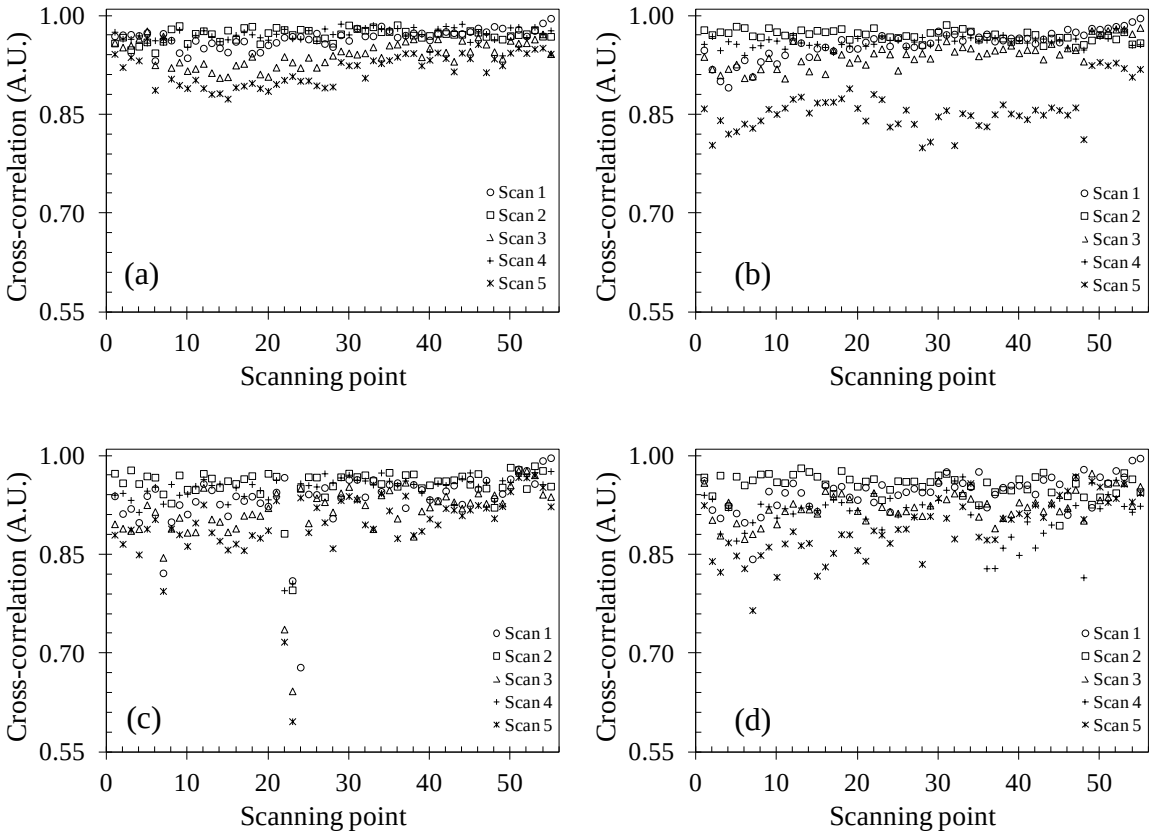

Figure 4.12. Experimental results relative to all scans. Cross-correlation as a function of the illuminated point (a) Transducer T1, (b) Transducer T2, (c) Transducer T3, and (d) Transducer T4 [161].

4.4 OUTLIER ANALYSIS

Outlier analysis is used in SHM as a tool to assess the presence of damage in the structures. The application of outlier analysis for the NDE/SHM of structures was first introduce by Worden in numerous articles [164-167] where he demonstrated the feasibility of the method at detecting the

reduced stiffness in modeled lamped-mass system. Latest applications included, but are not limited to, the detection of damages in plates and multi-wire strands [168][169].

Ying *et al.* studied the applications of machine learning to damage detection in pipes in order to develop a robust damage detection system [170].

An outlier is a datum that appears inconsistent with a set of data, the baseline, which describes the normal condition of the structure under investigation. Ideally, the baseline should include typical variations in environmental or operative conditions (e.g. temperature, humidity, and loads) of the structure [171][172] even though this is not always possible.

In the case where only one-dimensional data are considered, the outlier analysis can be performed computing the discordancy test between the data and the baseline. The most common test of this type is based on the deviation statics z_ζ:

$$z_\zeta = \frac{\left| x_\zeta - \bar{x} \right|}{\sigma} \tag{4.9}$$

where x_ζ is the potential outlier, $\bar{x}$ is the mean and σ the standard deviation of the baseline, which can be both calculated with or without the potential outlier depending upon whether inclusive or exclusive measures are preferred. The value of z_ζ is then compared to the threshold value. If x_ζ is higher than the threshold value, will be categorized as an outlier or viceversa.

When the analysis involves a set of *p*-dimensional (multivariate) data consisting of *n* observations in *p* variables, the outlier analysis can be performed using the Mahalanobis Squared Distance (MSD), D_ζ, which is a non-negative scalar defined as:

$$D_\zeta = (\{x_\zeta\} - \{\bar{x}\})^T \cdot [K]^{-1} \cdot (\{x_\zeta\} - \{\bar{x}\}) \tag{4.10}$$

where $\{x_\zeta\}$ is the potential outlier vector, $\{\bar{x}\}$ is the mean vector of the baseline, *[K]* is the covariance matrix of the baseline, and *T* symbolizes the transpose operation. Both vectors $\{x_\zeta\}$ and $\{\bar{x}\}$ are p-dimensional whereas *[K]* is a square matrix of order p. The baseline vector and the covariance matrix can be calculated with or without the potential outlier depending upon whether inclusive or exclusive measures are preferred. In the present study, as the potential outliers are always known a priori, D_ζ is calculated exclusively without contaminating the statistics of the baseline data. A new datum is an outlier if the corresponding value of D_ζ falls above a set threshold [169]. When the available number of baseline data is limited, it is common practice to compute the threshold based on a Monte Carlo simulation [167][173].

4.4.1 SHM algorithm

For each scalogram as the one presented in Figure 4.10, we computed two subplots that, for illustrative purposes, are shown in Figure 4.13.

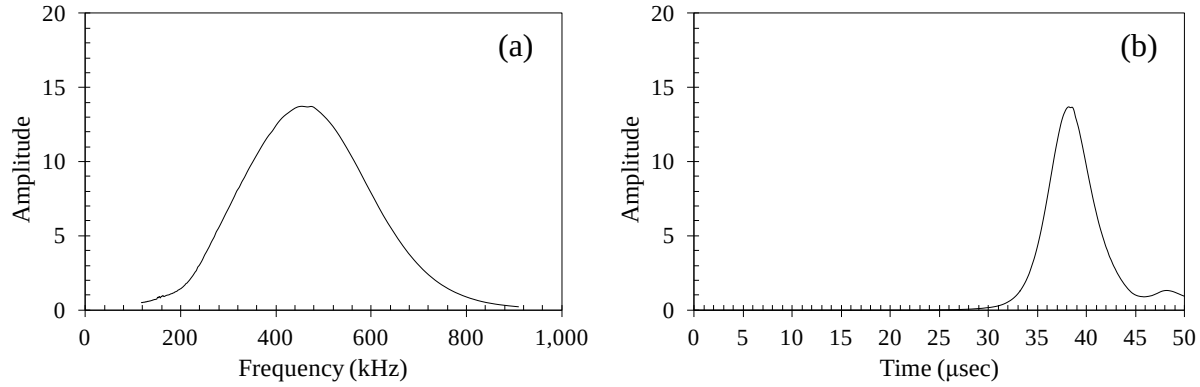

Figure 4.13. Joint time-frequency domain associated with the data from transducer T1. (a) Largest wavelet coefficients as a function of the frequency; (b) largest wavelet coefficients as a function of the time of arrival.[161]

Figure 4.13a displays the values of the largest wavelet coefficients at each scale, i.e., frequency. If the signals were not dispersive, all the coefficients would occur at the same instant. Figure 4.13b shows the maximum value of the wavelet coefficients at each time of arrival. If the signals were monochromatic, these coefficients would all occur at the same wavelet scale. From each scalogram the following three features were considered: 1) scalogram maximum value; 2) RMS of the curve associated with the largest coefficients in the frequency domain, i.e., the RMS associated with plots like the one in Figure 4.13a; 3) RMS of the curve associated with the largest coefficients in the time domain, i.e., the RMS associated with plots like the one in Figure 4.13b.

These features can be analytically expressed as:

$$F_{(i)}^{(k)} \qquad (k=1,2,3;i=1,2,3,4) \tag{4.11}$$

where k indicates the feature type and the subscript i identifies the immersion transducer. From the above features a damage index (D.I.) defined as:

$$D.I._{(i)}^{(k)} = MAX\left(\frac{F_{(i)}^{(k)}}{F_{(j)}^{(k)}}, \frac{F_{(j)}^{(k)}}{F_{(i)}^{(k)}}\right) \qquad \text{k=1,2,3; i=j=1,2,3,4 with i}\neq\text{j} \tag{4.12}$$

was computed. For each feature we therefore computed the ratios between all possible transducers' pair. Ideally, if the transducers were equally sensitive and the plate was pristine, the D.I. would be equal to 1. Otherwise, Equation (4.12) returns a value greater than 1. Figure 4.14 shows three indexes as a function of the scanning point, namely $D.I._{(2,3)}^{(1)}$, $D.I._{(3,4)}^{(2)}$, and $D.I._{(2,4)}^{(3)}$. The figures demonstrate that the sensitivity of the index in revealing the presence of an anomaly

is dependent upon the position of the defect with respect to the transducer. For example, the ratio $D.I._{(2,3)}^{(1)}$ presented in Figure 4.14a clearly shows the presence of defect 1 at points 23 and 24. Similar consideration can be drawn by observing the values of $D.I._{(3,4)}^{(2)}$ in Figure 4.14b. Instead, the index $D.I._{(2,4)}^{(3)}$ shown in Figure 4.14c has scatters in correspondence of the supports. This can be explained by looking at Figure 4.7e where the location of the transducers is illustrated. In fact, the sensitivity of a certain D.I. is affected by the relative position of the transducers with respect to the devised defects or to the supports, which were considered as defects in this study. Finally, the D.I.s were collected to form a multi-dimensional vector for the unsupervised learning algorithm based on the outlier analysis.

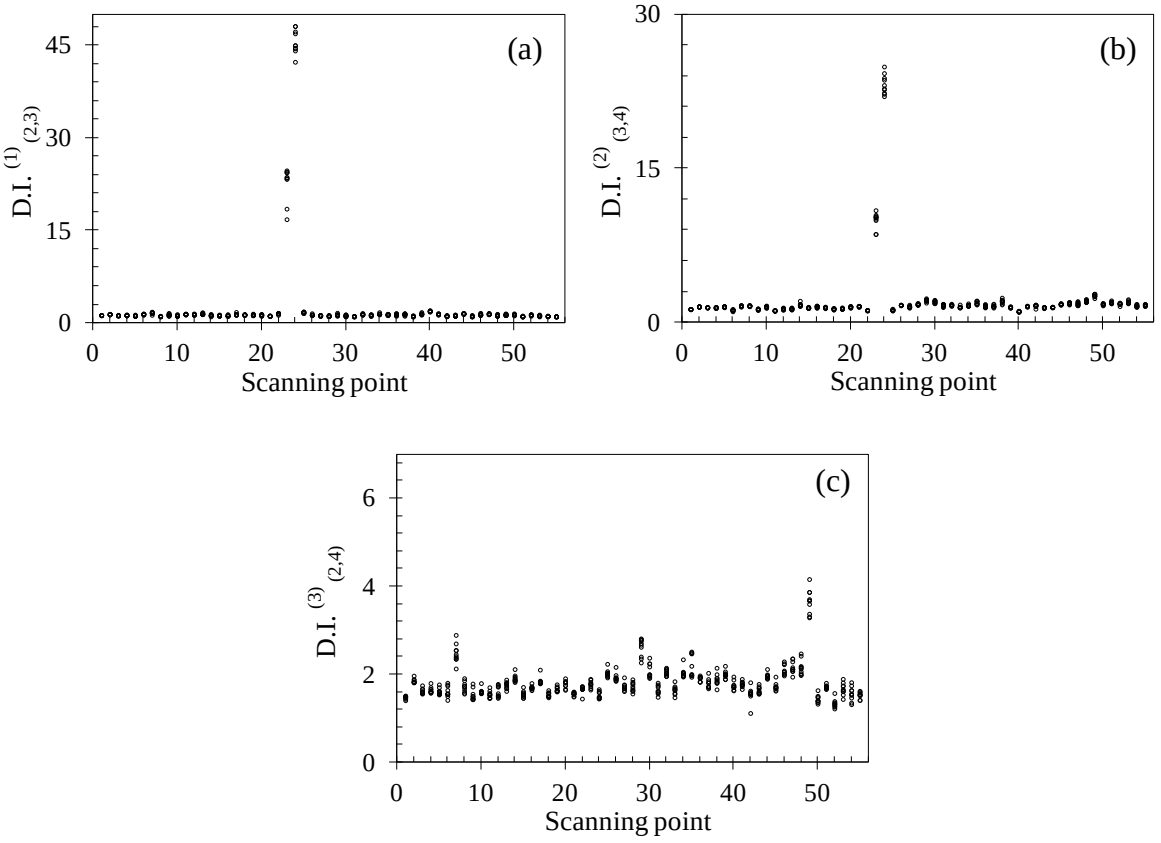

Figure 4.14. Damage index as a function of the sampling scanning points: (a) $D.I._{(2,3)}^{(1)}$, (b) $D.I._{(3,4)}^{(2)}$, (c) $D.I._{(2,4)}^{(3)}$ [161].

In the present study the baseline consisted of 500 samples (=20 scanning point x 5 measurements x 5 scans) taken at 20 scanning points that were damage-free. For each of these points, 5 out of 10 measurements were considered for all scans. Once the values of D_ζ according to Equation (4.2) of the baseline distribution were determined, the threshold value was taken as the usual value of 3σ equal to 99.73% of the Gaussian confidence limit. The normal probability plot [174] was computed to verify the Gaussian distribution of the baseline, proved by the fact that the data should be centered on the value of 1, which identifies the structure in its pristine conditions. In the circumstance that the baseline data do not comply with the normality distribution the threshold values can be still estimated [160][175][176]. For illustrative purposes, Figure 4.15 shows the normal probability plot of the baseline associated with three indexes, namely $D.I._{(2,4)}^{(1)}$, $D.I._{(2,4)}^{(2)}$, and $D.I._{(2,4)}^{(3)}$. Since all the data are clustered to the line and the same was proved for the whole baseline, we can assume that the baseline is normally distributed [177].

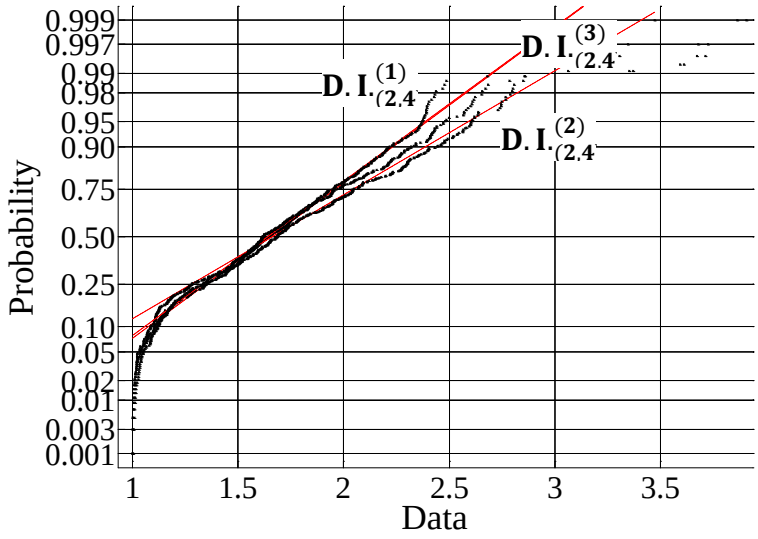

Figure 4.15. Normal probability plot for the baseline of features $D.I._{(2,4)}^{(1)}$, $D.I._{(2,4)}^{(2)}$ and $D.I._{(2,4)}^{(3)}$ [161].

4.4.2 Experimental results and discussion

We first applied the multivariate analysis using three features separately. The input vector in this case is 6-dimensional since four transducers can be paired in six different combinations. Figure 4.16 shows the Mahalanobis squared distance (MSD) as a function of the scanning points. The horizontal line represents the baseline threshold while the vertical lines identify the location of the defects (continuous lines) and of the supports (dashed lines). Feature 1 provides the highest number of proper outliers and lowest number of false positives and false negatives.

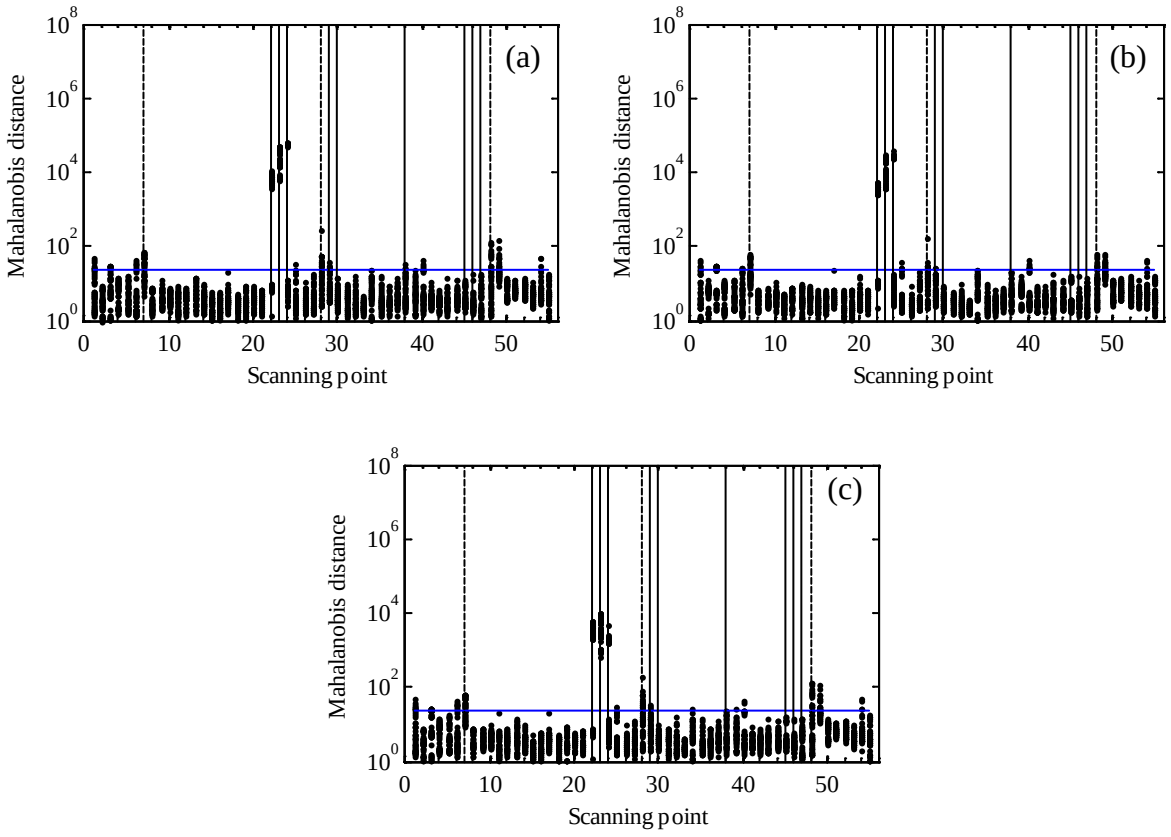

Figure 4.16. Mahalanobis squared distance for (a) feature 1 (b) feature 2 (c) feature 3. [161]

The features considered separately were then subsequently considered simultaneously with the aim of increasing the sensitivity to damage compared to the single feature's case. Thus,

four new cases were considered: three obtained by combining pairs of features in a round-robin fashion, and one combining the three features altogether. Figure 4.17 shows the Mahalanobis square distance as a function of the scanning points. The values of the corresponding thresholds are superimposed and the meaning of the vertical lines is the same as before. It should be noticed that the values of the Mahalanobis squared distance for the case of the three features altogether are some orders of magnitude larger than the corresponding values of the former multivariate analysis.

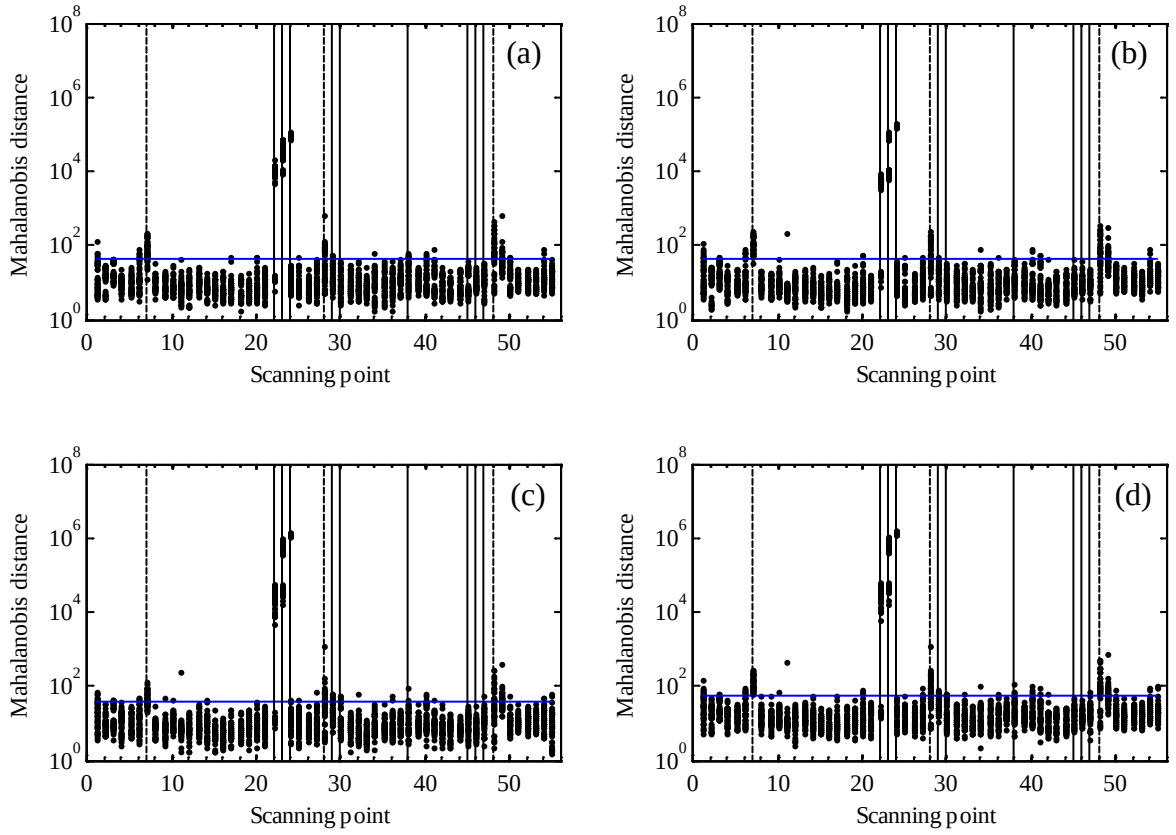

Figure 4.17. Mahalanobis squared distance for (a) features 1 and 2, (b) features 1 and 3, (c) features 2 and 3, and (d) all features. [161]

For example, the values of Mahalanobis squared distance for the case of feature 1-2-3 of Figure 4.17d are two orders of magnitude larger than the corresponding values for the case of feature 3 of Figure 4.16c. As a consequence, the sensitivity to damage is considerably improved.

Overall, the number of proper outlier increases and the number of false negative decreases when all the three features are considered (Figure 4.17d).

By looking at the plots presented in Figures 4.16 and 4.17, we can conclude that the method enable the detection of defects 1 and 2, while defects 3 and 4 were probably too small to be located. Table 1 summarizes the number of correct outliers, false positives, and false negatives. The table shows that the number and the type of feature selected affect the sensitivity of the non-contact probing system. While the single feature of the largest wavelet coefficient outperforms the other two features, the simultaneous use of all three increases by almost 50% the number of outliers detected and decreases by 20% the number of false negatives. This can be explained by looking at the nature of our inputs to the outlier analysis. In fact, we considered the ratios of three features inherent to the four transducers. The sensitivity to damage of a transducer, and consequently of a feature, is determined by the vicinity of that particular transducer to a defect. Thus, increasing the dimensionality of our matrix will lead to a better performance in terms of damage detection. Furthermore, it must be noticed that, in our analysis, we also included the supports as defects even though, in real applications, this is not really true.

Table 4.1. Proper number of outlier, false negative and false positive for multivariate analysis.

	Feature 1	***Feature 2***	***Feature 3***	***Feature 1-2***	***Feature 1-3***	***Feature 2-3***	***Feature 1-2-3***
Proper # of outlier	170	139	165	216	188	211	234
False positive	54	65	51	58	60	56	67
False negative	430	461	435	384	412	389	366

Therefore, for example, the number of false negative in Table 1 is comprehensive of also the missing outlier for the supports, thus making the real number of false negative much higher than what it would be in a real application.

4.4.3 Conclusions

In this chapter we presented an automated damage-detection technique for immersed metallic plates based on the noncontact generation and detection of guided ultrasonic waves. The waves were generated using laser pulses and detected by means of an array of immersion transducers. The main advantages of using laser pulses instead of immersion actuators for the generation of waves are the lift-off distance, the omni-directionality of the stress field on the irradiated point, and the broadband nature of the signal that can be generated. The signals were processed to extract few features in the time and joint time and frequency domain. The features were then used in a multivariate outlier analysis to detect structural damage artificially devised on the test object. We also include a finite element model to simulate the laser-based ultrasonic generation in an immersed plate and to portray the propagation of the guided waves as well as to map the pressure field in the liquid. This is important as the contactless method presented here enables, in principle, the detection of the Lamb waves leaking into the fluid, as well as the bulk waves propagating in the fluid only and the quasi-Scholte wave propagating at the solid-liquid interface.

In the experiments, the probing system was controlled by a hardware system designed and built in house that allowed for the automated inspection of immersed structures. Prior to examine the success of the noncontact system for health monitoring applications, its repeatability was tested by comparing the time waveforms detected at the same point and by inspecting the test object many times.

We found the noncontact system is repeatable and the signal processing algorithm adopted in this study was able to capture an artificial notch clearly, and was partially able to detect a through-thickness hole that was as small as few millimeters. A dent and a simulated corrosion (plate thinning) were not detected probably due to their small size.

4.5 TEST II –EXPERIMENTAL SETUP

In this experiment a very similar setup as the one illustrated in Chapter 4.3 was adopted. Here, five immersion transducers (Olympus NDT, V303-SU, Part ID: U8423005) were arranged according to the scheme presented in Figure 4.18. Please note that in Figure 4.18a-c there are seven transducers, since the original setup counted two additional receivers. In this dissertation, we report the results associated with the use of the five transducers T1-T5 shown in Figure 4.18e.

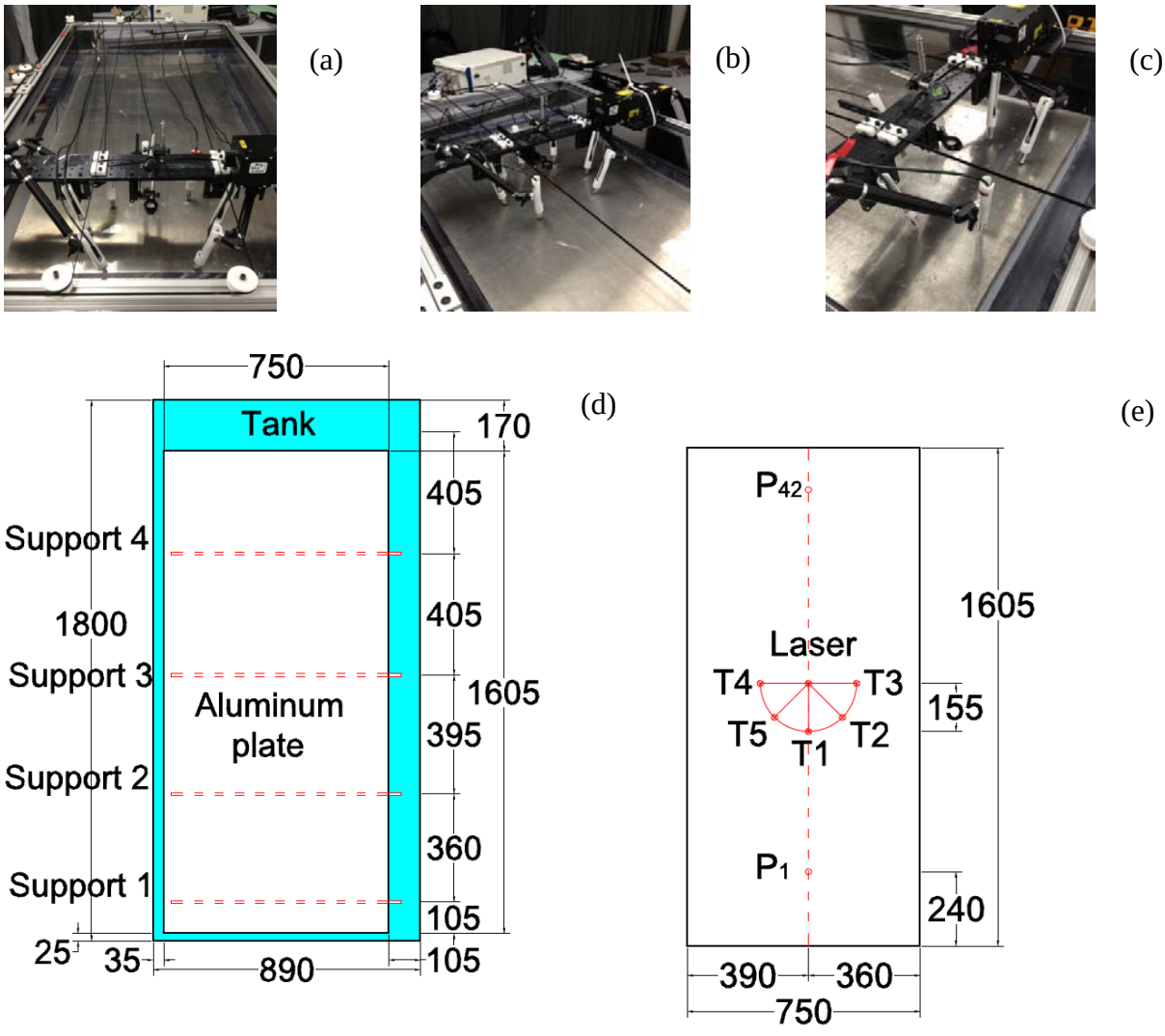

Figure 4.18. Experimental setup. (a,b,c) Photos of the scanning system and close up-view of the ultrasonic transducers, laser and optical system. (d,e) Schematics of the setup: (d) plan view, (e) details of the position of the transducers (T1-T5) and of the irradiated points. The drawings are on scale and all the quotes are in millimeters.

The foam panel was no longer present since we verified that the quality of the leaky Lamb waves did not improve significantly with its use. The plate was positioned on four supports (Figure 4.18d) and the level of water above was 65 mm.

Figure 4.18d details the location of the supports while the location of the transducers as well as their distance from the central laser-illuminated point is shown in Figures 4.18e. The same B-scan system used in Chapter 4.3 was used to perform the tests. Five defects displayed in Figure 4.19a were machined at the locations shown in Figure 4.19b. Defects 1 to 4 are the same described in Chapter 4.3, while defect 5 was a horizontal whole-through cut.

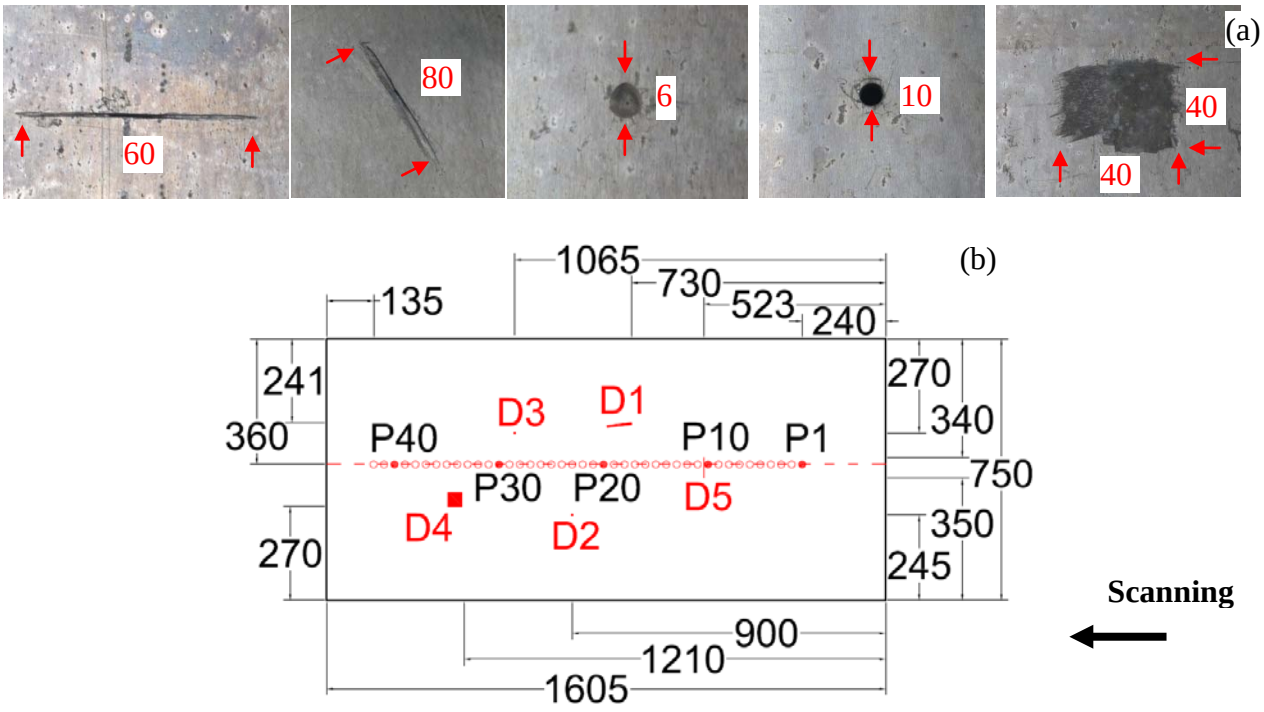

Figure 4.19. (a) Photos of the artificial defects (D1, D2, D3, D4, D5) devised on the plate. (b) Location of the defects and of few laser-illuminated points. The drawing is on scale and all the quotes are in millimeters.

In test 2 the B-scan was conducted by irradiating 42 points of the plate spaced 30 mm apart and aligned 360 mm from the right edge of the plate. Ten laser pulses were generated at each point. The plate was inspected five times to prove the repeatability of the methodology. Figure

4.19b also shows the location of the first and last scanning point as well as few other key points located close to the artificial defects. The repeatability of the method was already proved in Chapter 4.3.1.

4.5.1 SHM algorithm

Figure 4.20 shows a typical time waveforms recorded at point n. 27 in a defect-free location. Three main wave packets are visible: the first packet at about 40 μsec is the leaky S_0 mode, the second packet comprised between 50 μsec and 60 μsec is likely generated by the interaction of the leaky S_0 mode with the liquid-air interfaces, while the third wave packet beyond 80 μsec is the superposition of the quasi-Scholte mode and the bulk wave. In this study, we analyzed the leaky S_0 mode. As such, any signal processing discussed hereafter was conducted on the time window 0-50 μsec. As it is shown in Figure 4.20, the amplitudes of the signals are lower compared to Figure 4.9 since, in this test, we didn't use any preamplifiers in contrast with what we did In Chapter 4.3 .

Figure 4.21 shows the corresponding GWT scalograms of the time waveforms presented in Figure 4.20 at the time interval 0 – 50 μsec. The scalograms show that the energy of the leaky S_0 mode is dominant in the 200-800 kHz range, with peak located between 500 and 600 kHz.

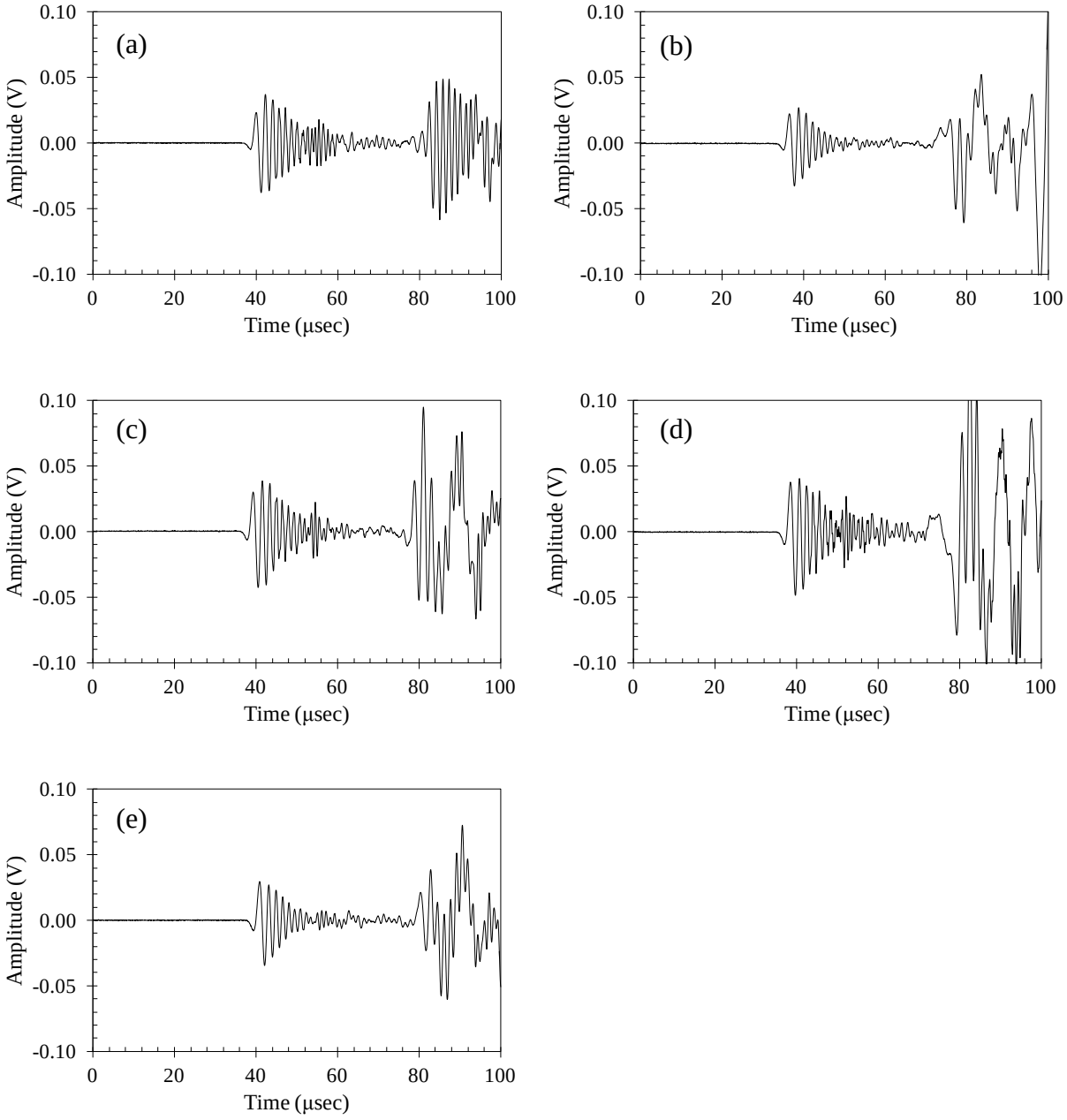

Figure 4.20. Experimental time waveforms by (a) T1, (b) T2, (c) T3,(d) T4, (e) T5.

From each scalogram, as the one displayed in Figure 4.21, we computed two subplots of the kind shown in Figure 4.22. In particular, Figure 4.22a displays the values of the largest wavelet coefficients at each frequency while Figure 4.22b displays the values of the largest wavelet coefficients at each time.

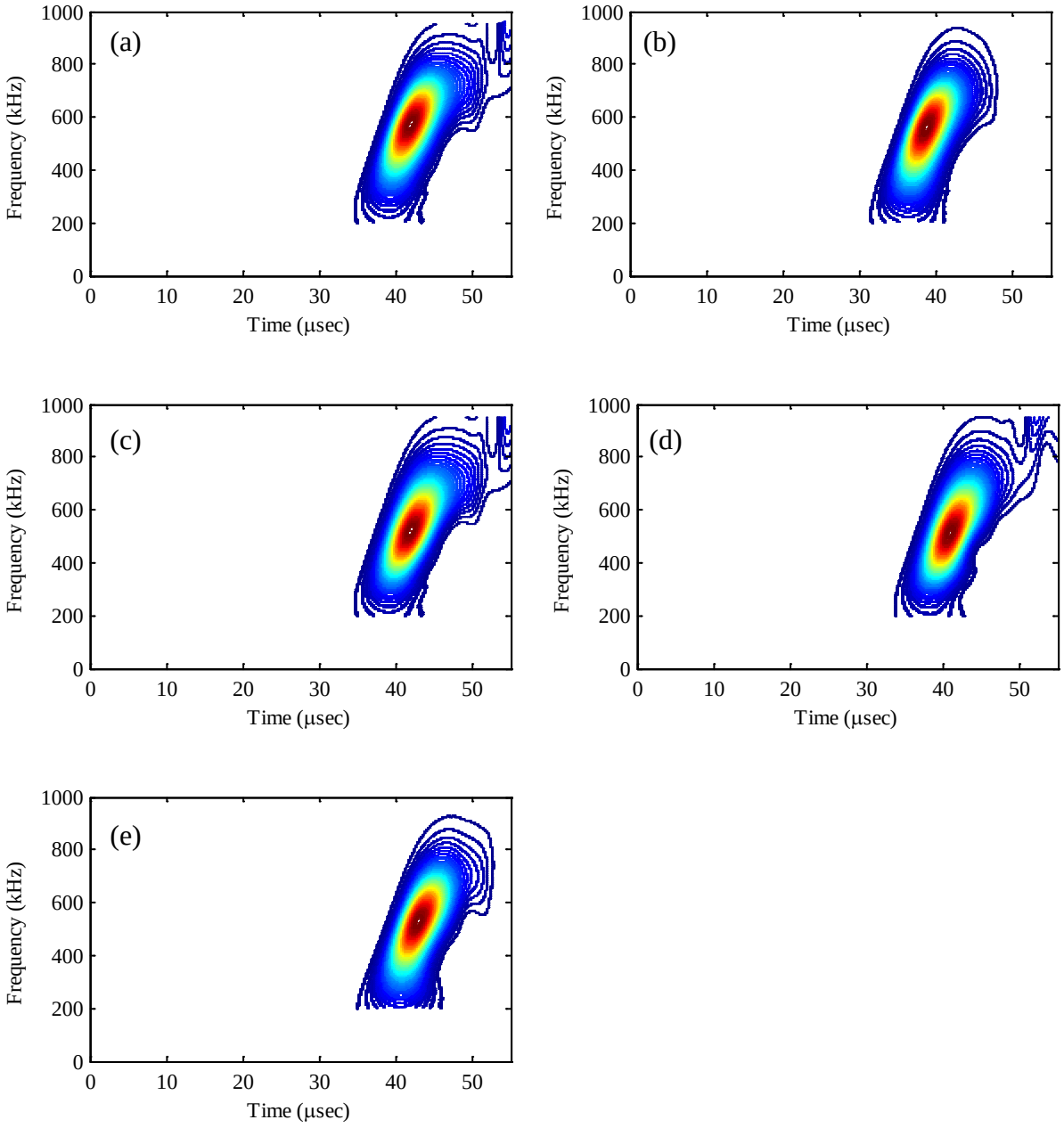

Figure 4.21. GWT scalograms associated with the time waveforms presented in Figure 4.20.

Figure 4.23 shows the Fast Fourier Transform (FFT) of the time waveforms presented in Figure 4.20 in the frequency range 0–4 MHz. As expected from Figure 4.21, the FFTs show a main peak located between 500-600 kHz.

From the graphs like the ones shown in Figures 4.20-4.23, we extracted eight features from the time, time-frequency and frequency domain. From the time domain plots, we retained the peak-to-peak amplitude and the root mean square (RMS). From the time-frequency plots we retained the scalogram maximum values, the RMS of the curve associated with the largest coefficients in the frequency domain, and the RMS of the curve associated with the largest coefficients in the time domain. Finally, from the frequency plots, we retained the FFT maximum value, the RMS of the bandwidth comprised between 250 and 650 kHz, and the full width half maximum (FWHM) of the same FFT frequency bandwidth.

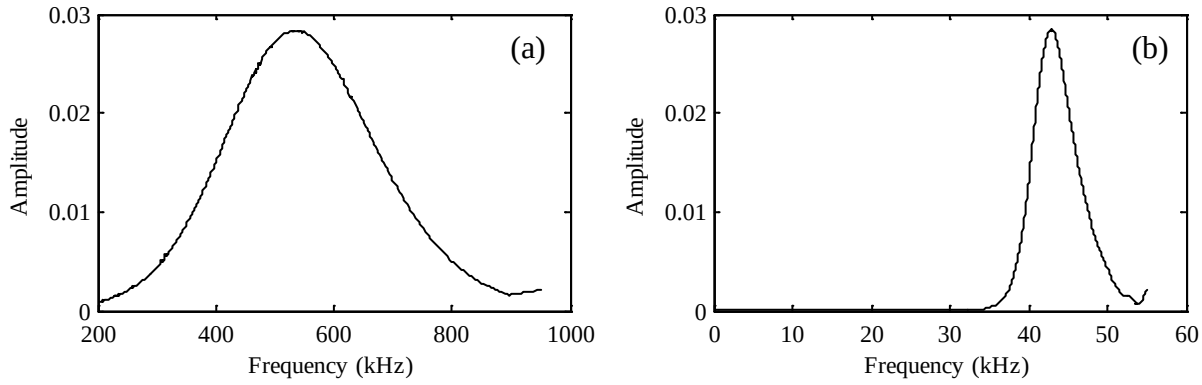

Figure 4.22. Joint time–frequency domain associated with the data from transducer T1: (a) largest wavelet coefficients as a function of the frequency and (b) largest wavelet coefficients as a function of the time of arrival.

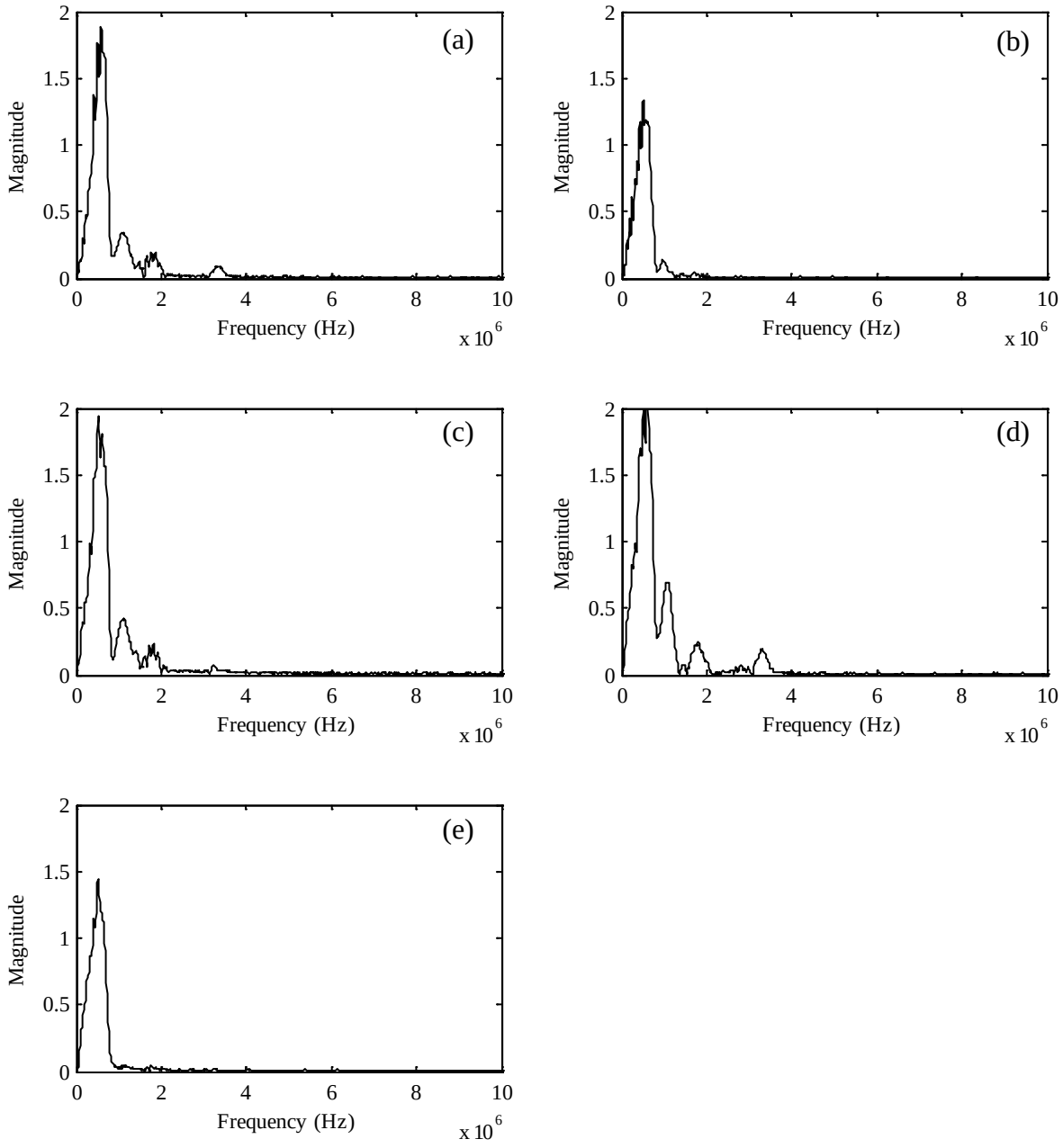

Figure 4.23. FFTs associated with the time waveforms presented in Figure 4.20.

Table 4.2 details all the features above described in the order used in our SHM algorithm. All the features can be analytically expressed as:

$$F_{(i)}^{(k)} \qquad (k=1\div 8; i=1,2,3,4,5) \tag{4.13}$$

where k indicates the feature type and the subscript i identifies the immersion transducer. From the above features a damage index (D.I.) defined as:

$$D.I._{(i)}^{(k)} = MAX\left(\frac{F_{(i)}^{(k)}}{F_{(j)}^{(k)}}, \frac{F_{(j)}^{(k)}}{F_{(i)}^{(k)}}\right) \qquad k=1\div 8;\ i=j=1,2,3,4,5 \text{ with } i\neq j \tag{4.14}$$

was computed. For each feature we therefore computed the ratios between all possible transducers' pair. Ideally, if the transducers were equally sensitive and the plate was pristine, the D.I. would be equal to 1. Otherwise, Equation (4.14) returns a value greater than 1.

Table 4.2. Feature classification and type.

Feature	Description
1	Scalogram maximum value
2	FFT maximum value
3	RMS of the FFT for the bandwidth comprised between 250 and 650 kHz
4	RMS of the curve associated with the largest coefficients in the frequency domain
5	RMS of the curve associated with the largest coefficients in the time domain
6	Peak-to-peak value of the time window between 0-50 μsec
7	RMS value of the time window between 0-50 μsec
8	FWHM of the FFT for the bandwidth comprised between 250 and 650 kHz

Figure 4.24 shows two indexes as a function of the scanning point, namely $D.I._{(1,5)}^{(4)}$, $D.I._{(2,3)}^{(5)}$. The figures demonstrate that the index may reveal the presence of an anomaly, based upon the position of the bench plate with respect to the defect.

For example, the ratio $D.I._{(1,5)}^{(4)}$ presented in Figure 4.24a clearly shows the presence of the horizontal cut at the scanning points between 11 and 15. This is consistent with the fact that the area comprised by the array covers this defect. On the other hand, the ratio $D.I._{(2,3)}^{(5)}$ was effective at detecting the vertical cut at the scanning points between 19 and 23. This is again consistent with the fact that transducers 2 and 3 perfectly cover the area occupied by this defect.

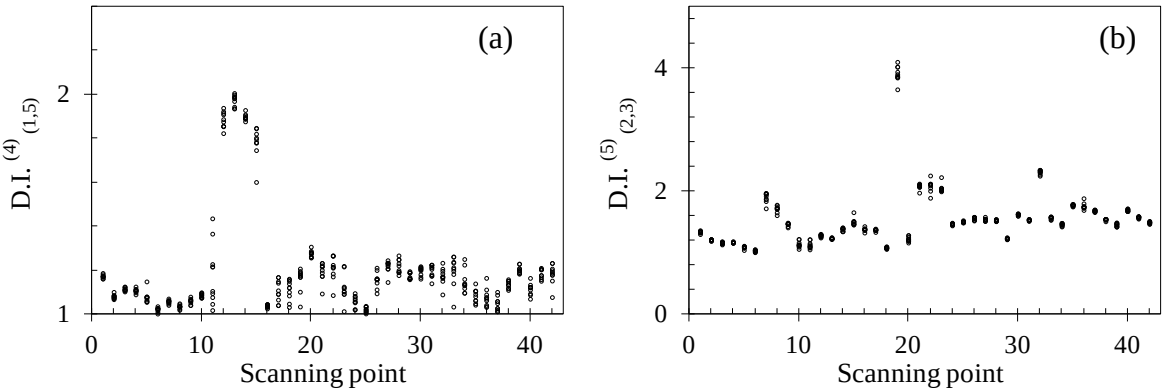

Figure 4.24. Damage index as a function of the sampling: (a) $D.I._{(1,5)}^{(4)}$, (b) $D.I._{(2,3)}^{(5)}$.

4.5.2 Experimental results and discussion. Part I

On the basis of the outcomes detailed in Chapter 4.4.2, we fist conducted a multivariate analysis considering all the eight features together, thus considering an input vector of 80 ratios since this should theoretically lead to the highest success of the method.

In this case the baseline consisted of 700 samples (=14 scanning point x 10 measurements x 5 scans) taken at 14 scanning points that were damage-free. For each of these points, all the 10 measurements were considered for all scans. Once the values of D_ζ according to Equation (4.10) of the baseline distribution were determined, the threshold value was taken as the usual value of 3σ equal to 99.73% of the Gaussian confidence limit. Figure 4.25 shows the Mahalanobis squared distance as a function of the scanning points. The horizontal line represents the baseline threshold.

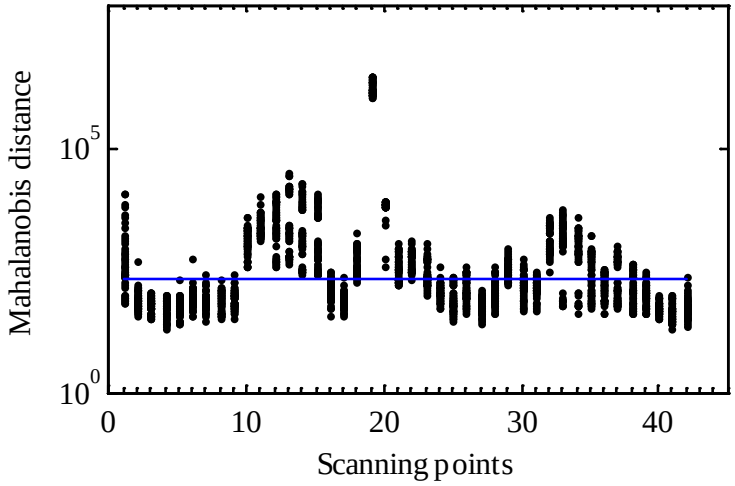

Figure 4.25. Mahalanobis squared distance for all eight features.

We considered as defects all those points that are falling into the area covered by the half-moon configuration, as shown in Figure 4.18e. From this analysis, we concluded that 24 points have to be considered as outlier locations, i.e., defects. As shown inn Figure 4.25, our outlier analysis was capable of distinguishing pretty clearly the presence of the horizontal cut (points 10 to 15), the vertical cut (points 19-23) and partially the corrosion (32-35). This confirms that the sensitivity of the methodology is also dependent upon the vicinity between the defects and the transducers, as argued in Chapter 4.4.2. With respect to the results presented in Chapter 4.4.2, an

improvement was observed. In fact, both the horizontal cut (not present before) and the corrosion were detected with some level of precision. Therefore, both the new spatial distribution of the transducers and the increased number of feature positively affected our results.

4.5.3 Selection of the training data

Following the outcomes of the analysis outlined in Chapter 4.5.2, we considered the dataset associated with pristine structure from the first scan as baseline and we tested the other scans in search for outliers. Therefore, once a scan is selected for training, the whole multivariate analysis can be conducted using only the baseline data taken from it, in contrast with what was done before. This approach is suitable for field test where, for instance, only a portion of collected data can be used as a baseline. This could be particularly useful when structures can be considered pristine only in some areas, which can be consequently used as baseline for the analysis of the whole target. Therefore, no prior knowledge of the entire structure is required for the application of this technique.

Following a procedure similar to the one adopted in Chapter 4.4.1, the D.I.s calculated according to Equation (4.12) were collected to form a multi-dimensional vector for the unsupervised learning algorithm based on the outlier analysis. We then calculated the MSD according to Equation (4.10). In this case, the baseline consisted of 140 samples (=14 scanning point x 10 measurements x scan 1) taken from scan in *a priori* known defect-free location. Once the values of D_{ζ} of the baseline distribution were determined, the threshold value was taken as the usual value of 3σ equal to 99.73% of the Gaussian confidence limit.

We first performed this analysis using the baseline taken from scan 1 and then we performed the same analysis using the baseline taken from scan 3 to see if any improvement was

achieved by the selection of a scan. Figure 4.26a shows the MSD as a function of the scanning points for all the five scans when the baseline is taken from scan 1, while Figure 4.26b shows the Mahalanobis square distance as a function of the scanning points for all the five scans when the baseline is taken from scan 3.

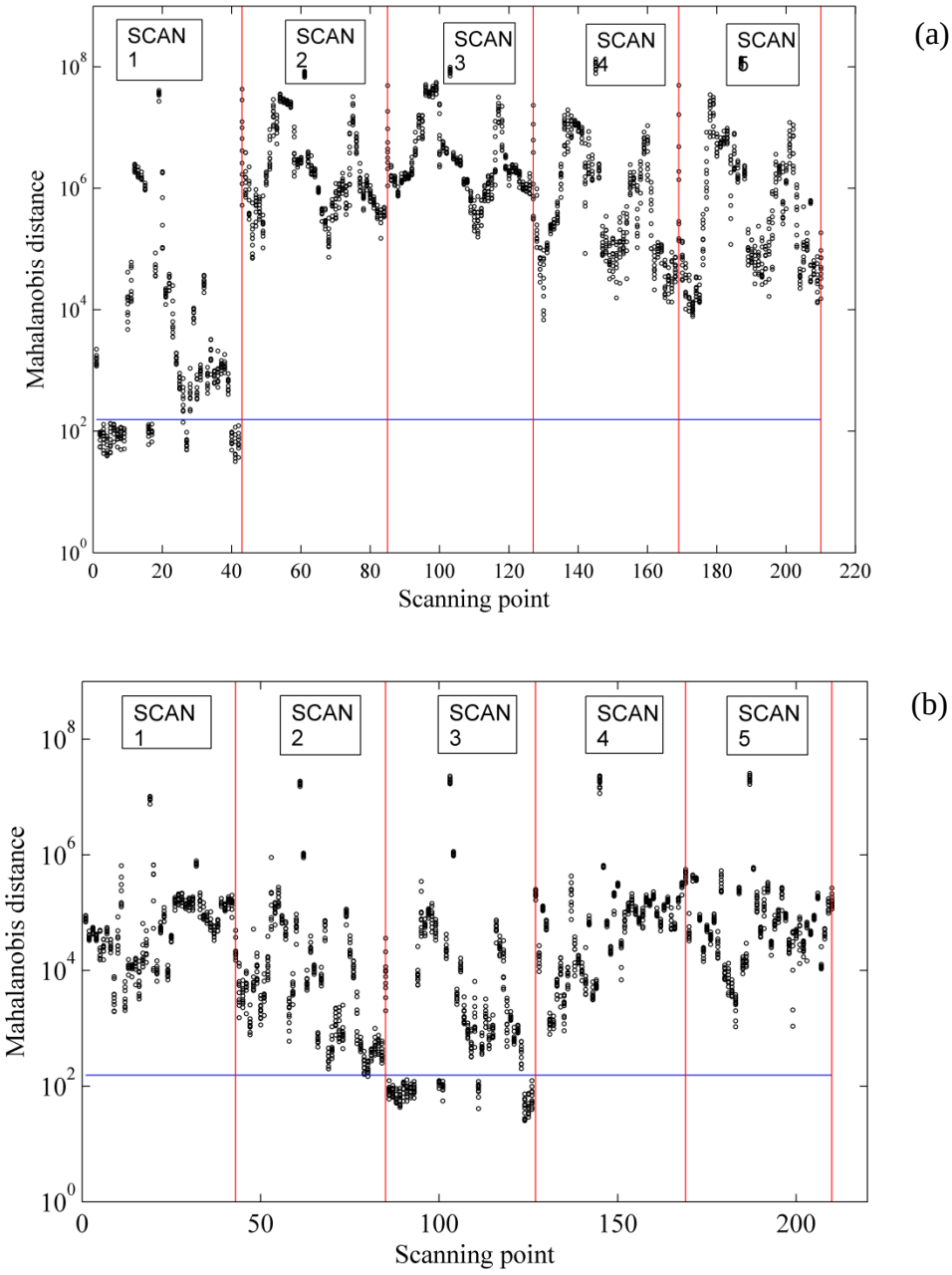

Figure 4.26. Mahanobis square distance as a function of the scanning points. (a) Baseline taken from scan 1, (b) baseline taken from scan 3.

In both cases, the horizontal line represents the baseline threshold while the vertical lines identify the successive scans. As can be seen, the results are comparable in both cases, thus confirming that the repeatability of the method is good. Even though the higher Mahalanobis square distance in Figure 4.26a would suggest a higher sensitivity of the method, the fact that both cases are comparable in terms of number of proper outliers suggests that either one could be taken as baseline. Therefore, we chose the baseline from scan 1 as reference from the analysis conducted from now on since that could correspond, in the real monitoring of a long structure, to the first length of the target.

4.5.4 Experimental results and discussion. Part II

Once we selected the baseline from scan 1, as outlined in Chapter 4.5.3, we performed the outlier analysis following an optimization approach. We first applied the multivariate analysis using the eight features separately. In this case, the input vector is 10-dimensional since 5 transducers produce 10 different combinations. Then, we paired the features into all the possible subsets following the procedure outlined in Chapter 4.4.2 until considering all the features together. Figure 4.27 shows the MSD as a function of the scanning points for three cases. The horizontal line represents the baseline threshold while the vertical solid line bound two consecutive scans. In particular, Figure 4.27a shows the analysis associated with feature 2 only, Figure 4.27b shows the MSD vs. scanning point for features 1, 2, 5, 8 combined, and Figure 4.27c shows the MSD vs. scanning point for all features together.

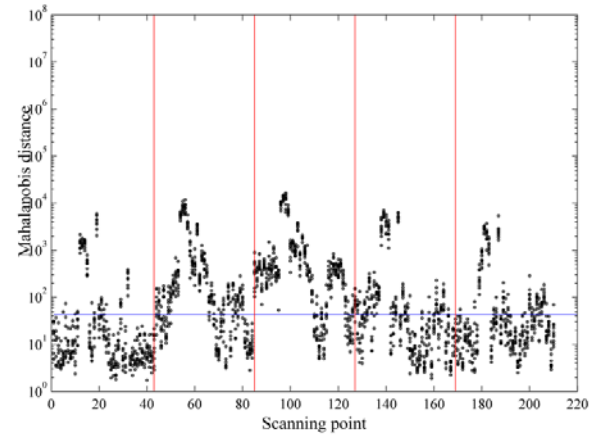

(a)

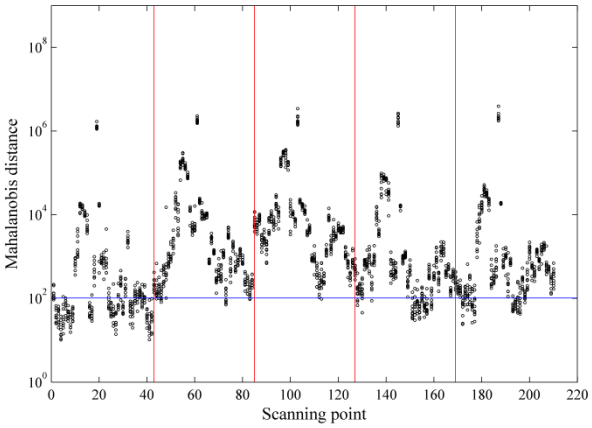

(c)

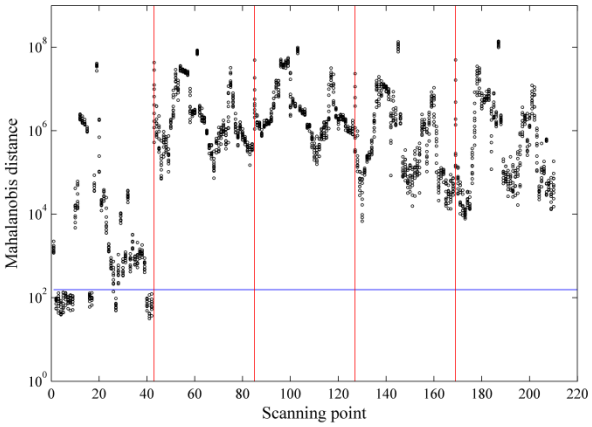

(b)

Figure 4.27. Mahalanobis square distance relative to: (a) feature 2, (b) features 1,2,5,8, and (c) all features.

The cases of single features provided the highest number of proper outliers and lowest numbers of false positives and false negatives. In the analysis of more features paired together, no significant improvements are achieved if considering additional features, such as, for instance, two vs. eight. On the other hand, as we use more features simultaneously, the values of the MSD progressively become of some orders of magnitude larger. For example, the values of the MSD for the case of feature 2 of Figure 4.27a are four orders of magnitude smaller than the corresponding values for the case of all the features. However, this is only a partially true increase of sensitivity. In fact, the total number of outlier increases but it is almost lost the sensitivity to specific defects. In other words, the algorithm categorizes most of the points as outlier, thus also detecting the true defects, but not clearly discriminating them.

As such, we investigated the true success rate of the methodology on the basis of the following approach. If we define the success rate as the sum of proper outliers and proper inliers over the total number of data in percentage, we can say that the highest success rate was achieved when using the features separately. In particular, feature 2 gave the highest success rate equal to 65.95%. When combining the features into pair of four, the success rate drops to slightly above 50% which is perfectly comparable with the success rate of the case of eight features together (52.38%). We also calculated the false positive percentage as the number of false positives over the total number of data and the false negative percentage as the number of false negative over the total number of data. Table 4.3 and 4.4 summarize the percentage for the success rate, the false positive and false negative when using one feature and four features, respectively. All the results presented in Table 4.3 and 4.4 are relative to scan 2 to scan 5.

Table 4.3. Results of the multivariate damage classification for all combinations with one feature.

Combination	Success rate (%)	False positive (%)	False negative (%)	Total (%)
1	65.24	31.37	3.39	100.00
2	65.95	19.05	15.00	100.00
3	53.39	41.37	5.24	100.00
4	58.81	35.95	5.24	100.00
5	65.12	32.50	2.38	100.00
6	51.96	44.52	3.51	100.00
7	59.11	38.39	2.50	100.00
8	46.96	2.92	50.12	100.00

Table 4.4. Results of the multivariate damage classification for all combinations with four features.

Combination	Success rate (%)	False positive (%)	False negative (%)	Total (%)
1 2 3 4	52.38	47.62	0.00	100.00
1 2 3 5	52.38	47.62	0.00	100.00
1 2 3 6	52.38	47.62	0.00	100.00
1 2 3 7	52.38	47.62	0.00	100.00
1 2 3 8	52.38	47.62	0.00	100.00
1 2 4 5	52.98	45.89	1.13	100.00
1 2 4 6	52.62	47.38	0.00	100.00
1 2 4 7	52.80	46.67	0.54	100.00
1 2 4 8	55.36	43.27	1.37	100.00
1 2 5 6	52.62	47.38	0.00	100.00
1 2 5 7	54.70	44.64	0.65	100.00
1 2 5 8	58.27	40.30	1.43	100.00
1 2 6 7	52.50	47.50	0.00	100.00
1 2 6 8	52.86	47.14	0.00	100.00
1 2 7 8	56.01	43.33	0.65	100.00
1 3 4 5	52.38	47.62	0.00	100.00
1 3 4 6	52.38	47.62	0.00	100.00
1 3 4 7	52.38	47.62	0.00	100.00
1 3 4 8	52.38	47.62	0.00	100.00
1 3 5 6	52.38	47.62	0.00	100.00
1 3 5 7	52.38	47.62	0.00	100.00
1 3 5 8	52.38	47.62	0.00	100.00
1 3 6 7	52.38	47.62	0.00	100.00
1 3 6 8	52.38	47.62	0.00	100.00
1 3 7 8	52.38	47.62	0.00	100.00
1 4 5 6	52.50	47.50	0.00	100.00
1 4 5 7	52.38	47.56	0.06	100.00
1 4 5 8	53.39	45.65	0.95	100.00

"Table 4.4 (continued)."

1	4	6	7	52.38	47.62	0.00	100.00
1	4	6	8	52.80	47.20	0.00	100.00
1	4	7	8	53.45	46.07	0.48	100.00
1	5	6	7	52.44	47.56	0.00	100.00
1	5	6	8	52.74	47.26	0.00	100.00
1	5	7	8	55.65	43.75	0.60	100.00
1	6	7	8	52.50	47.50	0.00	100.00
2	3	4	5	52.38	47.62	0.00	100.00
2	3	4	6	52.38	47.62	0.00	100.00
2	3	4	7	52.38	47.62	0.00	100.00
2	3	4	8	52.38	47.62	0.00	100.00
2	3	5	6	52.38	47.62	0.00	100.00
2	3	5	7	52.38	47.62	0.00	100.00
2	3	5	8	52.38	47.62	0.00	100.00
2	3	6	7	52.38	47.62	0.00	100.00
2	3	6	8	52.38	47.62	0.00	100.00
2	3	7	8	52.38	47.62	0.00	100.00
2	4	5	6	52.56	47.44	0.00	100.00
2	4	5	7	53.10	46.49	0.42	100.00
2	4	5	8	54.52	44.11	1.37	100.00
2	4	6	7	52.50	47.50	0.00	100.00
2	4	6	8	52.86	47.14	0.00	100.00
2	4	7	8	55.54	43.75	0.71	100.00
2	5	6	7	52.50	47.50	0.00	100.00
2	5	6	8	52.74	47.20	0.06	100.00
2	5	7	8	55.89	43.33	0.77	100.00
2	6	7	8	52.62	47.26	0.12	100.00
3	4	5	6	52.38	47.62	0.00	100.00
3	4	5	7	52.38	47.62	0.00	100.00
3	4	5	8	52.38	47.62	0.00	100.00
3	4	6	7	52.38	47.62	0.00	100.00
3	4	6	8	52.38	47.62	0.00	100.00
3	4	7	8	52.38	47.62	0.00	100.00
3	5	6	7	52.38	47.62	0.00	100.00
3	5	6	8	52.38	47.62	0.00	100.00
3	5	7	8	52.38	47.62	0.00	100.00
3	6	7	8	52.38	47.62	0.00	100.00
4	5	6	7	52.44	47.56	0.00	100.00
4	5	6	8	52.74	47.26	0.00	100.00
4	5	7	8	53.57	46.13	0.30	100.00
4	6	7	8	52.50	47.50	0.00	100.00

"Table 4.4 (continued)"

5	6	7	8	52.56	47.44	0.00	100.00

Figure 4.28 shows the success rate for all the five scans when using the data from scan 1 as baseline and all features together. It is possible to note that the algorithm performs well when considering the first scan, i.e., the same as the one from which we extrapolated the baseline, but it is not very effective when analyzing the successive scans. In fact, the success rate drops from more than 85% to 53%. Therefore, the algorithm is successful if the data used as baseline are included in the overall set of testing data. However, it is not effective when the baseline is not included in the dataset used for general testing.

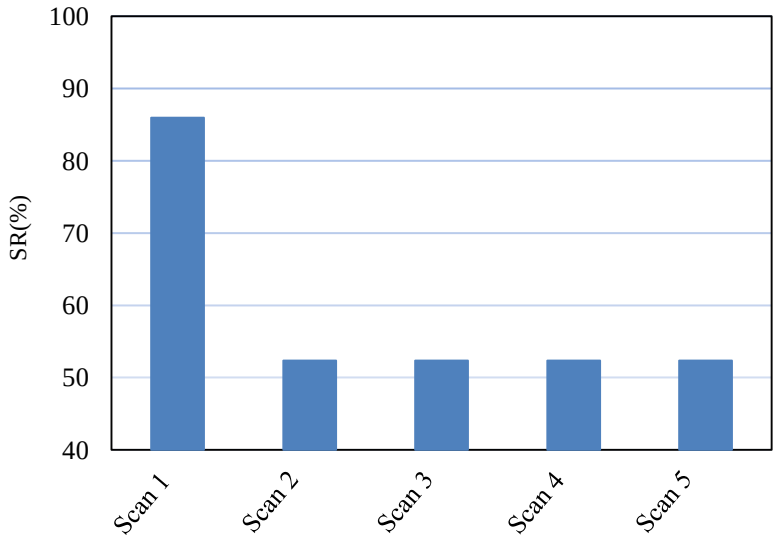

Figure 4.28. Success rate of the multivariate analysis associated with five scans by considering eight features.

Several hypotheses can be argued to justify the results. For instance, the choice of the features could be not optimal. To verify this, we compared the values of the single features $F_{(i)}^{(k)}$ for all the eight features to see if any were faulty. According to the analysis synthesized in Table

4.3, feature 1 should be the most and feature 8 the least successful. This was proven by our analysis. Figure 4.29 shows the amplitude of two features, namely feature 1 (Figure 4.29a) and feature 8 (Figure 4.29b) vs. scanning points for all the five scans.

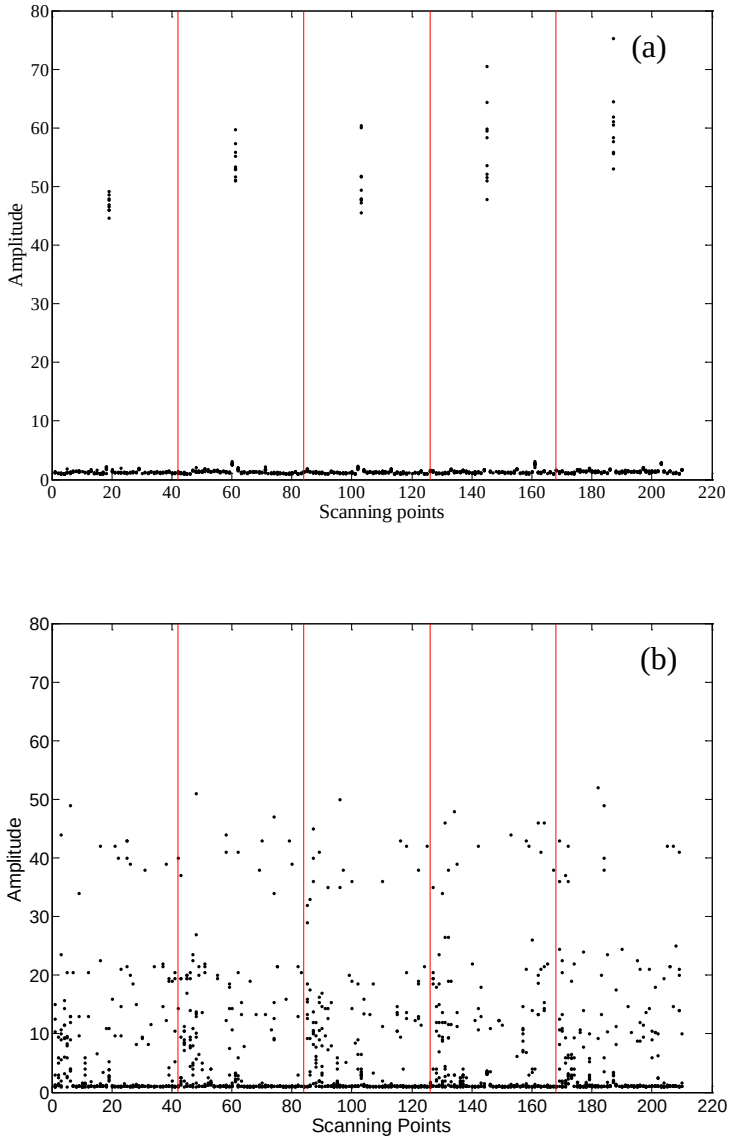

Figure 4.29. Amplitude of (a) feature 1 and (b) feature 8 vs. scanning points.

As can be seen, the repeatability of feature 8 is much lower than the one relative to feature 1, as proved by diffuse scattering of the data. This implies that some features could not

have performed very well, and thus other features could be used for this analysis in the future. In this specific case, the FWHM (feature 8) could be less stable since it required selecting a narrow frequency bandwidth for all the data (250-650 kHz). However, even small shifts in the frequency spectrum could have affected the result. On the other hand, the maximum of the CWT (feature 1) is the most complete since it retains both time and frequency content and it is the less prone to error, granted that the CWT has been chosen appropriately.

Another possible reason for the low success rate of the method could be related to the fact that the signal processing adopted was not aggressive enough for the specific application. A good solution could be to try to compare this multivariate analysis with other methods, such as the artificial neural network. Furthermore, the method itself could be not enough repeatable to be successful in the case where the baseline is not included in the testing data. In other words, the technique is capable of properly classifying defects when the inclusion in the baseline of defect-free points taken from all the data set is available, but it is not yet capable of discriminating proper outliers if no *a priori* knowledge of the data is available. Therefore, it is possible to conclude that this analysis is somehow promising even though further analysis is suggested.

4.5.5 Conclusions

In this chapter we presented an automated damage-detection technique for immersed metallic plates based on the noncontact generation and detection of guided ultrasonic waves. The waves were generated using laser pulses and detected by means of an array of immersion transducers. The signals were processed to extract eight features in the time and joint time and frequency domain. The features were then used in a multivariate outlier analysis to detect five structural damages artificially devised on the test object. In the experiments, the probing system was

controlled by a hardware system designed and built in house that allowed for the automated inspection of immersed structures.

We found the noncontact system is capable of detecting the defects when the baseline is included in the testing data. In fact, we could successfully discriminate the horizontal cut, the vertical cut and the corrosion. However, the success rate of the method is still not optimal when the training data are not inclusive to the testing data.

5.0 INVESTIGATION OF ALUMINUM PLATES OF VARYING THICKNESS

In this chapter we present the research conducted to investigate the effect of plate thickness on the energy concentration of the ultrasonic signals. The objective is to understand why an energy peak around 500 kHz was observed in the previous experiments.

The first section of this chapter will introduce the theoretical basis of Lamb wave propagation and energy concentration in waveguides. The second section will discuss the experimental results conducted during a series of experiments using six different plate thicknesses.

5.1 VARIOUS ASPECTS OF ENERGY CONCENTRATION

An interesting aspect of laser propagation on immersed structures involves the understanding of energy concentration in the waveguides. In fact, despite the ultrasonic transducers selection, a guide on peak energy concentration can be of great aid in proper analysis of the results. If time-frequency analysis is involved, for instance, this understanding will help in choosing an effective scale selection and, therefore, a good resolution. Furthermore, appropriate distance between transmitter and receiver could also be inferred.

Laser generation is broadband and the way to control mode generation is by keeping the Lamb wave frequency-thickness product low. However, there are cases where thicker plates are studied and, increasing the frequency-thickness product, multiple modes are excited. A better

understanding of the influence of varying thickness plate on the peak energy values in the time-frequency domain is needed.

In 1991 Bushell et al. studied the effect of the thickness on the laser-generated waves in plates [178]. They used an Nd:YAG laser on a series of dry aluminum plates with thickness in the range from 28 μm to 63 mm using 1.064 μm wavelength and a laser pulse-time of 10 ns. They measured the nodal and in-plane motion by electromagnetic acoustic transducers and, for comparison, the normal displacement by a laser interferometer. Referring to the fact that the propagation of ultrasonic waves in plates follows the Rayleigh-Lamb equation, they distinguished three zones. The first zone is dominated by the presence of surface Rayleigh waves and bulks waves that have very distinct time of arrival and shapes. In this case the thickness of the plate is higher than all the wavelengths contained in the pulse and, in their case, represented plates with thickness greater than 6 mm. The appearance of the Rayleigh waves is independent from the thickness. The second zone is dominated by the presence of the zero-order Lamb waves. In this case the thickness of the plate is smaller than all the wavelengths contained in the pulse and, in their case, represented plates with thickness smaller than 0.5 mm. The shape of the waveforms could vary dramatically even with small changes in thickness. The third region is the intermediate one, where the waveforms are extremely complex and it may become very hard to discriminate their true nature. The Rayleigh waves progressively disappear with the decrease of the thickness with respect to the Lamb wave modes [178].

Various methods have also been developed in literature to calculate the thickness or the thickness velocities of thin plates by means of laser techniques [179-181]. To the best author's knowledge, no studies have been conducted on the influence of plate thickness on the laser-generated leaky Lamb waves in immersed waveguides.

5.2 METHODOLOGY

We adopted a technique outlined elsewhere [157]to extract the group velocities of the ultrasonic signals. In particular we extracted our group velocities using a joint-time frequency analysis based on the CWT. Therefore, by using the GWT transform, we produced scalogram contour plots that show the time-frequency content in term of energy of our ultrasonic signals captured at two separated locations (x_1 and x_2) located in the same direction of the leaky Lamb wave. We then retained the time of arrival (t_1 and t_2) of the GWT scalogram peaks at all the frequencies and we calculated the group velocity Cg as a function of frequency f(i) according to the following equation [*Sale*]:

$$C_g(f) = \frac{x_2 - x_1}{t_2(f) - t_1(f)} \tag{5.1}$$

Once we obtained the experimental values, we compared them with the theoretical results calculated for a dry aluminum plate using the SAFE method. Figure 5.1 shows the theoretical dispersion curves for phase (Figure 5.1a) and group velocity (Figure 5.1b) for a dry aluminum plate that we used as reference.

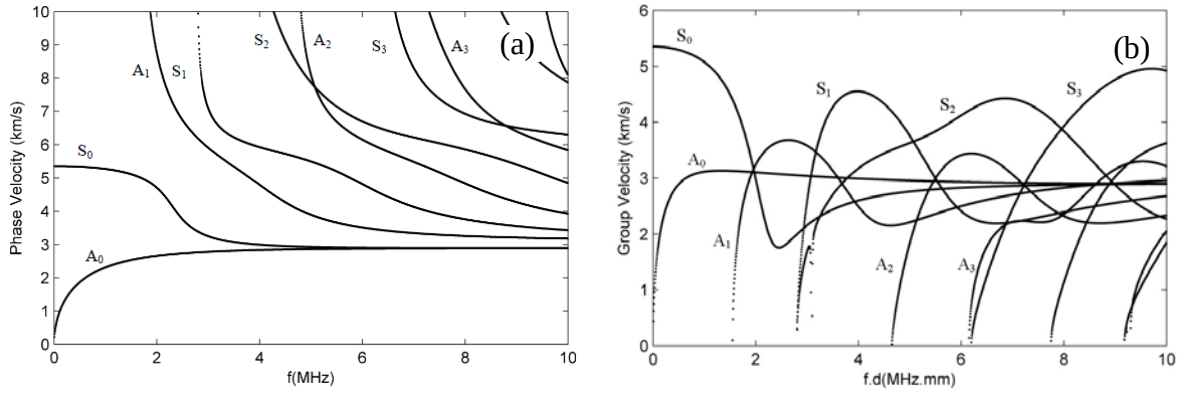

Figure 5.1. Dispersion curves for an aluminum plate in vacuum. (a) Phase velocity, (b) group velocity. Courtesy of Mr. A. Bagheri.

5.3 PLATE THICKNESS

Six defect-free aluminum plates of different thickness were tested. Each plate was investigated seventy times to increase the statistical population data.

5.3.1 Experimental setup

A 8-ns Q-switched Nd:YAG pulsed laser (CFR 200, Quantel USA) operating at 0.532 μm was used to probe the plates immersed in a tank filled with water. We tested five aluminum plates of equal dimension (50.8 mm x 50.8 mm) in addition to the same plate used for the tests of Chapter 4 (750 mm x 1605 mm x 2.54 mm). The thicknesses were:

- 1.016 mm
- 2.0 mm
- 3.175 mm
- 6.35 mm
- 9.25 mm.

The nominal level of output energy was equal to 180 mJ. A 1-mm diameter laser beam was delivered to the surface of the plate by means of a mirror and a PCX with focal length of 100 mm (Newport, KPX094AR.14). Two immersion transducers (T1 and T2) resonant at 1 MHz, 0.5” in diameter (Olympus NDT, V303-SU, Part ID: U8423005) were used to receive the laser-generated ultrasound and they were arranged in a straight-line receiving mode, 10 cm and 25 cm apart from the laser impinging, respectively. Figure 5.2 shows a typical plan view with dimensions of the plates and the location of the transducers at location 1(T1) and 2 (T2). According to Snell’s law, we inclined the transducers at 16° to maximize the sensitivity to the

leaky S_0 mode. Each plate was positioned on two supports, and the level of water above each plate was kept at 32 mm (adjusted each time according to the plate thickness).

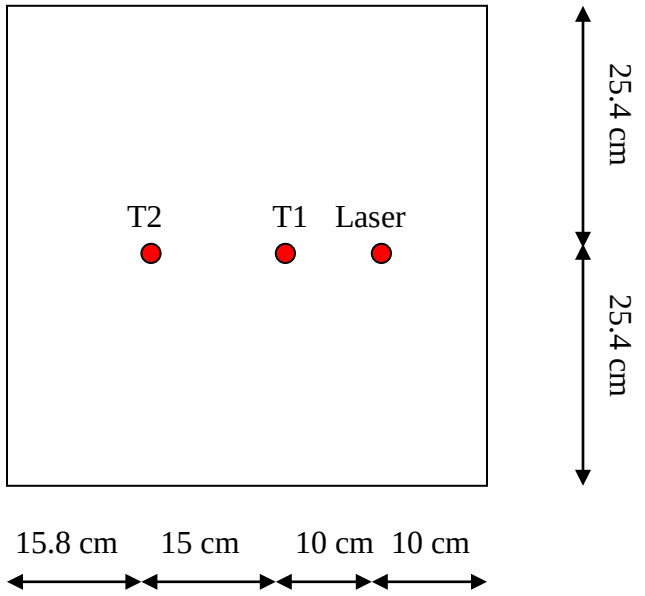

Figure 5.2. Typical plan view of plate dimensions and transducers location.

We used the same system made of the laser head and the transducers secured to a movable metallic bench plate employed in the tests of Chapter 4. However, motion was not include being outside the scope of this research. A front user interface, running under LabVIEW, was coded to control proper parameters for the generation, detection, and the storage of the ultrasonic waves. Figure 5.3 shows the typical setup adopted for all the plate thickness during the experiments.

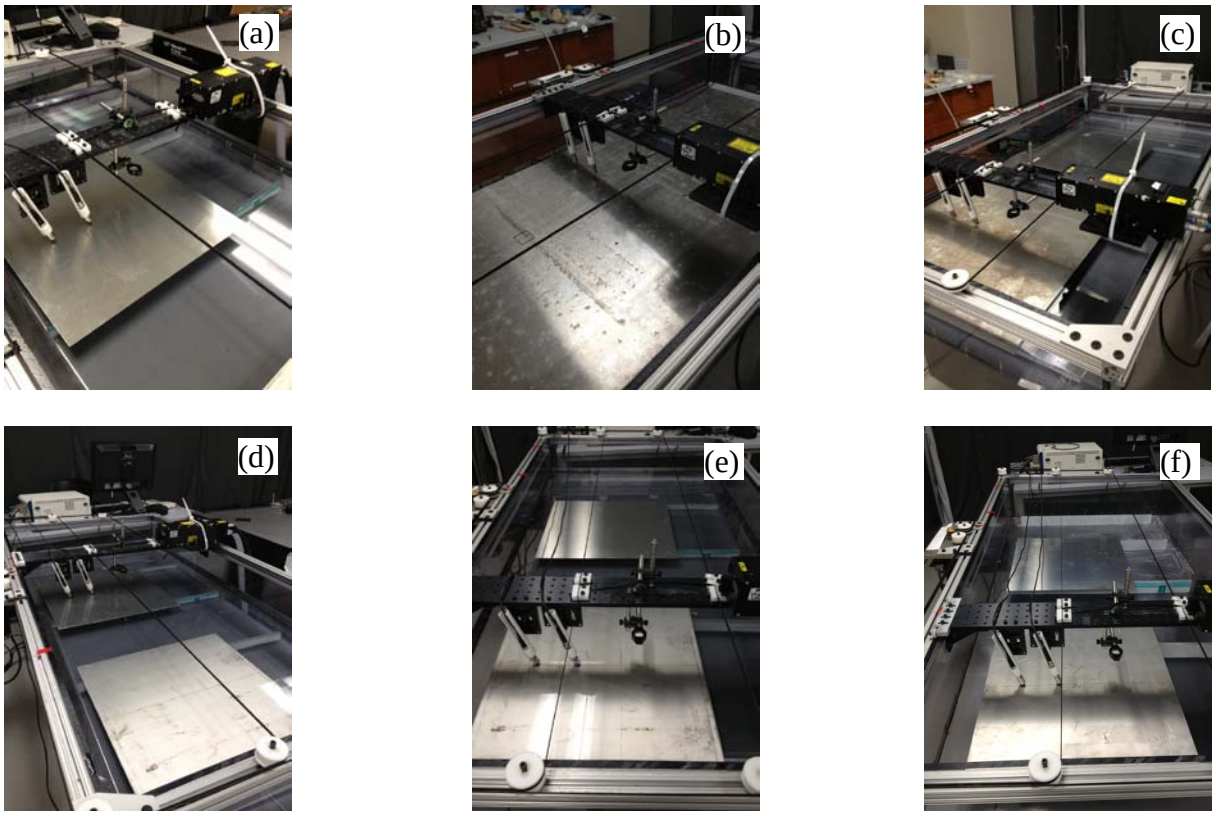

Figure 5.3. Plate thickness test I, photo of the experimental setup. Plates with thickness: (a) 1.016 mm, (b) 2 mm, (c) 2.54 mm, (d) 3.175 mm, (e) 6.35 mm and (f) 9.25 mm.

5.3.2 Results and discussion

We computed the GWT scalograms for all the time waveforms in order to extract the time-frequency content of the leaky Lamb waves. In particular, we restricted the study to the time window between 0-50 μs since it includes the arrival time frame of the S_0 mode, being the fastest and most stable mode. From the GWT scalogram we extracted the time of arrival at location 1 and 2 of the peak energy at the various frequencies. From the average value of this quantity, and knowing the distance between the transducers (100 mm), we extracted the experimental group velocity Cg according to Equation (5.1). The experimental value of Cg was then compared with

the theoretical value that can be obtained from the dispersion curves reproduced in Figure 5.1 in correspondence of the specific product $f_{max}*d$ of the of the maximum frequency f_{max} and thickness d. Please note that we referred to dispersion curves for aluminum plates in dry conditions. However, we consider this analysis still accurate, since the main difference between dry conditions and the coupling of water is in the attenuation of the ultrasonic waves and not in the mode shape of the waves [82]. First, the calculation of the group velocities was conducted to be certain that the modes detected, despite the time of arrival, were exactly the first fundamental symmetric ones. Then, the scope of the analysis includes the possibility of marking a trend of peak energies as a function of thickness for aluminum plates immersed in water. The transducers were always kept inclined at 16° which is the angle that maximizes the first symmetric mode for phase velocities of 5.3 mm/μs, i.e., we considered the phase velocity as if it were constant during the experiments despite the different thickness of the various plates. However, this simplification was considered acceptable since a velocity of ± 0.5 km/s will lead to a variation of the angle of about ±2°.

Figures 5.4 to Figure 5.9 show the results associated with a single measurement, for all the plates. In particular, the time waveforms, the corresponding scalograms, the curves of all the maximum amplitude of the GWT coefficients as a function of frequency and the group velocity Cg are presented.

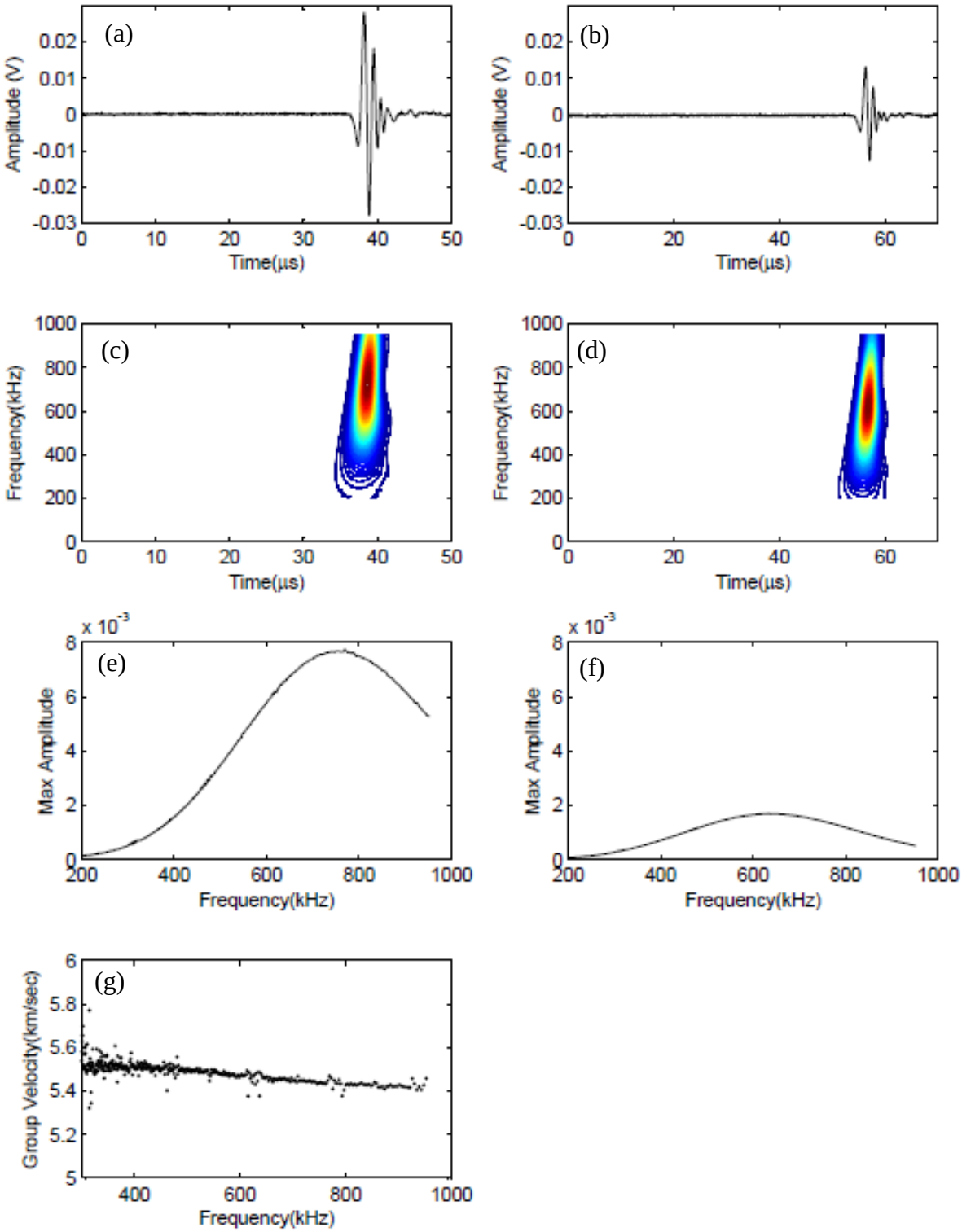

Figure 5.4. 1.016 mm plate. Time waveforms recorded by (a) T1 and (b) T2. Scalograms for time waveforms at (c) a and (d) b. Maximum amplitude vs. frequency for scalogram (e) c and (f) d. (g) Calculated Cg.

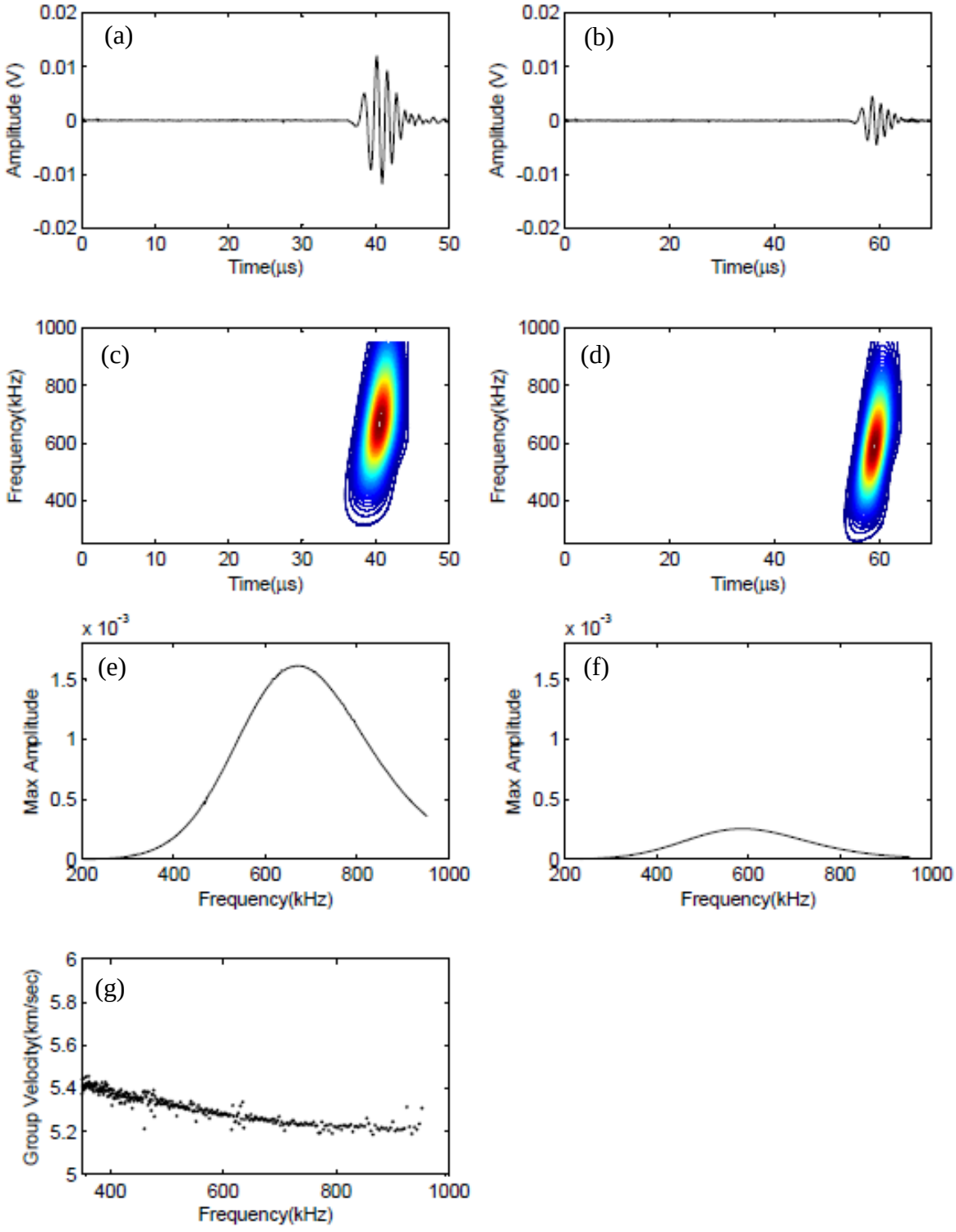

Figure 5.5. 2.0 mm plate. Time waveforms recorded by (a) T1 and (b) T2. Scalograms for time waveforms at (c) a and (d) b. Maximum amplitude vs. frequency for scalogram (e) c and (f) d. (g) Calculated Cg.

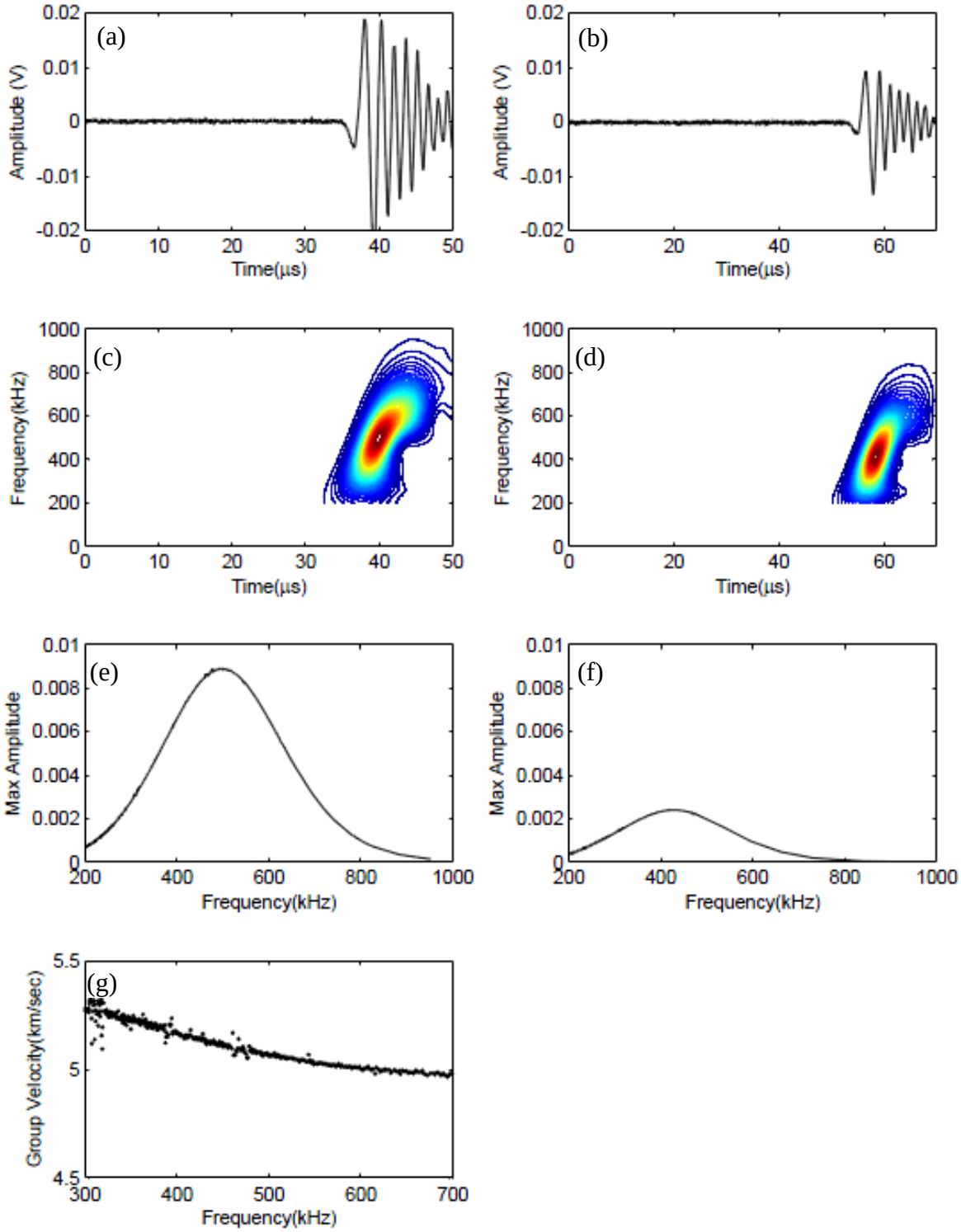

Figure 5.6. 2.54 mm plate. Time waveforms recorded by (a) T1 and (b) T2. Scalograms for time waveforms at (c) a and (d) b. Maximum amplitude vs. frequency for scalogram (e) c and (f) d. (g) Calculated Cg.

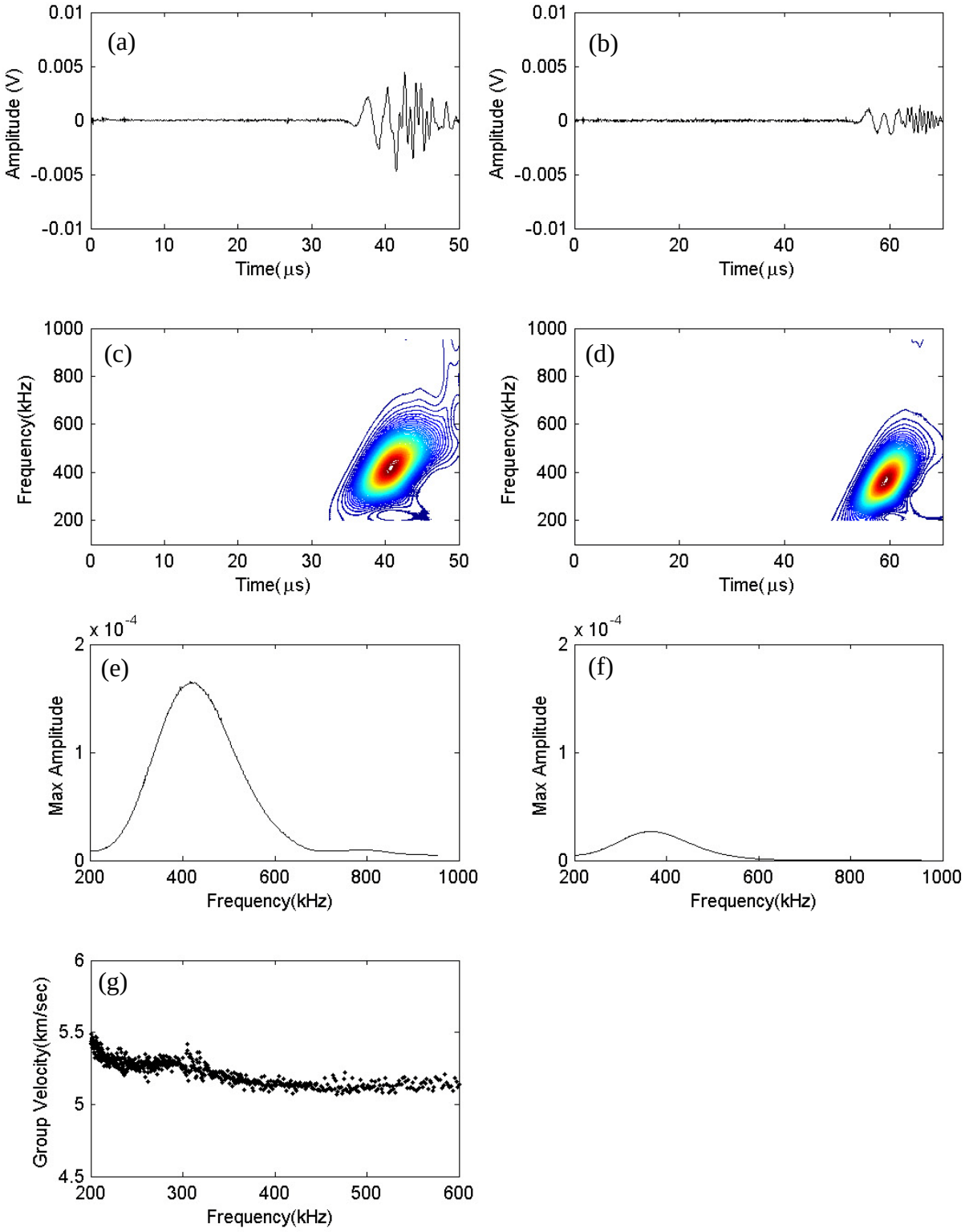

Figure 5.7. 3.175 mm plate. Time waveforms recorded by (a) T1 and (b) T2. Scalograms for time waveforms at (c) a and (d) b. Maximum amplitude vs. frequency for scalogram (e) c and (f) d. (g) Calculated Cg.

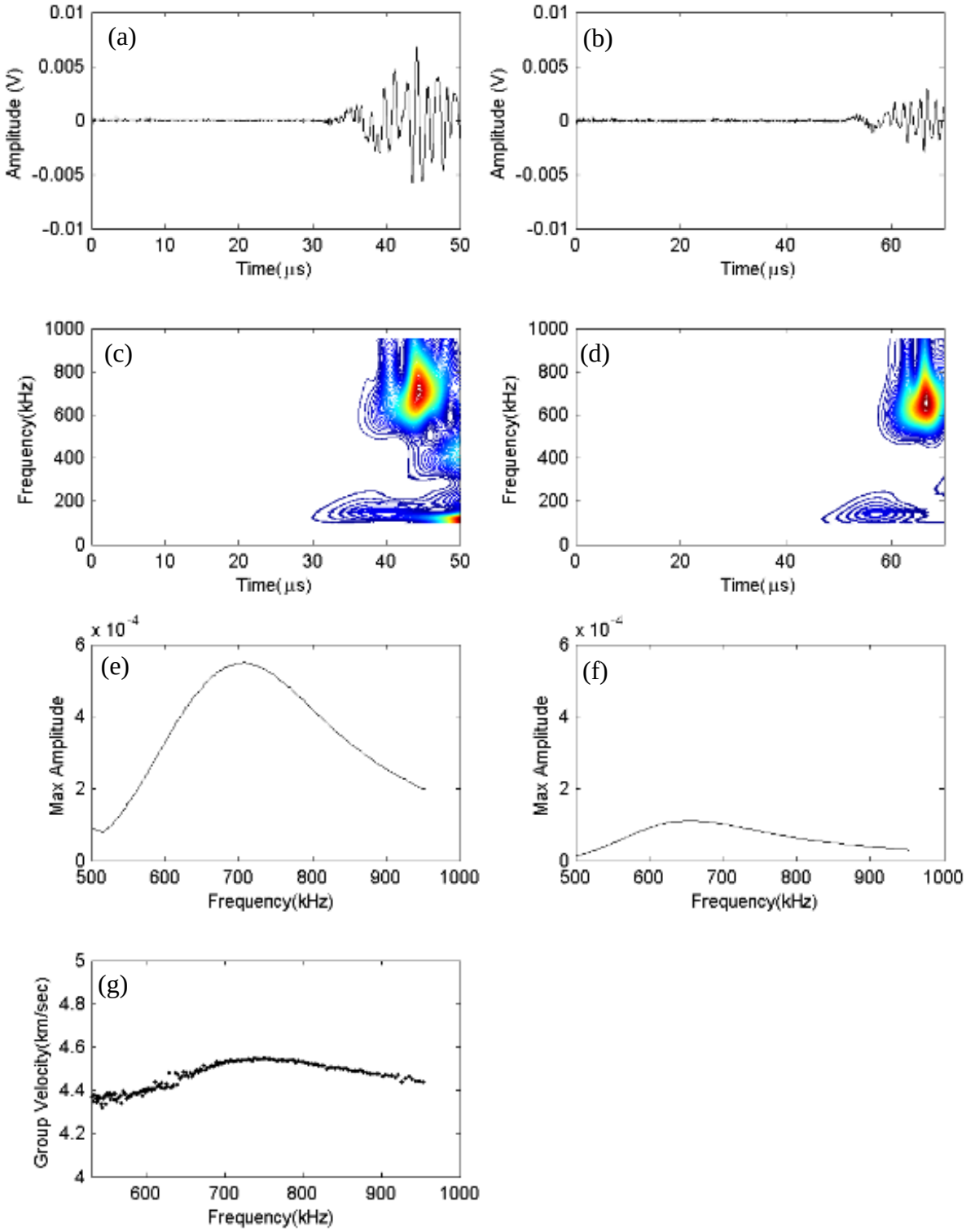

Figure 5.8. 6.35 mm plate. Time waveforms recorded by (a) T1 and (b) T2. Scalograms for time waveforms at (c) a and (d) b. Maximum amplitude vs. frequency for scalogram (e) c and (f) d. (g) Calculated Cg.

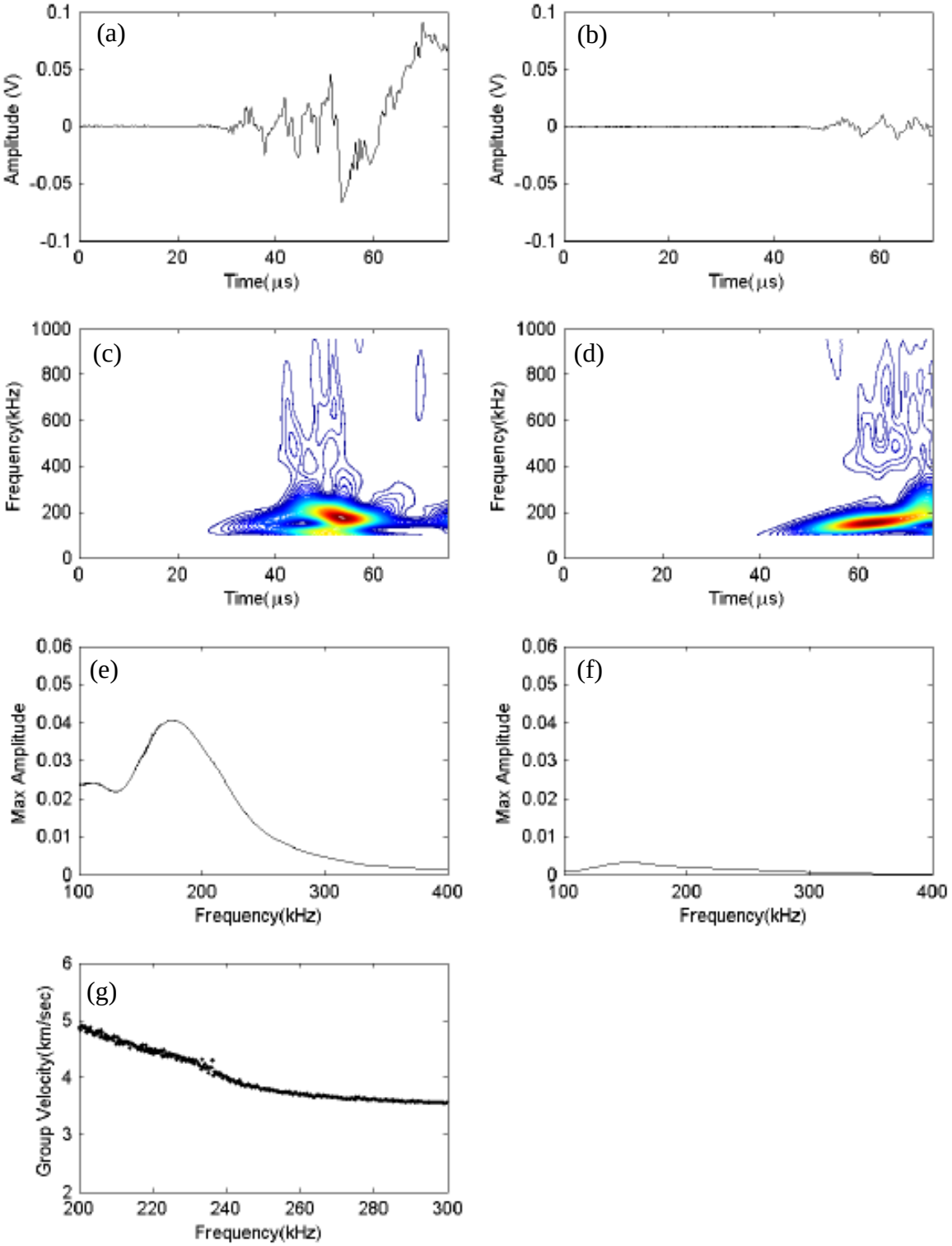

Figure 5.9. 9.525 mm plate. Time waveforms recorded by (a) T1 and (b) T2. Scalograms for time waveforms at (c) a and (d) b. Maximum amplitude vs. frequency for scalogram (e) c and (f) d. (g) Calculated Cg.

From our analysis it is possible to see that the time waveforms, as the thickness increases, are becoming more complicated. The hypothesis that a limit dependent on thickness exists such that the Lamb waves or the Rayleigh waves dominate the time domain was experimentally proven. Table 5.1 summarizes the frequency peak, the measured *Cg* and the theoretical *Cg* for the S_0, and for other few modes, such as the A_0 and A_1 modes. It is possible to see that the product $f_{max}*d$ is not constant. In fact, as the thickness increases, the peak energy decreases. For plates 1.016 mm, 2 mm, 2.54 mm, 3.175 mm thick, the presence of the S_0 mode is well defined. The calculated values are around 5.0 mm/μs, as theoretically expected. In all these cases, as also shown in Figures 5.4-5.7, the time domain is showing a clear blob resembling the classic shape of the S_0 mode. However, as the thickness approaches the 6 mm and beyond, the time waveforms become less clear. A GWT analysis that was also including the time window beyond 50 μs was necessary to attempt the detection of the S_0 mode. As the product $f_{max}*d$ increases, the dispersion curves predict the existence of many modes. In the case of the 6 mm thick plate, the detection of the S_0 mode was not achieved. However, at higher thickness such as the 9.525 mm, we succeed again at detecting the S_0 mode.

Table 5.1. Theoretical and experimental Cg as a function of the plate thickness.

Thickness (d)	**mm**	**1.016**	**2**	**2.54**	**3.175**	**6.35**			**9.525**
Frequency peak (f_{max})	**MHz**	0.7	0.64	0.5	0.4	0.68	0.45	0.15	0.17
f_{max}*d	**kHz-mm**	0.71	1.28	1.27	1.27	4.32	2.86	0.95	1.62
C_g - Theoretical (mm/μs)	**S_0**	5.30	5.00	4.90	4.90	2.70	2.00	5.10	4.00
C_g - Theoretical (mm/μs)	**A_0**	3.10	3.10	3.10	3.10	3.00	3.00	3.00	3.00
C_g - Theoretical (mm/μs)	**S_1**					4.40			
C_g - Theoretical (mm/μs)	**A_1**						3.60		
C_g - Measured (mm/μs)		**5.5**	**5.3**	**5.2**	**5.2**	**4.50**	**3.60**	**3.80**	**4.5**
		S_0	**S_0**	**S_0**	**S_0**	**S_1**	**A_1**	**?**	**S_0**

From the calculated group velocities, confirmed by the theoretical comparison, it was possible to mark a trend of the peak energy value vs. thickness. In particular, Figure 5.10 shows the maximum frequency extracted from the scalograms as a function of thickness and the red line represents an exponential trend fitting the data.

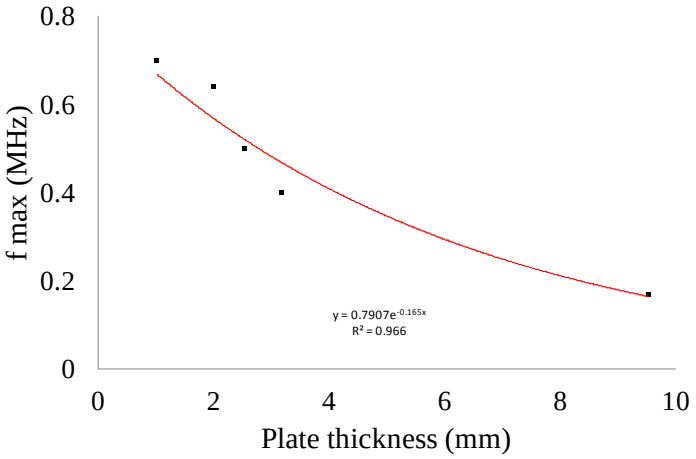

Figure 5.10. Max frequency as a function of the plate thickness.

The case of the 6 mm thick plate is not included since it was not possible to clearly detect the S_0 mode. It is possible to see that, as the thickness increases, the peak energy decreases. This can be particularly useful in real applications where the notion of possible velocity at certain thickness can be of aid for the selection of the proper inclination angle of the transducers.

The reason for the dependence between thickness and peak energy concentration can be found in the phase velocity diagram of Figure 5.1. By keeping the inclination of the transducers constant at 16° and by applying Snell's law, we maximize specific modes such as the S_0, A_1, S_1, etc. that are in fact the ones most commonly detected by our analysis. Once the phase velocity of a specific mode (for example S_0) is determined, and either f_{max} or d are known, as matter of inversion of the product $f_{max}.d$, the relation between f_{max} and d can be obtained.

As a matter of comparison, we compared the experimental *Cg* velocities for the S_0 mode with the theoretical prediction accomplished by the SAFE method. In particular, we conducted this analysis for the 1.016 mm, 2 mm, 2.54 mm, 3.175 mm thick plates, since we obtained for this thickness values the most reliable results. Figure 5.11 shows the *Cg* values as a function of $f_{max}.d$ product for the above mentioned plates. The SAFE curve is plotted with continuous line while the experimental values have dotted lines. As can be seen, the agreement between the two methods is satisfactory.

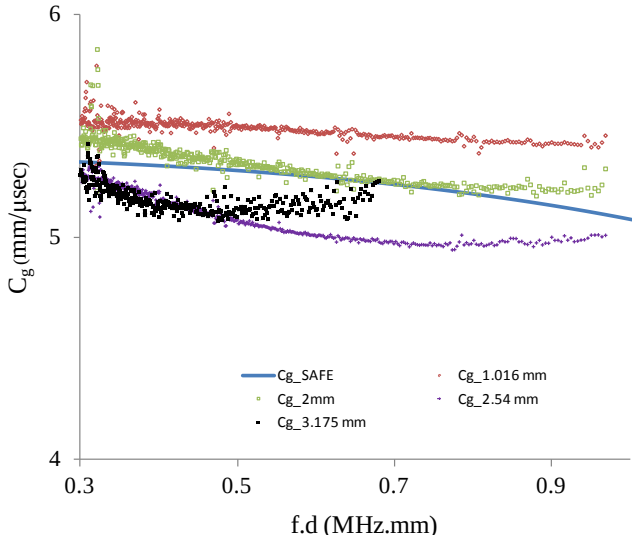

Figure 5.11. Experimental Cg for 1.016 mm, 2 mm, 2.54 mm and 3.175 mm and theoretical curve obtained with the SAFE method.

5.3.3 Conclusions

In the study reported in this chapter we investigated the effect of thickness on laser-generated ultrasonic waves. First, we tested six aluminum plates of thickness ranging from 1.016 mm to 9.525 mm immersed in water. We laser-irradiated a single spot seventy times and we received

the leaky Lamb waves by means of two immersion transducers. The transducers were aligned along the same direction of the propagation of the ultrasonic waves. The group velocity of the waves was calculated since the distance between the transducers was known and the time of arrival of the peak energy of the GWT scalograms was calculated. These experimental values were then compared with the theoretical ones extrapolated by the dispersion curves for an aluminum plate in dry conditions. This procedure allows us to confirm the type of modes we were observing and, consequently, that above a certain thickness threshold additional modes were generated. In fact, above 6 mm thickness, the shape of the waves became complex due the presence of additional modes (increased $f_{max}*d$ product). Nonetheless, it was possible to trace a decaying trend of the peak energy as a function of the thickness and we demonstrated that the $f_{max}*d$ product was not constant as the thickness varies. The dependence between peak energy and thickness can be explained by looking at the phase velocity dispersion curve for a dry aluminum plate. In fact, by keeping the transducers constantly inclined at 16° and by applying Snell's law, the relation between f_{max} and d can be obtained once either value for f_{max} or d are known.

The tabulation of peak energy values can be particularly useful in practical applications such as the investigations of immersed structures of various thicknesses. In fact, by knowing the group velocity of the wave packet of interest, peak energies can be predicted on the basis of a specific thickness.

6.0 DAMAGE DETECTION OF IMMERSED PLATES BY MEANS OF FOCUSED TRANSDUCER

In the study presented in this chapter we replaced the pulsed-laser with an immersion transducer. The aim is to compare the two methods for the generation of leaky lamb waves. Usually, the actuator was lighter and easier to operate. The setup was similar to the one presented in Chapter 4 and 5. We tested the same aluminum plate used during the experiment illustrated in Chapter 4.5.

The first section of this chapter will introduce the theoretical basis of this research as well as the background. The second section will discuss the experimental results collected during a test where a single focused transducer was used as actuator and five immersion transducers were used as receivers.

6.1 INTRODUCTION

The use and detection of leaky Lamb waves in immersed plates was already proved in 1984 by *Billy et al.* [182] where two transducers were used to test underwater steel plates of varying thickness (0.5 to 3 mm). Figure 6.1 shows the experimental setup they adopted [182]. In the first set of experiments, the transmitter was used in pulse-echo, and the back reflected leaky Lamb waves were measured. In the second set, another transducer was positioned at the opposite side

of the plate and the backward transmitted ultrasonic signals were recorded. In both cases, leaky Lamb waves at various angles of incidence (various propagating modes) were recorded. Very similar studies have been conducted for leaky Rayleigh waves [183-185].

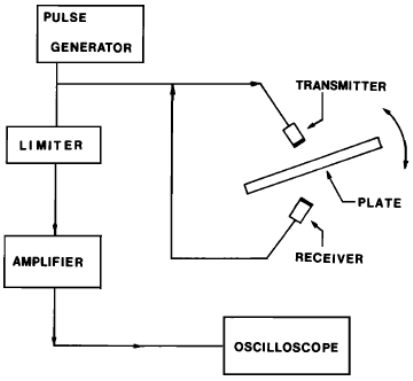

Figure 6.1. Experimental setup used for the measurement of leaky Lamb waves [182].

Studies have also been conducted on the use of leaky Lamb waves for composite plates immersed in water to experimentally measure the material properties of the plates and to derive the dispersion curves [186][187]. The most common setup consists of a plate immersed in a water bath inclined at different Lamb angles and of two transducers in a pitch catch or in through transmission configurations [186][187]. The use and application to NDE of leaky Lamb waves in immersed plates of various materials was also investigated by numerous authors both experimentally and theoretically [188-197]. However, in the cases cited above, the setup usually consists of a pair of transducers to extract the mechanical properties of the material as well as the attenuation curves.

6.2 EXPERIMENTAL SETUP

A spherical focused (Olympus NDT, V303, SU-F) transducer (0.5” in diameter) was insonifying an aluminum plate (750 x 1605 x 2.54 mm) immersed in water. Five immersion transducers (Olympus NDT, V303-SU, Part ID: 8423005) arranged to form a half-circle were used as receivers. The setup is arranged in pitch-catch mode facing the upper surface of the plate. The actuator was placed in the center of the circle in order to guarantee the same distance between the actuator and the receiver. The resonant frequency of the transducers was 1 Mhz. Figure 6.2 shows the experimental setup.

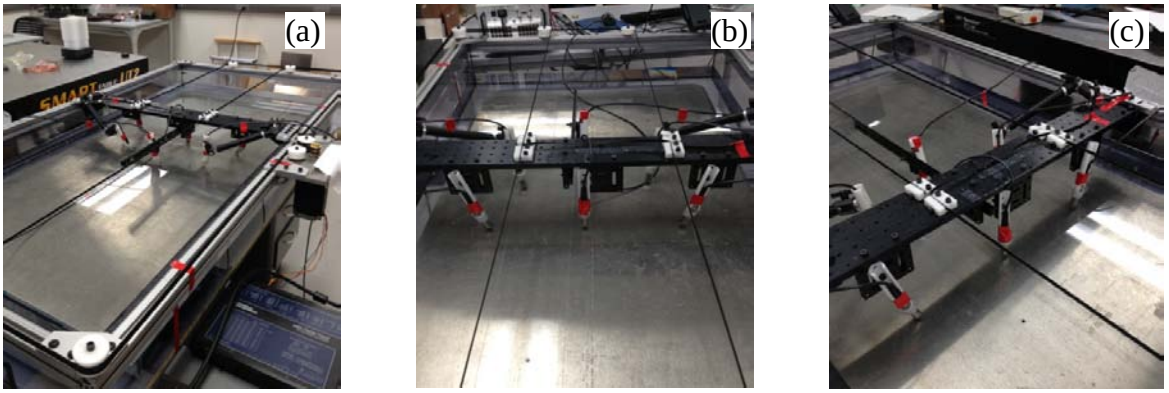

Figure 6.2. Experimental setup. (a,b,c) Photos of the scanning system and close up-view of the ultrasonic transducers.

Both the actuator and the receivers were mechanically mounted on a bench plate to allow a B-scan of the plate. The plate had five defects as illustrated in Chapter 4.5.

According to the Snell’s law, we inclined the receivers at 16° to maximize the sensitivity to the leaky S_0 mode with a lift-off distance equal to 15 mm with respect to the surface of the plate. The lift-off distance of the focused transducer is 16 mm (0.62 in FPF Spherical Focus) but he was kept in vertical position to equally insonifying all the receivers. The general setup recalls

the one described in Chapter 4.5 but with some differences. First, the position of the plate with respect to the supports has changed. Then, the sensing path was incremented. This allowed probing a wider area with a single burst. The scanning points were increased to 57 since the distance between two successive points is now equal to 20 mm. The type, the location and the label of the defects were the same as the ones adopted in Chapter 4.5. Figure 6.3 show the plan view of the plate, the position of the supports, the location and label of the transducers, the defect legenda, as well as some significant scanning points.

The motion of the bench plate was guaranteed by pulleys and belts driven by a National Instrument PXI unit as outlined in Chapter 4.4. A front user interface, running under LabVIEW, was coded to control the motion of the scan and to select the proper parameters for the generation, detection, and the storage of the ultrasonic waves. A function generator (NI PXI 5412) was used to produce five cycles tone burst with center frequency at 500 kHz, following the results of Chapter 5. The signal output was amplified by a linear amplifier (Piezo Systems, INC. Linear Preamplifier, Model EPA-104) and the output voltage reaching the actuator was measured to be 16V peak-to-peak. The leaky Lamb waves, after being sensed by the five immersion transducers, were amplified by 60 dB using a linear preamplifier (Olympus NDT, Model 5660C). In addition, 200 averages were taken for each scanning point to improve the SNR. The plate was tested five times as in former tests.

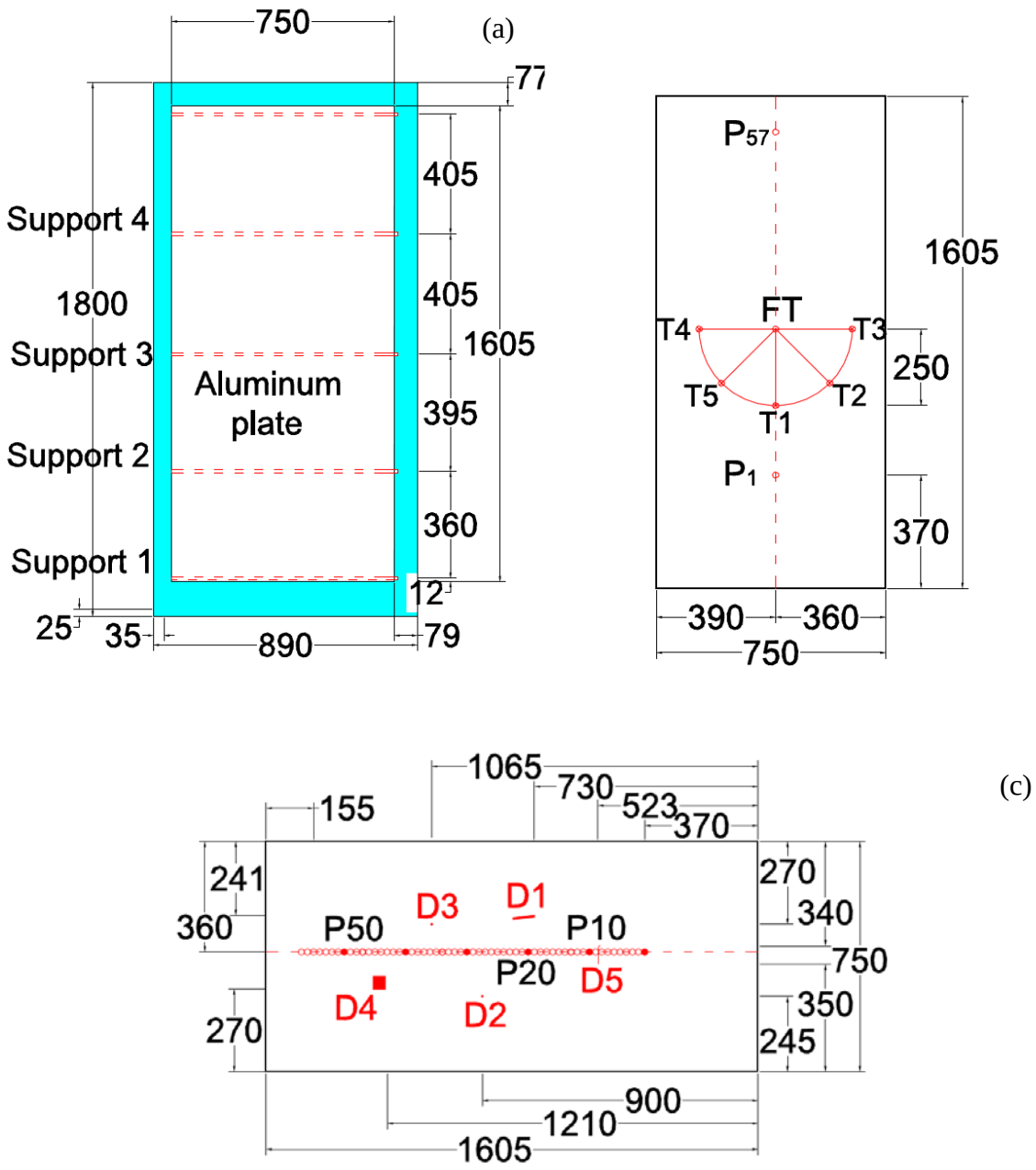

Figure 6.3. Schematics of the setup. (a) plan view of the plate and the tank. (b) Details of the position of the transducers (T1, T2, T3, T4, T5) in vertical position. (c) Defects legenda. The drawings are on scale and all the quotes are in millimeters.

6.3 SETUP ASSESSMENT

Figure 6.4 shows a typical time waveforms recorded at point n. 7 by the five sensors for scan 1. Point 7 was defect-free. As can be seen, the amplitude is very similar in all cases, except for transducer 5 where the amplitude is slightly smaller.

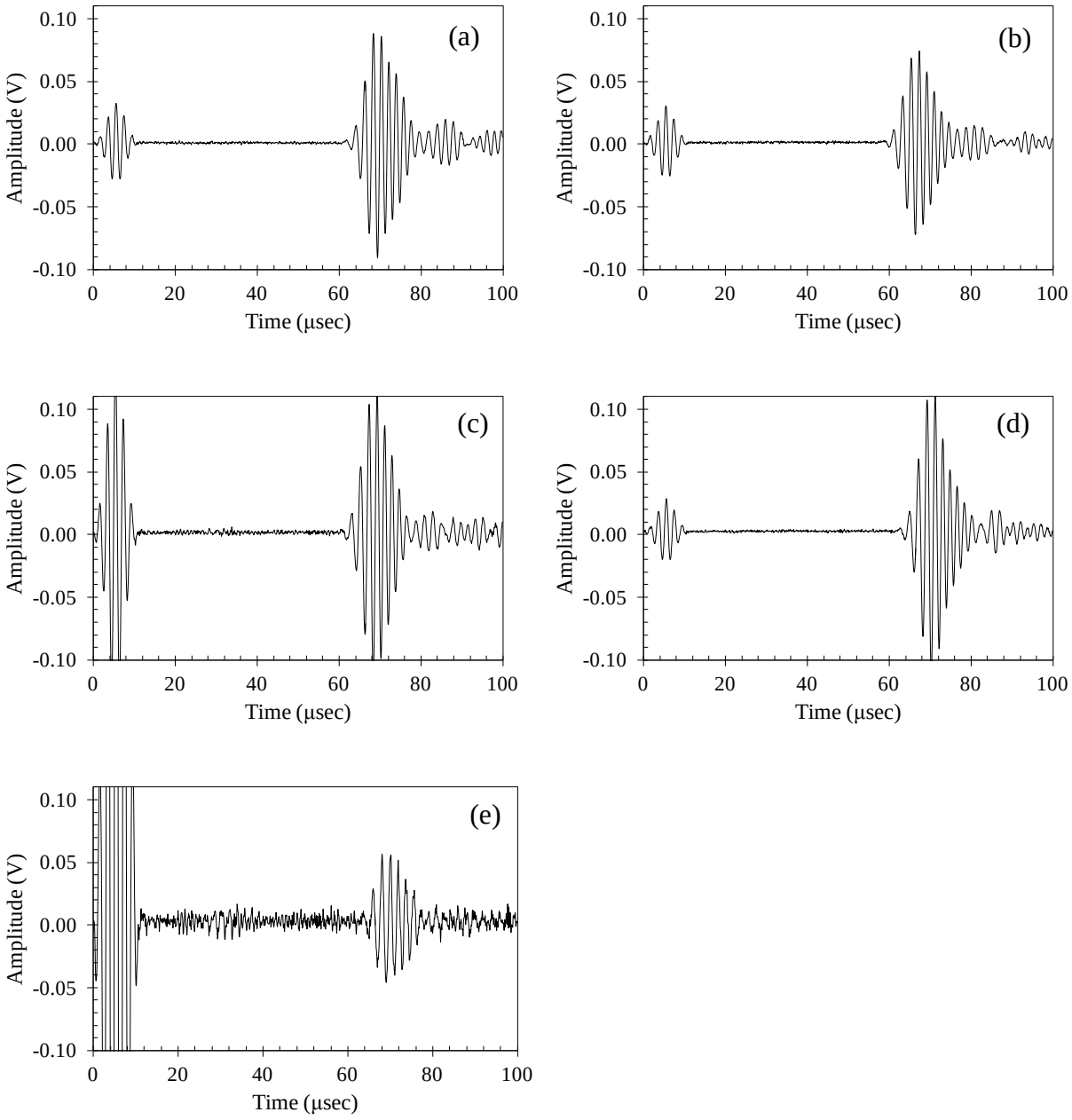

Figure 6.4. Experimental time waveforms by (a) T1, (b) T2, (c) T3,(d) T4, (e) T5.

Three main wave packets are visible. The packet included between 60 and 80 μsec is the leaky S_0 mode. The small wave packet beyond 80 μsec is likely generated by the interaction of the leaky S_0 mode and the liquid-air interfaces while the wave packet at the beginning of the time window is cross-talk noise. In this study we considered the signal between 60 and 80 μsec.

First, we evaluated the repeatability of the methodology by performing a cross-correlation analysis of the signals in the time window 60-80 μsec. In particular, we used the time waveforms recorded at each point during the first scan as the reference signal for the successive scans. Therefore, we calculated the cross-correlation of the time waveforms associated with the remaining four scans with respect to the reference signals. For instance, the waveforms related to point 10 of scan 2 to 5 were all cross-correlated to the waveform of point 10 of the first scan and so on for all the scanning points. Figure 6.5 shows the cross-correlation as a function of the scan points for all the scans and relative to all transducers. As can be seen, the cross-correlation is high, thus confirm the repeatability of the methodology. The scatters in Figure 6.5a can be explained with the fact that defects were between the actuator and transducer 1. Point 10 was affected by the presence of the horizontal cut, while location 40 was affected by the presence of corrosion. Similarly, the scatters around point 20 in Figure 6.5c are the results of the proximity of defect 2 (vertical cut) to transducer 3. Finally, the the scatters around point 40 in Figure 6.5d can be explained with the vicinity between transducer 3 and the defect 4 (corrosion). The high repeatability of transducer 5 is justified by the fact that this transducer is the least influenced by the presence of damage. Overall the values of the cross-correlation shown in Figure 6.5 are higher than those presented in Chapter 4.4.1 and relative to laser-based wave generation. This is due to the shorter duration of the test which reduced the number of coalesced gas bubbles

trapped in water. Moreover, the generation of ultrasound with a transducer is more repeatable than with a pulsed laser.

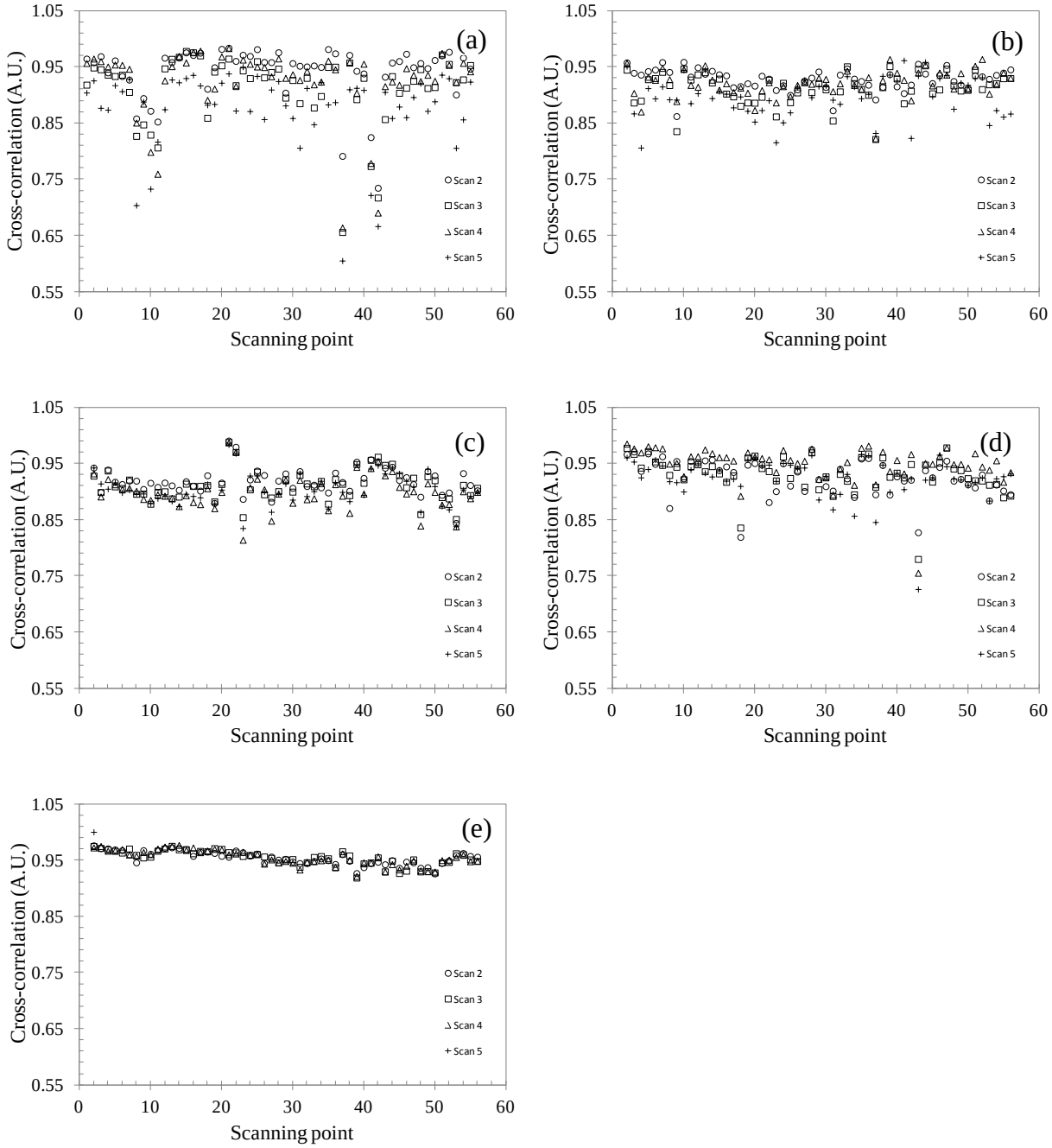

Figure 6.5. Experimental results relative to all scans. Cross-correlation as a function of the scanning point. (a) T1, (b) T2, (c) T3, (d) T4, (e) T5.

6.4 SHM ALGORITHM

Figure 6.6 shows the corresponding GWT scalograms of the time waveforms presented in Figure 6.4. The scalograms show that the energy of the leaky S_0 mode is dominant at 500 kHz, consistent with the results of Chapter 4.5 and with the fact that a 500 kHz modulated tone burst was used as exciting wave.

Figure 6.7 shows the Fast Fourier Transform (FFT) of the time waveforms presented in Figure 6.4 in the frequency range 0-3 MHz. A peak comprised around 500 kHz is visible in accordance with the peak energy concentration of the scalograms. The good repeatability of the signals is also confirmed by the high similarity of the time frequency results.

Following the same procedure outlined in Chapter 4.5.1, we extrapolated from these graphs the first seven features introduced in Chapter 4.5.1 and listed in Table 4.2. In accordance with the results found in Chapter 4.5.4., we excluded the feature related to the FWHM. The algorithm used here closely follows the procedure presented in Chapter 4.5.1.

We considered defects all the points that fall into the area covered by the semi-circle of the transducers. This implies that the guided waves generated by the actuator at 37 out of 57 locations should be affected by at least one defect prior to leak and being sensed by the sensors.

For sake of completeness, Figure 6.8 shows two typical curves extracted from the scalograms in order to compute features 1, 4 and 5. In particular, Figure 6.8a displays the values of the largest wavelet coefficients at each frequency while Figure 6.8b displays the values of the largest wavelet coefficients at each time.

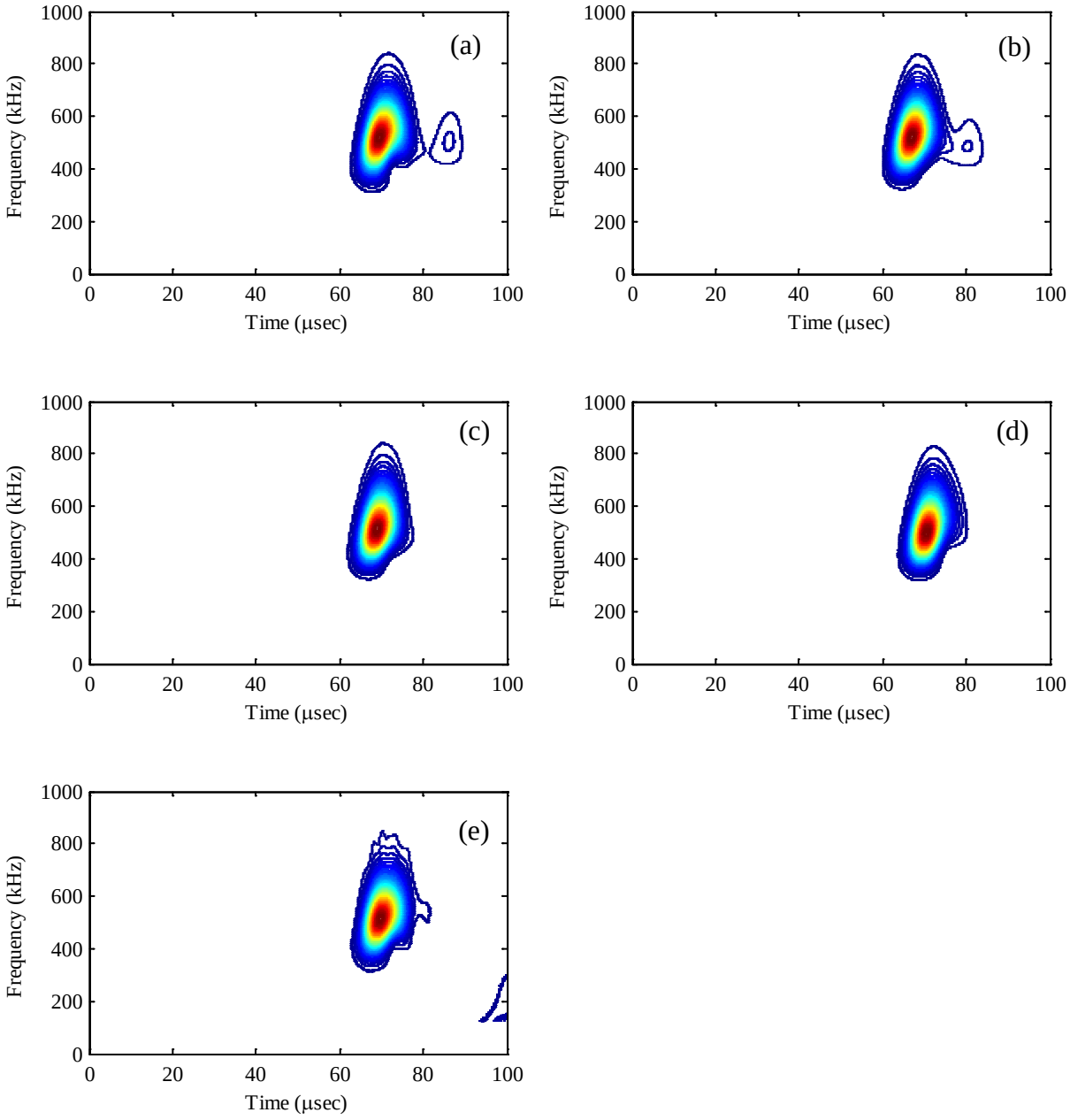

Figure 6.6. GWT scalograms associated with the time waveforms presented in Figure 6.4.

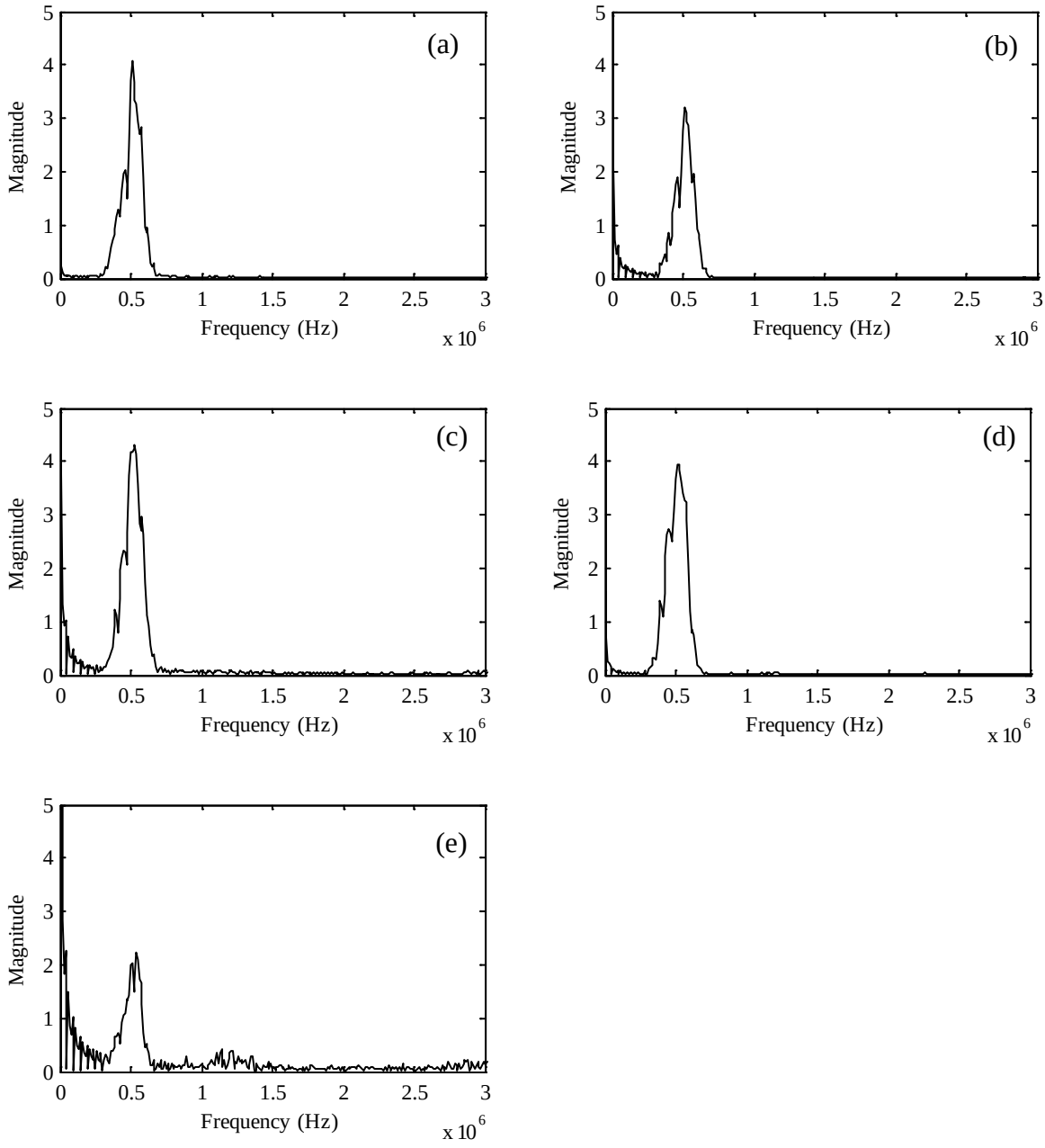

Figure 6.7. FFTs associated with the time waveforms presented in Figure 6.4.

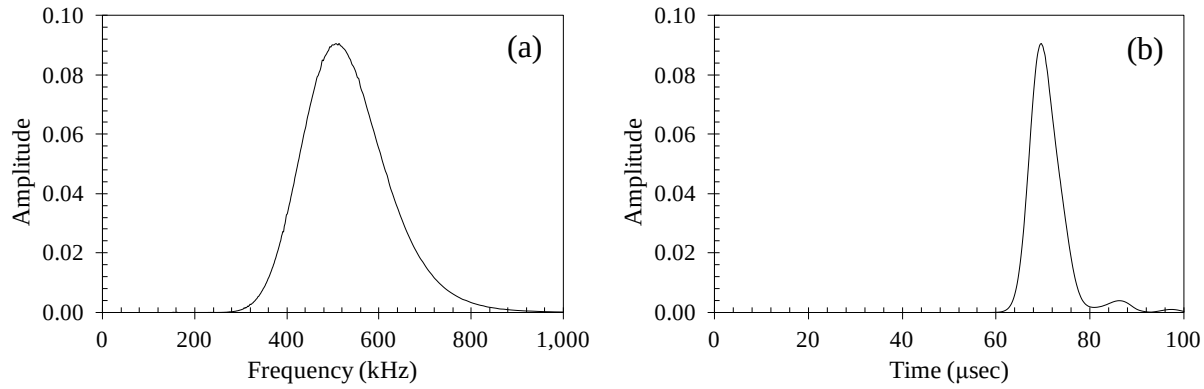

Figure 6.8. Joint time–frequency domain associated with the data from transducer T1: (a) largest wavelet coefficients as a function of the frequency and (b) largest wavelet coefficients as a function of the time of arrival.

Figure 6.9 show three D.I.s calculated according to Equation 4.8., namely $D.I._{(3,4)}^{(1)}$, $D.I._{(1,4)}^{(1)}$, $D.I._{(1,3)}^{(4)}$ where the sensitivity of some features with respect to the defects and the transducers could be appreciated. In particular, Figure 6.9a shows the sensitivity of transducers 3 and 4 to the vertical cut. Figure 6.9b shows the sensitivity of transducers 1 and 4 to corrosion. Figure 6.9c shows the sensitivity of transducers 1 and 3 to the vertical cut.

Finally, the D.I.s were collected to form a multi-dimensional vector for the unsupervised learning algorithm based on outlier analysis. In this analysis, the baseline consisted of 80 samples (= 16 pristine locations x 5 scans).

The normal probability plot was computed to verify the Gaussian distribution of the baseline, proved by the fact that the data should be centered on the values of 1, which identifies the structure in its pristine conditions. For illustrative purposes, Figure 6.10 shows the baseline associated with three indexes, namely, $D.I._{(1,2)}^{(2)}$, $D.I._{(1,3)}^{(2)}$, $D.I._{(1,4)}^{(2)}$. Since all the data are clustered to the line and the same was proved for the whole baseline, we can assume that the baseline is normally distributed [177].

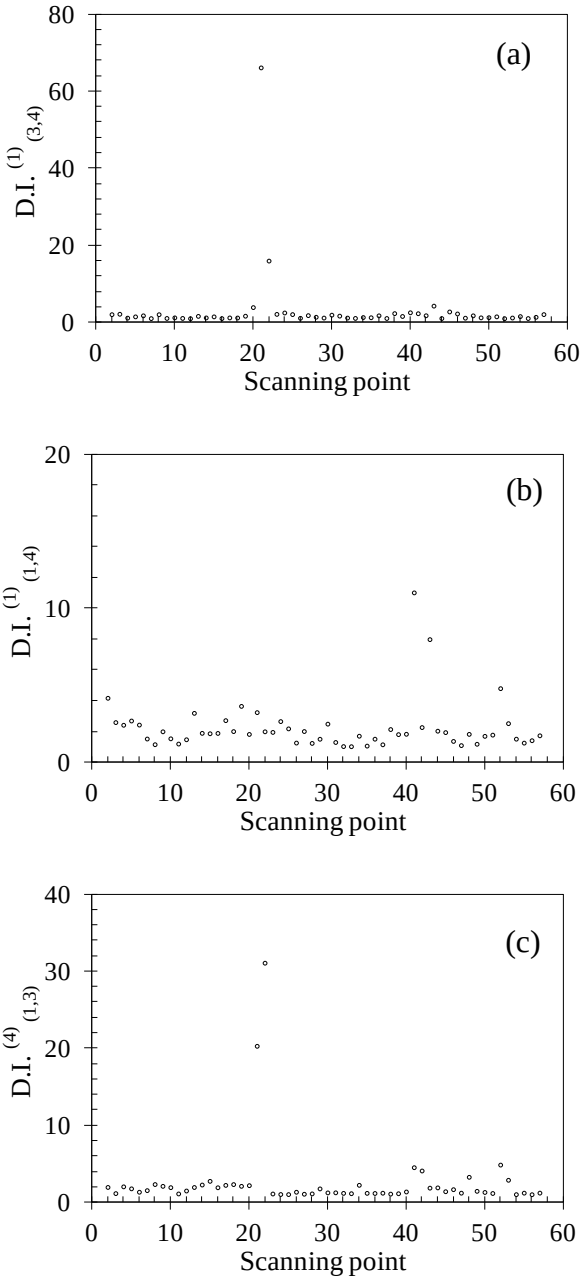

Figure 6.9. Damage index as a function of the sampling: (a) $D.I._{(3,4)}^{(1)}$ (b) $D.I._{(1,4)}^{(1)}$ and (c) $D.I._{(1,3)}^{(4)}$.

Once the values of D_ζ according to Equation (4.2) of the baseline distribution were determined, the threshold was taken as the usual value of 3σ equal to 99.73% of the Gaussian confidence limit. Then, all the data were tasted to classify damage (outlier) vs. pristine (inlier),

considering also the presence of false positive and false negative adopting an optimization approach for the features.

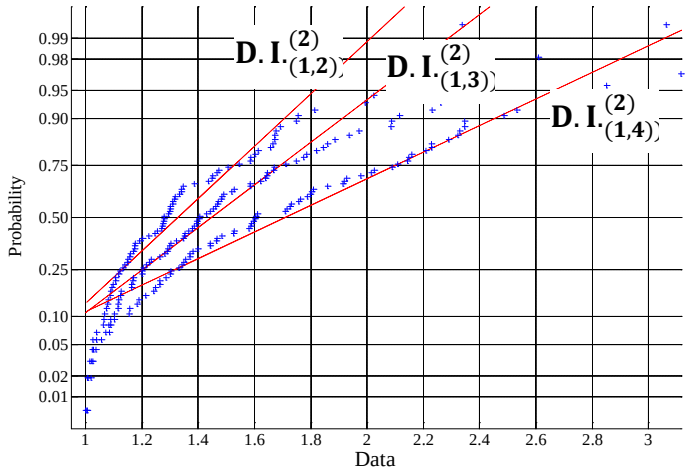

Figure 6.10. Normal probability plot for the baseline of features $D.I._{(1,2)}^{(2)}$, $D.I._{(1,3)}^{(2)}$ and $D.I._{(1,4)}^{(2)}$.

6.5 RESULTS AND DISCUSSION

We first applied the multivariate analysis using the seven features separately. The input vector in this case is 10-dimensional since five transducers can be paired in ten different combinations. The features considered separately were then paired in combinatorial subsets with the aim of increasing the sensitivity to damage compared to the single feature's case, following the procedure outlined in Chapter 4.4.3. The final set consists of all the seven features. Figure 6.11 shows the Mahalanobis squared distance as a function of the scanning points relative to three different combinations of features. The horizontal line represents the baseline threshold.

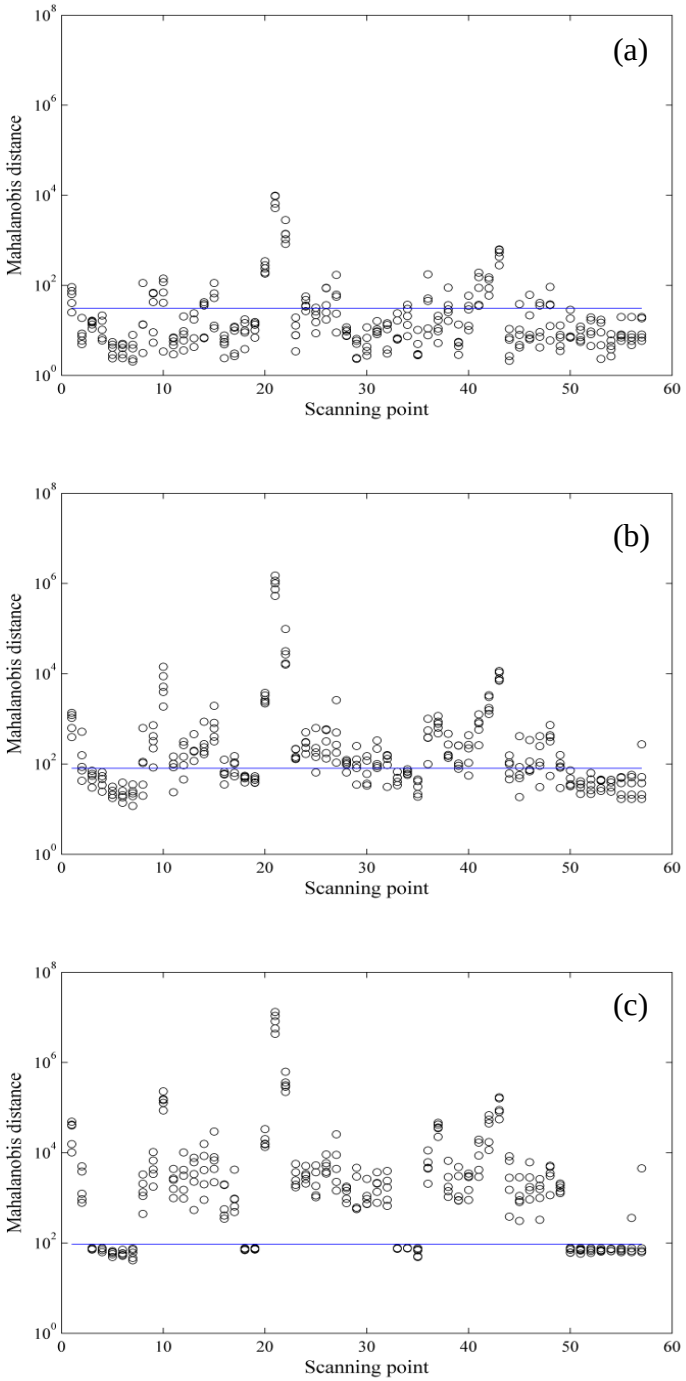

Figure 6.11. Mahalanobis square distance for feature 3 (a), for features 3,4,5,6 (b), and for all features (c).

In particular, Figure 6.11a shows the Mahalanobis squared distance as a function of the scanning points relative to the single feature 3; Figure 6.11b shows the case associated with four

features together (feature 3,4,5,6); Figure 6.11c shows for results relative to the simultaneous case of all the seven features. As proved later, these cases have the highest success rate with respect to their category. What can be noticed is that, by increasing the number of features, the sensitivity to the defect is incremented (higher amplitude in the MSD) and the number of proper outliers is higher. In fact, the case of single features provided the lowest number of proper outliers while the case of seven features produced the highest number of proper outliers and only two points (1 and 2) were categorized as false positive. Furthermore, point 56 and 57 refer to damage-free zones. Although these points were not included in the baseline dataset, the algorithm properly recognized them as inliers in the case of all seven features. A varying sensitivity of the methodology to the different defects could also be noticed. In fact, when the focused transducer is insonifying very closely to specific defects, the values of the MSD are higher. This can be noticed for the horizontal cut (around point 10), the vertical cut (around point 20), and the corrosion (around point 42).

Table 6.1, 6.2 and 6.3 summarize the results of the outlier analysis, by displaying the number of proper outliers, false positive, false negative, and proper inliers, as well as the percentage of success rate, of the false positives and of false negatives. The tables refer to single features, to four features and six features, respectively.

As can be seen, increasing the number of features increases the sensitivity to defects and the success rate. The success rate of feature 3 alone is 57.54%, whereas the success rate of all features is 95.79%. In this case, as mentioned earlier, only two points were misclassified. The case of four features is in between. Combination 3,4,5,6 provides the highest success rate, where 3 out of 4 features having the highest success rate alone are combined (2,3,5) and feature 6 has a very low percentage of false positive.

Table 6.1. Results of the multivariate damage classification for all combinations with one feature and seven features.

Comb.	No.of Outl	No.of Proper Outl	No.of False +	No.of Inliers	No.of False –	No.of Proper Inliers	No.of Totals	Success rate %	False positive %	False negative %	Tot %
1	42	39	3	243	146	97	285	47.72	1.05	51.23	100
2	66	60	6	219	125	94	285	54.04	2.11	43.86	100
3	74	69	5	211	116	95	285	57.54	1.75	40.70	100
4	40	39	1	245	146	99	285	48.42	0.35	51.23	100
5	67	63	4	218	122	96	285	55.79	1.40	42.81	100
6	53	49	4	232	136	96	285	50.88	1.40	47.72	100
7	56	49	7	229	136	93	285	49.82	2.46	47.72	100
ALL	197	185	12	88	0	88	285	95.79	4.21	0.00	100

Table 6.2. Results of the multivariate damage classification for all combinations with four features.

Comb.	No.of Outl	No.of Proper Outl	No.of False +	No.of Inliers	No.of False -	No.of Proper Inliers	No.of Totals	Success rate %	False positive %	False negative %	Tot %
1234	131	124	7	154	61	93	285	76.14	2.46	21.40	100
1235	137	129	8	148	56	92	285	77.54	2.81	19.65	100
1236	135	125	10	150	60	90	285	75.44	3.51	21.05	100
1237	132	123	9	153	62	91	285	75.09	3.16	21.75	100
1245	132	124	8	153	61	92	285	75.79	2.81	21.40	100
1246	132	125	7	153	60	93	285	76.49	2.46	21.05	100
1247	127	120	7	158	65	93	285	74.74	2.46	22.81	100
1256	146	138	8	139	47	92	285	80.70	2.81	16.49	100
1257	133	125	8	152	60	92	285	76.14	2.81	21.05	100
1267	135	127	8	150	58	92	285	76.84	2.81	20.35	100
1345	134	126	8	151	59	92	285	76.49	2.81	20.70	100
1346	139	129	10	146	56	90	285	76.84	3.51	19.65	100
1347	134	125	9	151	60	91	285	75.79	3.16	21.05	100
1356	146	138	8	139	47	92	285	80.70	2.81	16.49	100
1357	136	128	8	149	57	92	285	77.19	2.81	20.00	100
1367	134	125	9	151	60	91	285	75.79	3.16	21.05	100
1456	147	138	9	138	47	91	285	80.35	3.16	16.49	100
1457	133	126	7	152	59	93	285	76.84	2.46	20.70	100
1467	132	124	8	153	61	92	285	75.79	2.81	21.40	100
1567	144	135	9	141	50	91	285	79.30	3.16	17.54	100
2345	141	133	8	144	52	92	285	78.95	2.81	18.25	100
2346	138	129	9	147	56	91	285	77.19	3.16	19.65	100
2347	138	129	9	147	56	91	285	77.19	3.16	19.65	100
2356	143	135	8	142	50	92	285	79.65	2.81	17.54	100
2357	138	129	9	147	56	91	285	77.19	3.16	19.65	100
2367	143	134	9	142	51	91	285	78.95	3.16	17.89	100
2456	150	142	8	135	43	92	285	82.11	2.81	15.09	100
2457	139	130	9	146	55	91	285	77.54	3.16	19.30	100
2467	137	129	8	148	56	92	285	77.54	2.81	19.65	100
2567	143	134	9	142	51	91	285	78.95	3.16	17.89	100
3456	159	150	9	126	35	91	285	84.56	3.16	12.28	100

"Table 6.2 (continued)."

3457	142	134	8	143	51	92	285	79.30	2.81	17.89	100
3467	149	140	9	136	45	91	285	81.05	3.16	15.79	100
3567	149	140	9	136	45	91	285	81.05	3.16	15.79	100
4567	149	140	9	136	45	91	285	81.05	3.16	15.79	100

For sake of completeness, we also include the list of combinations with six features in order to show that a very high success rate equal to 95.44% was already achieved without considering all the seven features.

Table 6.3. Results of the multivariate damage classification for all combinations with six features.

Comb.	No.of Outl	No.of Proper Outl	No.of False +	No.of Inliers	No.of False –	No.of Proper Inliers	No.of Totals	Success rate %	False positive %	False negative %	Tot %
123456	195	183	12	90	2	88	285	95.09	4.21	0.70	100
123457	193	181	12	92	4	88	285	94.39	4.21	1.40	100
123467	194	182	12	91	3	88	285	94.74	4.21	1.05	100
123567	195	183	12	90	2	88	285	95.09	4.21	0.70	100
124567	195	183	12	90	2	88	285	95.09	4.21	0.70	100
134567	196	184	12	89	1	88	285	95.44	4.21	0.35	100
234567	196	184	12	89	1	88	285	95.44	4.21	0.35	100

6.6 COMPARISON WITH LASER METHODOLOGY

Even though the capability at detecting defects was proved with different success scale depending on the applications, some concerns about the regular use of this system for damage detection on immersed plates exist. In fact, the hazards associated with laser use as well as the need of high power can limitate the potential wide applications of the technique. Therefore, we implemented a new system hazard-free where we substitute the laser head (and as such the source of ultrasonic generation) with a focused transducer in order to implement an assembly

that is lighter and easy-to-operate. On the receiver side, the same type of immersion transducers used in Chapter 4 was employed.

This focusing methodology successfully discriminated between damaged and pristine conditions in almost all cases. The highest success rate was achieved when combining all the possible chosen features since only two points were classified as false positive. On this basis, the focusing technique achieved the best results compared to the laser technique. This can be justified by the fact that the repeatability of the whole procedure is higher in the latter case and by the fact that the spatial distribution of the transducers was more efficient. In fact, the half-moon covered a very wide area, thus leading to a constant coverage of the defects. On the other hand, the cross-configuration adopted in the first set of laser-generated test gave lower capability at detecting all the defects, but higher sensitivity to specific ones, such as the vertical cut. This can possibly depend on the type of statistical approach adopted. In fact, in the laser case only 6 ratios among 4 ‘distant’ transducers were considered for the multivariate algorithm, i.e., the quantity differ significantly from each other. In the focusing case, 10 ratios among closer transducers were considered. Despite the fact that this produced a general much higher effectiveness, it also leads to features that are more similar to each other (also due to the averaging adopting before the data storage). The higher number of features also produced a higher computational time. A possible improvement of the methodology could be to reduce the dimensionality of the features by retaining only those that are particularly sensitive to the defects.

Furthermore, the laser test requires much more time to be performed, thus allowing ionized gas bubbles to coalesce on the transducers more easily compared to the focusing case. On the other hand, the concave shape of the focused transducer easily allocates the formation of

gas bubbles, thus requiring to be checked after each scan. A possible solution could be the adoption of other type of focusing transducer for the scope.

As a concluding remark we can say that, overall, the focusing technique is better in terms of being hazard-free, more repeatable, faster and more user-friendly. Nonetheless, the laser methodology gave promising results for the noncontact monitoring of immersed plates.

6.7 CONCLUSIONS

In this chapter we presented an automated damage-detection technique for immersed metallic plates based on the noncontact generation and detection of guided ultrasonic waves. The waves were generated using a focused immersion transducer and detected by means of an array of five immersion transducers arranged in a half-moon configuration. The signals were averages 200 times before being recorded and analyzed and presented a very good repeatability as proved by the cross-correlation analysis. The signals were processed to extract seven features in the time and joint time and frequency domain. The features were then used in a multivariate outlier analysis to detect five structural damages artificially devised on the test object. In the experiments, the probing system was controlled by a hardware system designed and built in house that allowed for the automated inspection of immersed structures.

We proved that the technique was capable of identifying the defects with a success rate as high as 95.79% in the case of all the seven features. However, a success rate as high as 95.44% was already achieved with the case of six paired features. This can be explained with the fact that some features are very similar, and as such they do not improve considerably the effectiveness of the methodology. The right approach is a balance between the desired sensitivity to defects and

an acceptable computational time. The sensitivity to the defects, proved by a higher MSD value, is higher when the actuator is close to the defects.

As a concluding remark we can say that, overall, the focusing technique is better in terms of being hazard-free, more repeatable, faster and more user-friendly. Nonetheless, the laser methodology gave promising results for the noncontact monitoring of immersed plates.

7.0 CONCLUSIONS AND RECOMMENDATIONS FOR FUTURE STUDIES

7.1 CONCLUSIONS

In the fundamental research we investigated the effect of some parameters on the laser-generated ultrasound applied to immersed plates. In particular, we investigated two separate wavelengths, namely the 1.064 μm and the 0.532 μm, in order to verify which one is more suitable for damage detection on immersed structures. Due to absorption of water, we concluded that the green light is the only one suitable for such applications. Then, we investigated the effect of the temperature and pressure on the amplitude of the ultrasonic signals. Both effects are present, but they do not play a significant role in our field of study. Therefore, even if variations of temperature or pressure are present within the range investigated, the quality and amplitude of the laser-generated ultrasonic waves do not change dramatically. The effect of laser energy was also investigated, in order to narrow a good range for NDE applications. We concluded that energies between 160 mJ and 190 mJ are the most suitable being a good balance between effectiveness, signal amplitude increase and material deterioration.

A hybrid system consisting in a laser beam operating in the ablative regime (actuator) and various arrays of conventional immersion transducers (receivers) were then developed and tested in a series of different experiments. This technique has never been used for the NDE/SHM of immersed structures and the results are promising. We built *in house* a B scan consisting of an

array of immersions transducers securely mounted to a bench plate together with the laser head. The motion of the whole system was achieved by a series of belts and pulleys and it was controlled by a user-friendly interface running under Labview. The same interface allowed the control of all the significant laser parameters as well as the storage of the acquired data. We performed two types of tests were the number of transducers was incremented from four to five, the spatial distribution was changed from cross to half-circle and we incremented the number of defects from four to five. Both tests consisted of a full-scan of the plate repeated five times to increase the statistical data population. The repeatability of both the laser generation and the implementation over successive scans was proved though two types of cross-correlation analysis. The nature of the defects was various since we wanted to investigate if the technique was in any manner sensitive to this damage variety. Damage detection was achieved by the implementation of outlier analysis. In particular, for the first test, we extracted three features from the time, frequency and time-frequency domain that were later fed into unsupervised learning algorithm based on outlier analysis. We tested the whole set of data considering the baseline taken from all the five scans. We adopted an optimization approach that lead to conclude that higher number of features leads higher sensitivity to defects. In particular, we successfully detected the cross-cut and the hole trough. In the second test, eight features were extracted (five additional ones with respect to the former test) and a similar outlier analysis with the baseline taken from all scans was performed with good results. In fact, we were capable of detecting the horizontal cut, the vertical cut and the corrosion. Then, we implemented a new multivariate algorithm where the baseline was taken from the first scan only. The aim was investigating the possibility that a training of the data can be achieved when considering a baseline that is not inclusive to all the data-set used for testing. In this case, the highest success rate approximated the 65% in the case

of single feature. The method was not very effective at discriminating the defects, as it categorized the greatest part of the data points as outliers.

The experimental investigations of the immersed plate pointed out a constant peak energy around 500 kHz for the S_0 mode. Tempting to address this phenomenon, we planned a new series of tests where six aluminum plates of varying thickness between 1.016 mm and 9.525 mm were tested by our hybrid laser-immersion transducer system. We experimentally proved that the peak of energy decreases with the increase of thickness. In all cases, we were capable of tracing the group velocity of the fundamental symmetric mode and we compared them with the theoretical curve calculated with the SAFE method, reaching a very good agreement. On this basis, we provide a list of ranges of peak energy according to plate thickness and fixed distance between the receivers and the actuator (in this case the laser beam).

The hazards associated with the laser use and the complexity of operating this system in unprotected environments suggested the implementation of a similar system where the laser generation was substituted by a focused transducer. The receivers were allocated in a half-circle position where the distance between the actuator and the receivers was wider compared to former tests in order to cover a larger area on the plate. We considered as defects all the points that were inside the area covered by the transducers during the scan. The B-scan on the plate was repeated five times to increase the statistical population data. We extracted seven features from the time, frequency and time-frequency domain that were later fed into an unsupervised algorithm based on outlier analysis. The baseline was chosen from defect-free location at data points sampled from all the five scans. The multivariate analysis was performed following an optimization approach for the features. The results in terms of success rate were the highest (95.79%) for the case of all the seven features, even though a similar rate was achieved already for some of the

combination considering six features. This suggests that higher number of features increases the sensitivity of the technique, but not necessarily the highest number combination produces the highest success rate, especially when some features are similar. However, only in the case of seven features all the outliers were properly classified and only 2 points were considered as false positive. The results suggest that the application with the focused transducer is very effective at detecting all the defects.

We concluded the analysis by comparing the hybrid laser-immersion transducer system with the focused transducer system. Both were promising at detecting defects in immersed plates. The latter could be considered faster, lighter and hazard-free compared to the laser technology. As such, its use could potentially find wider applications in the noncontact monitoring of immersed structures.

7.2 RECOMMENDATIONS FOR FUTURE STUDIES

The use of laser-generated ultrasound has been shown promising for the NDE of immersed plates. To the best of the author's knowledge, no research has been conducted prior to this dissertation for the damage detection of immersed plates using a hybrid laser-immersion transducer system. The applications of the proposed technology could span from the inspection of immersed structures to the inspection of pipelines from the inner diameter in order to avoid service interruption. However, in order to have this technology implemented in the field, research and development has to be conducted to waterproof the laser, to control the motion of the inspection system, to minimize the power requirement. The number and the arrangement of the receivers should also be investigated in order to find a good tradeoff between the widest area

to be probed with a single laser shot and the most acceptable signal-to-noise ratio. Future researches may also focus on other signal processing algorithm and pattern recognition techniques to maximize the sensitivity to the presence of damage and minimize the number of false positives and negatives.

The dependence between the thickness and the peak energy of the laser-generated waves could lead important results for experiment planning. The possible effect of the distance between the actuator and the receivers could also be investigated as a parameter for peak concentration.

The results achieved with the focused transducer were promising in terms of damage detection, since all the defects were detected. Furthermore, to cut the computational time, one approach consists of the reduction of the number of variables in the multivariate algorithm. This leads to the reduction of the dimensionality of the features. Rather than adopting methods such as principal component analysis, we think that, due to the nature of the problem, a better approach would be to look at the physics of the experiments. In fact, since we averaged 200 times signals that are highly repeatable and we computed the ratios among transducers that have close spatial path, it is reasonable to presume that some entries are very similar. Thus, it would be meaningful to adopt only the ratios that are, for instance, sensitive to the defects, neglecting all the others to try to reduce the dimensionality of the problem.

PUBLICATIONS STEMMED FROM THIS WORK

Peer-reviewed journal paper

Pistone, E., Li, K. and Rizzo, P. (2013, accepted – in press). "Noncontact Monitoring of Immersed Plates by means of Laser-induced Ultrasounds," *Structural Health Monitoring, an International Journal (Special Issue on Noncontact Measurement Technology for SHM).*

Bagheri, A., Pistone, E. and Rizzo, P. (2013, accepted – in press). "Guided Ultrasonic Wave Imaging for Immersed Plates Based on Wavelet Transform and Probabilistic Analysis," *Research in Nondestructive Evaluation*.

Pistone, E., Bagheri, A., Rizzo, P.. "Outlier Analysis and Artificial Neural Network Applied to the Noncontact Monitoring of Immersed Plates," *in preparation*.

Pistone, E., Rizzo, P.. "Comparison between Laser-generated Ultrasound and Focusing Technique for the Remote Monitoring of Immersed Plates," *in preparation*.

Conference Papers

Bagheri, A., Pistone, E. and Rizzo, P. (2013, submitted). "Assessment and Condition Evaluation of Immersed Plates," *International Conference on Infrastructure Management, Assessment and Rehabilitation Techniques*, Sharjah, UAE, March 4-6, 2014.

Pistone, E., Bagheri, A., Li, K. and Rizzo, P. (2013, accepted – in press). "Advancement on the Inspection of Immersed Plates by means of Guided Waves," *Proceedings of 9th International Workshop on Structural Health Monitoring*, Ed. F.K. Chang, Stanford, CA, USA, Sept. 10–12, 2013.

Pistone, E., Bagheri, A. and Rizzo, P. (2013, accepted – in press). "Signal Processing for the Smart Inspection of Immersed Plates," *Proceedings of the 6th ECCOMAS Conference on Smart Structures and Materials*, SMART2013, Torino, Italy, 24-26 June 2013.

Pistone, E., Li, K., Bagheri, A. and Rizzo, P. (2013, accepted - in press). "Signal Processing for the Inspection of Immersed Structures," *Proceedings of SPIE's 20th Annual International Symposium on Smart Structures and Materials*, Sensors and Smart Structures Technologies for Civil, Mechanical, and Aerospace Systems 2013, edited by N. Meyendorf, N. Wereley, V. Giurgiutiu, J. P. Lynch, Proc. of SPIE.

Rizzo, P., Pistone, E., Werntges, P., Han, J. and Ni, X. (2013). "Inspection of Underwater Metallic Plates by means of Laser Ultrasound", Intl. Symp. on Nondestructive Testing of Materials and Structures, NDTMS-2011, 15-18 May 2011, Istanbul, Turkey, O. Büyüköztürk et al. (eds.), Nondestructive Testing of Materials and Structures, *RILEM Bookseries 6*, pp. 675-680.

Rizzo, P., Pistone, E. (2011). "Effect of Water Temperature on the Laser-based Ultrasonic Testing of Immersed Structures", *Proceedings of the 8th International Workshop on Structural Health Monitoring*, Ed. F.K. Chang, Stanford, CA, USA, September 13–15, 2011, pp.1158-1164.

Pistone, E., Rizzo, P. and Werntges, P. (2011)."Bulk Waves for the Nondestructive Inspection of Immersed Structures," *Conference Proceedings of the Society for Experimental Mechanics Series, Experimental and Applied Mechanics*, Vol. 6, Mohegan Sun, Uncasville, CT, USA, June 13-16, 2011, pp. 643-649.

Pistone, E., Rizzo, P. and Werntges, P. (2011). "Hazard Mitigation of Water Mains by means of Immersed Active/Passive Inspection Systems," *Proceedings of 2011 NSF Engineering Research and Innovation Conference*, Atlanta, Georgia, USA, January 4 -7, 2011.

BIBLIOGRAPHY

[1] https://www.asnt.org/

[2] U.S. Environmental Protection Agency. Addressing the challenge through innovation, http://www.epa.gov/nrmrl/pubs/600f07015/600f07015.pdf (2010).

[3] http://www.post-gazette.com/pg/09351/1021687-100.stm (2013).

[4] Rizzo, P. NDE/SHM of Underwater Structures: A Review. *Advances in Science and Technology*, 83:208-216, 2013.

[5] Rizzo, P. "Structural Health Monitoring of Civil Structures: New Methodologies and Field Applications 2012", *Advances in Civil Engineering*, editorial, 2012.

[6] Goldberg, L. Diversity in underwater inspection. *Materials evaluation*, 54(3): 401-403, 1996.

[7] Mijarez-Castro, R. A remote and autonomous continuous monitoring ultrasonic system for flood detection in sub-sea members of offshore steel oilrigs, *Ph.D. Thesis*, University of Manchester, UK, 2006.

[8] Hayward, G., Pearson, J., & Stirling, G. An intelligent ultrasonic inspection system for flooded member detection in offshore structures. *Ultrasonics, Ferroelectrics and Frequency Control, IEEE Transactions on*, 40(5): 512-521, 1993.

[9] Rizzo, P. Water and Wastewater Pipe Health Monitoring: a Review. *Advances in Civil Engineering*, 83:208-216, 2010.

[10]Shull, P.J. Nondestructive Evaluation: theory, techniques, and applications, Marcel Dekker Ed., New York, 2002.

[11] http://www.sewer-rehabilitation.com/ (2013).

[12]Water Environment Research Foundation http://www.werf.org/AM/CustomSource/Downloads/uGetExecutiveSummary.cfm?FILE=ES-01-CTS-7.pdf&ContentFileID=1960, (2010).

[13]Teichgräber, B., Stemplewski, J., Althoff, H., and Elkmann, N. Remote controlled inspection device for large sewers. *Water Practice and Technology*, 1(4), doi: 10.2166/WPT.2006080, 2006.

[14]National Research Council, http://irc.nrc-cnrc.gc.ca/pubs/index_e.html (2010).

[15]Eiswirth, M., Heske, C., Burn, L.S., and DeSilva, D. New methods for water pipeline assessment. *IWA World Water Congress*, Berlin, Germany, 2001.

[16]Mergelas, B. and Henrich, G. "Leak locating method for precommissioned transmission pipelines: North American case studies," *Leakage 2005*, Halifax, Canada, 2005.

[17]McNulty, J.G. An acoustic based system for detecting, locating and sizing leaks in water pipelines. *4th International conference on water pipeline systems*, York, United Kingdom, 2001.

[18]Yang, J., Qingxin, Y., Guanghai, L., and Jingyan, Z. Acoustic emission source identification technique for buried gas pipeline leak. *Proceeding of the IEEE ICARCV 2006 Conference*:1-5, 2006.

[19]Kaewkongka, T. and Lim, J. Statistical estimated parameter for pipeline condition monitoring using acoustic emission. *Proceeding of the IEEE Instrument and Measurement Technology Conference*: 1-3, 2007.

[20]Sergiev, B. P. and Pachkov, A. V. Use of the acoustic-emission method for monitoring the condition of industrial pipelines. *Chemical and Petroleum Engineering*, 30(7-8):321-324, 1994.

[21]Shehadeh, A., Steel, J. A., and Reuben, R. L. Acoustic emission source location for steel pipe and pipeline applications: the role of arrival time estimation. *Journal of Process Mechanical Engineering*, 220(Part E):121-133, 2006.

[22]Travers, F. Acoustic monitoring of prestressed concrete pipe. *Construction and Building Materials*, 11(3): 175-187, 1997.

[23]Achenbach, J.D. *Wave propagation in elastic solids* (Vol. 16): North-Holland Amsterdam, 1973.

[24]Alleyne, DN, & Cawley, P. The excitation of Lamb waves in pipes using dry-coupled piezoelectric transducers. *Journal of Nondestructive Evaluation*, 15(1): 11-20, 1996.

[25]Rose, J.L. *Ultrasonic waves in solid media*: Cambridge university press, Cambridge, 2004.

[26]Kundu, T. *Ultrasonic nondestructive evaluation: engineering and biological material characterization*: CRC press, Boca Raton, FL, 2003.

[27]Rizzo, P. and Lanza di Scalea, F. Wavelet-based Unsupervised and Supervised Learning Algorithms for Ultrasonic Structural Monitoring of Waveguides. Chapter 8, *Progress in Smart Materials and Structures Research,* P. L. Reece, ed., Nova Editorial: 227-290, 2006.

[28]Bagheri, A., Pistone, E. and Rizzo, P. "Guided Ultrasonic Wave Imaging for Immersed Plates Based on Wavelet Transform and Probabilistic Analysis," *Research in Nondestructive Evaluation,* (2013, accepted – in press).

[29]Na, W. B., & Kundu, T. Underwater pipeline inspection using guided waves. *Journal of Pressure Vessel Technology-Transactions of the Asme,* 124(2):196-200. doi: Doi 10.1115/1.1466456, 2002.

[30]Mijarez. R., Gaydecki, P. and Burdekin, M. Flood member detection for real-time structural health monitoring of sub-sea structures of offshore steel oilrigs, *Smart Matl. Struct.*,16: 1857-1869, 2007.

[31]Bingham, J., Hinders, M., & Friedman, A. Lamb wave detection of limpet mines on ship hulls. *Ultrasonics*, 49(8):706-722, 2009.

[32]Monchalin, J.P. Optical detection of ultrasound. *IEEE Transactions on Ultrasonics Ferroelectrics and Frequency Control*, 33: 485-499, 1986.

[33]Scruby, CB, & Drain, LE. Laser Ultrasonics: Techniques and Applications. *Bristol: Adam Hilger*, New York, NY, 1990.

[34]Monchalin, J.P., Néron, C., Bussière, J.F., Bouchard, P., Padioleau, et al. Laser-ultrasonics: from the laboratory to the shop floor. *Advanced performance materials,* 5(1): 7-23, 1998.

[35]M. Lowe, "Matrix techniques for modelling ultrasonic waves in multilayered media," IEEE Trans. *Ultrason. Ferroelectr. Freq. Control*, 42: 25–542, 1995.

[36]J. C. P. McKeon and M. K. Hinders. Parallel projection and cross-hole lamb wave contact scanning tomography. *J. Acoust. Soc. Am,*. 106:2568– 2577, 1999.

[37]P. Fromme, P. D. Wilcox, M. J. S. Lowe, and P. Canvley. On the development and testing of a guided ultrasonic wave array for structural integrity monitoring. *IEEE Trans. Ultrason. Ferroelectr. Freq. Contro,l* 53:777–785, 2006.

[38]D. Alleyne and P. Cawley. The long range detection of corrosion in pipes using lamb waves. *Review of Progress in Quantitative NDE,* edited by D.O. Thompson and D. E. Chimenti Plenum, New York, Vol. 14, 1994.

[39]Rizzo, P. and Lanza di Scalea, F. Feature Extraction for Defect Detection in Strands by Guided Ultrasonic Waves," Journal of Structural Health Monitoring, 5(3): 297-308, 2006.

[40]B Pavlakovic, M Lowe, D Alleyne. Disperse: a general purpose program for creating dispersion curves, *Review of Progress in Quantitative Nondestructive Evaluation*, 16:185-192, 1996.

[41]Marzani, A., Viola, E., Bartoli, I., Lanza di Scalea, F., & Rizzo, P. A semi-analytical finite element formulation for modeling stress wave propagation in axisymmetric damped waveguides. *Journal of Sound and Vibration*, 318(3): 488-505, 2008.

[42]Aalami, B. Waves in prismatic guides of arbitrary cross section. *Journal of Applied Mechanics*, 40:1067-1072, 1973.

[43]Hayashi, T., Song, W.-J., and Rose, J. L. Guided wave dispersion curves for a bar with an arbitrary cross-section, a rod and rail example. *Ultrasonics*, 41:175-183, 2003.

[44]Gavrić, L. Computation of propagating waves in free rail using a finite element technique. *Journal of Sound Vibration*, 185:531-543, 1995.

[45]Rizzo, P., Bartoli, I., Marzani A., and Lanza di Scalea, F. Defect classification in pipes by neural networks using multiple guided ultrasonic wave features. *ASME Journal of Pressure Vessel Technology, Special Issue on the Nondestructive Evaluation of Pipeline and Vessel Structures*, 127(3):294-303, 2005.

[46]Hayashi, T., Kawashima, K., Sun, Z., and Rose, J. Guided wave focusing mechanics in pipe. *ASME Journal of Pressure Vessel Technology*,122:317-321, 2005.

[47]Rizzo, P., Bordoni, G., Marzani, A., and Vipperman, J. Localization of Sound Sources by Means of Unidirectional Microphones. Measurement Science and Technology, 20, 055202, 2009.

[48]Gazis, D. Three dimensional investigation of the propagation of waves in hollow circular cylinders. *Journal of Acoustical Society of America*, 31(5):568-578, 1959.

[49]Fitch,A. Observation of elastic-pulse propagation in axially symmetric and nonaxially symmetric longitudinal modes of hollow circular cylinders. *Journal of Acoustical Society of America*, 35(5):706-708, 1963.

[50]Safaai-Jazi, A., Jen, C.K. and Farnell, G. Cutoff conditions in an acoustic fiber with infinitely thick cladding. *IEEE Transaction in Ultrasonics and Ferroelectris Frequency Control*, 33(1): 69-73, 1986.

[51]Simmons, J., Drescher-Krasicka, H. and wadley, H. Leaky axysimmetric modes in infinite clad rods. *Journal of acoustical Society of America*, 92(2):1061-1090, 1992.

[52]Viens, M., Tshukahara, C. et al. Leaky torsional modes in in infinite clad rods. *Journal of acoustical Society of America*, 95(2):701-707, 1994.

[53]Rose, J.L., Jiao, D. and Spanner, J. Jr. Ultrasonic guided wave NDE for piping. *Materials and Evaluation*, 54:1310–1313, 1996.

[54]Rose, J., Cho, Y. and Ditri, J.J. Cylindrical guided wave leakage due to liquid loading in. D.O. Thomson, D.E. Chimenti (Eds), *Review of progress in quantitative NDE*, Vol. 13, plenum Press, New York: 259-266, 1994.

[55]Rose, J. A Baseline and Vision of Ultrasonic Guided Wave Inspection Potential. *Journal of Pressure Vessel Technology*, 124: 273-282, 2002.

[56]Rose, J.L., Mu, J. and Van Velsor, J. K. New Directions in Guided Wave Pipe Testing. *Materials Evaluation*: 375–378, 2007.

[57]Rose, J. Ultrasonic guided waves in structural health monitoring. *Key Engineering Materials*, 270-273(I):14-21, 2004.

[58] Liu, C., Harley, H. et al. Ultrasonic monitoring of a pipe under operating conditions,"*Proceedings of SPIE - The International Society for Optical Engineering*, Vol. 8345, *Sensors and Smart Structures Technologies for Civil, Mechanical, and Aerospace Systems 2012*, 2012.

[59]Alleyne, D., Lowe, M., Cawley, P. The reflection of guided waves from circumferential notches in pipes. *Journal of Applied Mechanics*, 65:635–641, 1998.

[60]Alleyne, D., Pavlakovic, B., Lowe, M., and Cawley, P. Rapid, long range inspection of chemical plant pipework using guided waves. *Insight*, 43:93–96, 2001.

[61]Carandente, R., Ma, J., Cawley, P. The scattering of the fundamental torsional mode from axi-symmetric defects with varying depth profile in pipes. *Journal of acoustical Society of America*, 127: 3440-3448, 2010.

[62]Demma, A., Cawley, P., Lowe, M., et al. The reflection of guided waves from notches in pipes: a guide for interpreting corrosion measurements. *NDT & E INTERNATIONAL*, 37:167-180, ISSN:0963-8695, 2004.

[63]Long, R., Lowe, M., Cawley P. Attenuation characteristics of the fundamental modes that propagate in buried iron water pipes. *Ultrasonics*, 41: 509-519, ISSN:0041-624X, 2003.

[64]Lowe, M., Alleyne, D., and Cawley, P. The mode conversion of a guided wave by a part-circumferential notch in a pipe. *Journal of Applied Mechanics*, 65:649–656, 1998.

[65]Lowe, M.J., Cawley, P., Galvagni, A. Monitoring of corrosion in pipelines using guided waves and permanently installed transducers. *Journal of acoustical Society of America*, 132, 1932-1938, 2012.

[66]Aristegui, C., Lowe, M.J.S., Cawley, P. Guided waves in fluid-filled pipes surrounded by different fluids. *Ultrasonics*, 39: 367-375, ISSN:0041-624X, 2001.

[67]Cawley P, Lowe MJS, Alleyne DN, et al. Practical long range guided wave testing: applications to pipes and rail. *Materials Evaluation*, 61:66-74, ISSN:0025-5327, 2003.

[68] http://www.guided-ultrasonics.com/ (2013).

[69]Zhu, W., and Rose, J. L. Lamb wave generation and reception with time-delay periodic linear arrays: A BEM simulation and experimental study. *IEEE Trans. Ultrasonics, Ferroelectrics and Freq. Ctl.*, 46(3): 654-664, 1999.

[70] Giurgiutiu, G. Lamb Wave Generation with Piezoelectric Wafer Active Sensors for Structural Health Monitoring. *Proc. SPIE- Smart Structures and Materials 2003: Smart Structures and Integrated Systems*, 5056:111-122, 2003.

[71]Greve, D.W. ,Neumann, J.J., Nieuwenhuis, J.H.; Oppenheim, I.J.; Tyson, N.L. Use of Lamb waves to monitor plates: experiments and simulations. *Proceedings of SPIE, Sensors and Smart Structures Technologies for Civil, Mechanical, and Aerospace Systems*, 5765, n PART 1:281-292, 2005.

[72]Lee, B.C., Staszewski, W.J. Modelling of Lamb waves for damage detection in metallic structures: Part I. Wave propagation. *Smart Materials and Structures*, 12(5):804-814, 2003.

[73]Lee, B.C., Staszewski, W.J. Modelling of Lamb waves for damage detection in metallic structures: Part II. Wave interactions with damage. *Smart Materials and Structures*, 12(5):815-824, 2003.

[74]Lee, B.C., Staszewski, W.J. Lamb wave propagation modelling for damage detection: I. Two-dimensional analysis. *Smart Materials and Structures*, 16(2):249-259, 2007.

[75]Lee, B.C., Staszewski, W.J. Lamb wave propagation modelling for damage detection: II. Damage monitoring strategy. *Smart Materials and Structures*, 16(2):260-274, 2007.

[76]Packo, P., Bielak, T.; Spencer, A.B.; Staszewski, W.J.; Uhl, T.; Worden, K. Lamb wave propagation modelling and simulation using parallel processing architecture and graphical cards. *Smart Materials and Structures*, 21(7):1-13, 2012.

[77]Ostachowicz, W., Krawczuk, M., Zak, A., Kudela, P. Wave propagation modelling for structural damage detection. *International Journal of COMADEM*, 13(1): 47-62, 2010.

[78]Han, S., Palazotto, A. N., Leakeas, C. L. Finite-element analysis of lamb wave propagation in a thin aluminum plate. *Journal of Aerospace Engineering*, 22(2):185-197, 2009.

[79]Pavlakovic, B. “Leaky guided ultrasonic waves in NDT”, Ph.D. Thesis, Mechanical Engineering Department, Imperial College London, 1998.

[80]Lowe, M.J.S., Cawley, P. and Pavlakovic, B.N. A General Purpose Computer Model for Calculating Elastic Waveguide Properties, with Application to Non-Destructive Testing. *Surface Waves in Anisotropic and Laminated Bodies and Defects Detection NATO Science Series II: Mathematics, Physics and Chemistry*, 163:241-256, 2005.

[81]Dao, C.M., Das, S., Banerjee, S., Kundu, T. Wave propagation in a fluid wedge over a solid half-space - Mesh-free analysis with experimental verification. *International Journal of Solids and Structures*, 46(11-12):2486-2492, 2009.

[82]Banerjee, S., Kundu, T. Ultrasonic field modeling in plates immersed in fluid. *International Journal of Solids and Structures*, 44(18-19):6013-6029, 2007.

[83]Banerjee, S., Kundu, T. Scattering of ultrasonic waves by internal anomalies in plates immersed in a fluid. *Proceedings of SPIE - The International Society for Optical Engineering, Health Monitoring and Smart Nondestructive Evaluation of Structural and Biological Systems V:* 6177, 2006.

[84]Ahmad, R., Kundu, T., Placko, D. Modeling of the ultrasonic field of two transducers immersed in a homogeneous fluid using distributed point source method. *I2M (Instrumentation, Measurement and Metrology) Journal*, 3:87–116, 2003.

[85]Kundu, T., Placko, D., Rahani, E.K., Yanagita, T., Dao, C.M. Ultrasonic field modeling: A comparison of analytical, semi-analytical, and numerical techniques. *IEEE Transactions on Ultrasonics, Ferroelectrics, and Frequency Control*, 57(12):2795-2807, 2010.

[86]Castaings, M. , Cawley, P. The generation, propagation and detection of Lamb waves in plates using air-coupled ultrasonic transducers. *Journal of the Acoustical Society of America*, 100:3070-3077, ISSN:0001-4966, 1996.

[87]Cawley,P., Alleyne,D.N. The use of Lamb waves for the long range inspection of large structures. *Ultrasonics*, 34:287-290, ISSN:0090-5607, 1996.

[88]Alleyne, C.P., Cawley, P. The Interaction of Lamb Waves with Defects. *IEEE Transactions on Ultrasonics Ferroelectris and Frequency Control*, 39:381-397, ISSN:0885-3010, 1992.

[89]Alleyne, C.P., Cawley, P. Optimization of Lamb Wave Inspection Techniques. *NDT & International*, 25:11-22, 0963-8695, 1992.

[90]Greve, David W. ,Oppenheim, Irving J.; Zheng, Peng. Lamb waves and nearly-longitudinal waves in thick plates. *Proceedings of SPIE, Sensors and Smart Structures Technologies for Civil, Mechanical, and Aerospace Systems*, 6932, DOI: 10.1117/12.775919, 2008.

[91]Greve, D.W., Oppenheim, I.J., Sohn, H., and Yue, C.P. "An inductively coupled (wireless) Lamb wave transducer," *Proc. Third International Workshop on Advanced Smart Materials and Smart Structures*: 27-33, (Techno-Press, Yuseong, Korea), 2007.

[92]Cegla, F.B. Energy concentration at the center of large aspect ratio rectangular waveguides at high frequencies. *Journal of the Acoustical Society of America*, 123(6): 4218-4226, 2008.

[93]Chen, J., Su, Z., Cheng, Li. Identification of corrosion damage in submerged structures using fundamental anti-symmetric Lamb waves. *Smart Materials and Structures*, 19(1):1-12, 2010.

[94]Cegla, FB, Cawley, P., & Lowe, MJS. Material property measurement using the quasi-Scholte mode—A waveguide sensor. *The Journal of the Acoustical Society of America*, 117: 1098-1107, 2005.

[95]Aussel, J.D., & Monchalin, J.P. Precision laser-ultrasonic velocity measurement and elastic constant determination. *Ultrasonics*, 27(3):165-177, 1989.

[96]Lanza di Scalea, F., Rizzo, P., & Marzani, A. Propagation of ultrasonic guided waves in lap-shear adhesive joints: Case of incident a Lamb wave. *The Journal of the Acoustical Society of America*, 115:146-156, 2004.

[97]Wooh, S.C., & Zhou, Q. Behavior of laser-induced ultrasonic waves radiated from a wet surface. Part I. Theory. *Journal of Applied Physics*, 89(6):3469-3477, 2001.

[98]Wooh, S.C., Zhou, Q. Behavior of laser-induced ultrasonic waves radiated from a wet surface. Part II. Experimental work," *J. Appl. Phys.*, 89:3478-3485, 2001.

[99]Achenbach, JD. Quantitative nondestructive evaluation. *International Journal of Solids and Structures*, 37(1):13-27, 2000.

[100]Davies, S.J., Edwards, S.J. et al. Laser-generated ultrasound: its properties, mechanisms and multifarious applications. *J. Appl. Phys.*, 26:329-348, 1993.

[101]Sohn, H. Laser based structural health monitoring for civil, mechanical, and aerospace systems. *Proc. of SPIE, Vol. 8345, Sensors and Smart Structures Technologies for Civil, Mechanical, and Aerospace Systems*, March 11-14, San Diego, California, 834502; doi:10.1117/12.921722, 2012.

[102]Burrows, S.E., Dutton, B., & Dixon, S. Laser generation of lamb waves for defect detection: Experimental methods and finite element modeling. *Ultrasonics, Ferroelectrics and Frequency Control, IEEE Transactions on*, 59(1): 82-89, 2012.

[103]Caron, J.N., DiComo, G.P., & Nikitin, S. Generation of ultrasound in materials using continuous-wave lasers. *Optics letters*, 37(5):830-832, 2012.

[104]Xu, B., Feng, J., Xu, G., Wang, J., Sun, H., & Cao, G. Laser-generated thermoelastic acoustic sources and Lamb waves in anisotropic plates. *Applied Physics A: Materials Science & Processing*, 91(1):173-179, 2008.

[105]Rizzo, P., & Lanza di Scalea, F. Wave propagation in multi-wire strands by wavelet-based laser ultrasound. *Experimental Mechanics*, 44(4): 407-415, 2004.

[106]Frenz, M., Paltauf, G., & Schmidt-Kloiber, H. Laser-generated cavitation in absorbing liquid induced by acoustic diffraction. *Physical review letters*, 76(19): 3546-3549, 1996.

[107]Sullivan, B., & Tam, AC. Profile of laser-produced acoustic pulse in a liquid. *The Journal of the Acoustical Society of America*, 75:437-441, 1984.

[108]Scruby, CB, Dewhurst, RJ, Hutchins, DA, & Palmer, SB. Quantitative studies of thermally generated elastic waves in laser-irradiated metals. *Journal of Applied Physics,* 51(12):6210-6216, 1980.

[109]Krehl, P. and Schwirzke, F. Correlation of stress-waves profiles and the dynamics of the plasma produced by laser irradiation of the plane solid targets, *J. Appl. Phys*. 46:462-468, 1965.

[110]Miller, J.C., & Haglund, R.F. *Laser ablation and desorption* (Vol. 30): Academic Press: San Diego, CA, 1998.

[111]Dewhurst, RJ, Hutchins, DA, Palmer, SB, & Scruby, CB. Quantitative measurements of laser-generated acoustic waveforms. *Journal of Applied Physics,* 53(6): 4064-4071, 1982.

[112]Ready, J.F. "Effects of High Power Laser Radiation," New York Academy, New York, 1971.

[113]Ready, J.F. Effects due to absorption of laser radiation. *J. Appl. Phys.*36: 4400-4406, 1975.

[114]Berthe, L., Fabbro, R., Peyre, P., Tollier, L., & Bartnicki, E. Shock waves from a water-confined laser-generated plasma. *Journal of Applied Physics*, 82(6):2826-2832, 1997.

[115]Bell, CE, & Landt, JA. Laser-induced high-pressure schock waves in water. *Applied Physics Letters*, 10(2):46-48, 1967.

[116]Berthe, L., Fabbro, R., Peyre, P., & Bartnicki, E. Wavelength dependent of laser shock-wave generation in the water-confinement regime. *Journal of applied physics*, *85*(11):7552-7555, 1999.

[117]Emmony, DC. Interaction of IR laser radiation with liquids. *Infrared Physics*, *25*(1):133-139, 1985.

[118]Kennedy, P.K., Hammer, D.X., & Rockwell, B.A. Laser-induced breakdown in aqueous media. *Progress in quantum electronics*, 21(3):155-248, 1997.

[119]Noack, J., & Vogel, A. Laser-induced plasma formation in water at nanosecond to femtosecond time scales: calculation of thresholds, absorption coefficients, and energy density. *Quantum Electronics, IEEE Journal of*, 35(8):1156-1167, 1999.

[120]Toker, G., Bulatov, V., Kovalchuk, T., & Schechter, I. Micro-dynamics of optical breakdown in water induced by nanosecond laser pulses of 1064nm wavelength. *Chemical Physics Letters*, 471(4):244-248, 2009.

[121]Toker, G., Bulatov, V., Kovalchuk, T., & Schechter, I. Underwater Interaction of 1064 nm Laser Radiation with Metal Target. *World Acad. Sci. Eng. Technol.*, 31:25-28, 2009.

[122]Vogel, A., Busch, S., & Parlitz, U. Shock wave emission and cavitation bubble generation by picosecond and nanosecond optical breakdown in water. *The Journal of the Acoustical Society of America*, 100:148-165, 1996.

[123]Hale, G., Querry, M. Optical constants of water in the 200-nm to 200-μm wavelength region. *Appl. Opt.*:12:555-563, 1973.

[124] Rusk, A., Williams, D., Querry, M. Optical constants of water in the infrared. *J. Opt. Soc. Am.*, 61:895-903, 1971.

[125]Smith, R., Baker, K. Optical properties of the clearest water (200-800 nm). *Appl. Opt.*, 20:177-184, 1981.

[126]Sogandares, M., Fry, E. Absorption spectrum (340-640 nm) of pure water. I. Photothermal measurements. *Appl. Opt.*, 36:8699-8709, 1997.

[127]Sullivan, S. Experimental study of the absorption in distilled water, artificial sea water, and heavy water in the visible region of the spectrum. *J. Opt. Soc. Am.*, 53: 962-967, 1963.

[128]Tam, A.C., Patel, C. K. N. Optical absorptions of light and heavy water by laser optoacoustic spectroscopy. *Appl. Opt.*, 18:3348-3358, 1979.

[129]Busse, G. Optoacoustic and photothermal material inspection techniques. *Appl. Opt.*, 21:107-110, 1982.

[130]Kuo, C.Y., Patel, C. K. N. Direct measurements of optoacoustic induced ultrasonic waves. *Appl. Phys. Lett.*, 44:752-754, 1984.

[131]Kuo, C.Y., Vieira, M.F. et al. Transient optoacoustic pulse generation and detection. *J. Appl. Phys.*, 55:3333-3336, 1984.

[132]McDonald, F.A., Wetsel, G.C. Generalized theory of the photoacosutic effect. *J. Appl. Phys.*, 49: 2313-2332, 1978.

[133]Patel, C. K. N., Kerl, R.J. A new optoacoustic cell with improved performance. *Appl. Phys. Lett.*, 30:578-579, 1977.

[134]Patel, C. K. N., Tam, A.C. Optoacoustic spectroscopy of liquids. *Appl. Phys. Lett.*, 34:467-470, 1979.

[135]Patel, C. K. N., Tam, A.C. Pulsed optoacoustic spectroscopy of condensed matter. *Rev Mod Phys*, 53:517-550, 1981.

[136]Sigrist, M., Kneubuhl, F. Laser-generated stress waves in liquids. *J. Acoust. Soc. Am.*, 55:3333-3336, 1984.

[137]Sigrist, M. Laser generation of acoustic waves in liquid and gases. *J. Appl. Phys*., 60:83-121, 1986.

[138]A. Morel. Optical properties of pure water and pure sea water. *Optical Aspects of Oceanography*, N. G. Jerlov and E. S. Nielson, eds. (Academic, New York, 1974):1-24, 1974.

[139]S. A. Sullivan. Experimental study of the absorption in distilled water, artificial sea water, and heavy water in the visible region of the spectrum. *Journal of the Optical Society of America*, 53(8): 962, 1963.

[140]K. F. Palmer and D. Williams. Optical properties of water in the near infrared. *Journal of the Optical Society of America*, 64(8):1107, 1974.

[141]M. R. Querry, P. G. Cary, and R. C. Waring. Split-pulse laser method for measuring attenuation coefficients of transparent liquids: Application to deionized filtered water in the visible region. *Applied Optics,* 17(22): 3587-3592, 1978.

[142]T. I. Quickenden and J. A. Irvin. The ultraviolet absorption spectrum of liquid water. J. *Chem. Phys*, 72(8): 4416, 1980.

[143]L. P. Boivin, W. F. Davidson, R. S. Storey, D. Sinclair, and E. D. Earle. Determination of the attenuation coefficients of visible and ultraviolet radiation in heavy water. *Applied Optics* ,25(6):877, 1986.

[144]R. A. J. Litjens, T. I. Quickenden, and C. G. Freeman. Visible and nearultraviolet absorption spectrum of liquid water. *Applied Optics*, 38(7): 1216, 1999.

[145]E. O. Hulburt. Optics of distilled and natural water. *Journal of the Optical Society of America*, 35(11): 698, 1945.

[146]http://en.wikipedia.org/wiki/Electromagnetic_absorption_by_water (2013).

[147]Wang, L. Measuring optical absorption coefficient of pure water in UV using the integrating cavity absorption meter. (*Doctoral dissertation*). Texas A&M University, 2008.

[148]M. Hass, J. W. Davisson, H. B. Rosenstock, and J. Babiskin. Measurement of very low absorption coefficients by laser calorimetry. *Applied Optics*, 14(5):1128, 1975.

[149]M. Hass and J. W. Davisson. Absorption coefficient of pure water at 488 and 541.5 nm by adiabatic laser calorimetry. *Journal of the Optical Society of America*, 67(5):622, 1977.

[150]J. Stone.Thermooptical technique for the measurement of absorption loss spectrum in liquids," *Applied Optics,12:*1828, 1973.

[151]Fairand, B.P.; Clauer, A.H. Laser generation of high amplitude stress waves. *Journal of Applied Physics,* 50(3):1497-1502, 1979.

[152]Stafe, M., Negutu, C. et al. Pulsed laser ablation of solids. *Rom. Rep. Phys.,* V 62:758-770, 2010.

[153]Alleyne, D., & Cawley, P. A two-dimensional Fourier transform method for the measurement of propagating multimode signals. *The Journal of the Acoustical Society of America,* 89: 1159-1168, 1991.

[154]Moser, F., Jacobs, L.J., & Qu, J. Modeling elastic wave propagation in waveguides with the finite element method. *Ndt & E International,* 32(4): 225-234, 1999.

[155]Valle, C., Niethammer, M., Qu, J., & Jacobs, L.J. (2001). Crack characterization using guided circumferential waves. *The Journal of the Acoustical Society of America,* 110: 1282-1290.

[156]Bartoli, I., Lanza di Scalea, F., Fateh, M., & Viola, E. Modeling guided wave propagation with application to the long-range defect detection in railroad tracks. *NDT & E International,* 38(5):325-334, 2005.

[157]Sale, M., Rizzo, P., & Marzani, A. Semi-analytical formulation for the guided waves-based reconstruction of elastic moduli. *Mechanical Systems and Signal Processing,* 25(6):2241-2256, 2011.

[158]Yaralioglu, G.G., Ergun, SA, & Khuri-Yakub, B.T. Finite-element analysis of capacitive micromachined ultrasonic transducers. *Ultrasonics, Ferroelectrics and Frequency Control, IEEE Transactions on,* 52(12):2185-2198, 2005.

[159]Newmark, N.M. A method of computation for structural dynamics. *Proc. Am.* Soc.*Civ. Engs,* 85(EM3):67-94, 1959.

[160]Mallat, S. *A wavelet tour of signal processing*: Academic press: San Diego, CA, 1999.

[161]Pistone, E., Li, K. and Rizzo, P. Noncontact monitoring of immersed plates by means of laser-induced ultrasouns. *Structural Health Monitoring, an International Journal (Special Issue on Noncontact Measurements technology for SHM),* in press, 2013.

[162]Rizzo, P., Cammarata, M., Dutta, D., Sohn, H., & Harries, K. An unsupervised learning algorithm for fatigue crack detection in waveguides. *Smart Materials and Structures,* 18(2): 1-11, 2009.

[163]Marzani, A., Viola, E., Bartoli, I., Lanza di Scalea, F., & Rizzo, P. A semi-analytical finite element formulation for modeling stress wave propagation in axisymmetric damped waveguides. *Journal of Sound and Vibration,* 318(3): 488-505, 2008.

[164]K. Worden. Structural fault detection using a novelty measure. *Journal of Sound and Vibration,* 201:85–101, 1997.

[165]Chetwynd, D., Rongong, J. A., Pierce, S. G., and Worden, K. Damage detection in an aluminium plate using outlier analysis, *Fatigue and Fracture of Engineering Materials and Structures*, 31(8): 629-643, 2008.

[166]K. Worden, S.G. Pierce, G. Manson, W.R. Philp, W. Staszewski, B. Culshaw. Detection of defects in composite plates using Lamb waves and novelty detection, *International Journal of System Science*,31:1397–1409, 2000.

[167]Worden, K., Manson, G., & Fieller, NRJ. Damage detection using outlier analysis. *Journal of Sound and Vibration,* 229(3):647-667, 2000.

[168]W. Staszewski, G. Pierce, K. Worden, W. Philp, G. Tomlinson, B. Culshaw. Wavelet signal processing for enhanced Lamb-wave defect detection in composite plates using optical fiber detection, *Optical Engineering*, 36:1877–1888, 1997.

[169]Rizzo, P., Sorrivi, E., Lanza di Scalea, F., Viola, E. Wavelet-based outlier analysis for guided wave structural monitoring: Application to multi-wire strands. *Journal of Sound and Vibration*, 307(1-2):52-68, 2007.

[170]Ying, Y., Harley, H. et al. "Applications of machine learning in pipeline monitoring," Proceedings of the *Congress on Computing in Civil Engineering, Proceedings, Computing in Civil Engineering - Proceedings of the 2011 ASCE International Workshop on Computing in Civil Engineering*:242-249, 2011.

[171]Worden, K., Sohn, H., & Farrar, CR. Novelty detection in a changing environment: regression and interpolation approaches. *Journal of sound and vibration*, 258(4):741-761, 2002.

[172]Sohn, H., Worden, K., & Farrar, C.R. Statistical damage classification under changing environmental and operational conditions. *Journal of Intelligent Material Systems and Structures*, 13(9):561-574, 2002.

[173]Guttormsson, S.E., Marks, RJ, El-Sharkawi, MA, & Kerszenbaum, I. Elliptical novelty grouping for on-line short-turn detection of excited running rotors. *Energy Conversion, IEEE Transactions on*, 14(1):16-22, 1999.

[174]Nair, K.K., Kiremidjian, A.S., & Law, K.H. Time series-based damage detection and localization algorithm with application to the ASCE benchmark structure. *Journal of Sound and Vibration*, 291(1):349-368, 2006.

[175]Sohn, H., Allen, D.W., Worden, K., & Farrar, C.R. Structural damage classification using extreme value statistics. *Journal of dynamic systems, measurement, and control*, 127(1):125-132, 2005.

[176]Park, H.W., & Sohn, H. Parameter estimation of the generalized extreme value distribution for structural health monitoring. *Probabilistic engineering mechanics*, 21(4):366-376, 2006.

[177]Nair, KK, Kiremidjian, AS, Lei, Y., Lynch, JP, & Law, KH. *Application of time series analysis in structural damage evaluation.* Proceedings of the International Conference on Structural Health Monitoring, Tokyo, Japan, November 14-16, 2003.

[178]Bushell, A.C., Edwards, C.; Palmer, S.B. Laser-generated surface waves on plates of varying thickness. *British Journal of Non-Destructive Testing*, 33(4): 177-182, 1991.

[179]Hutchins, D.A., Lundgren, K., and Palmer, S.B. A laser study of transient Lamb waves in thin material. *J. Acoust. Soc. Am*., 85(4): 1441-1448, 1989.

[180]Dewhurst, R.J., Edwards, C., McKie, A.D.W. and Palmer, S.B. Estimation of the thickness of thin metal sheet using laser generated ultrasound. *Applied Physic Letter*, 51(14): 1066-1068, 1987.

[181]Hayashi, Y., Ogawa, Sh.; Cho, H.; Takemoto, M. Non-contact estimation of thickness and elastic properties of metallic foils by the wavelet transform of laser-generated Lamb waves. *NDT and E International*, 32(1): 21-27, 1999.

[182]Billy, M., Adler, L. and Quentin, G. Measurement of backscattered leaky Lamb waves in plates. *Journal of Acoustical Society of America*, 75(4): 998-1001, 1984.

[183]Adler,L. Billy, M. and G . Quentin. Excitation of ultrasonic Rayleigh leaky waves at liquid-solid interface for general angle of incidence, *J. Appl. Phys*., 53: 8756-8758, 1984.

[184]H. L. Bertoni and T. Tamir. Unified theory of Rayleigh angle phenomena for acoustic beams at liquid-solid interfaces. *A ppl. Phys*., 2:157-172, 1973.

[185]W. G. Neubauer. Ultrasonic reflection of a bounded beam at Rayleigh and critical angles for a plane liquid-solid interface. *J. Appl. Phys*., 4(4):48-55, 1973.

[186]Bar-Cohen Y., A. K. Mal and C. -C. Yin. Ultrasonic Evaluation of Adhesive Bonding. *Journal of Adhesion*, 29(1-4):257-274, 1989.

[187]Dayal, V., and V.K. Kinra. Leaky Lamb waves in an anisotropic plate. I: An exact solution and experiments. *J. Acoustic Soc. of Amer*., 85(6):2268 – 2276, 1989.

[188]http://www.ndt.net/article/v05n06/barcohen/barcohen.htm.

[189]Bar-Cohen Y., and D. E. Chimenti. Leaky Lamb Waves in Fiber-Reinforced Composite Plates. *Review of Progress in Quantitative NDE*, Vol. 3B, D. O. Thompson and D. E. Chimenti (Eds.), Plenum Press, New York and London:pp. 1043-1049, 1984.

[190]Jansen D. P., and D. A. Hutchins. Lamb wave immersion Topography. *Ultrasonics*, 30: 245-254, 1992.

[191]Mal, A. K., and Y. Bar-Cohen. Ultrasonic Characterization of Composite Laminates. *Proceedings of the Joint ASME and SE meeting*, AMD-Vol. 90, A. K. Mal and T.C.T. Ting (Eds.), ASME, NY:1-16, 1998.

[192]Mal, A.K., Bar-Cohen, Y. and Lih, S.-S. Wave Attenuation in Fiber-Reinforced Composites. *Proceedings of M ^{3} D*, Kinra, V.K. (editor), ASTM STP, 1169:245-261, 1992.

[193]Nagy P. B., W. R. Rose and L. Adler. A Single Transducer Broadband Technique for Leaky Lamb Wave Detection. *Review of Progress in QNDE,* 6A: 483-490, 1987.

[194]Nayfeh, A. H., and D. E. Chimenti. Propagation of Guided-Waves in Fluid-Coupled Plates of Fiber-Reinforced Composit. *Journal of the Acoustical Society of America*, 83(5):1736-1747, 1998.

[195]Chimenti, D.E., Martin, R.W. Nondestructive evaluation of composite laminates by leaky Lamb waves. *Ultrasonic,* 29: 13-21, 1991.

[196]Y. Bar-Cohen, and S.-S. Lih. Experimental Enhancement of Leaky Lamb Wave Dispersion Data Acquisition and Implementation Challenges to NDE of Composites. *Materials Evaluation*, 58(6):801-806, 2000.

[197]Y. Bar-Cohen, A. K. Mal and Z. Chang. Defects Detection and Characterization Using Leaky Lamb Wave (LLW) Dispersion Data," ASNT '98 Spring Conference, Joint with 9th Asia-Pacific Conference on NDT, and 7th Annual Research Symposium, Anaheim, CA:195-197,1998.